Master's thesis

NTNU
Norwegian University of Science and Technology
Faculty of Social and Educational Sciences
Department of Geography

Oskar E. Lilienthal

The onset of relative sea-level rise in the late 19th century at Tranevåg salt marsh, southern Norway.

Master's thesis in Geography
Supervisor: Nixon, F. C.
August 2019

NTNU
Norwegian University of
Science and Technology

Oskar E. Lilienthal

The onset of relative sea-level rise in the late 19th century at Tranevåg salt marsh, southern Norway.

Master's thesis in Geography
Supervisor: Nixon, F. C.
August 2019

Norwegian University of Science and Technology
Faculty of Social and Educational Sciences
Department of Geography

NTNU
Norwegian University of
Science and Technology

Abstract

By the end of the 21st century, the highest projected rates of RSL rise following RCP 8.5, might approach or exceed ~10mm/yr for most of the Norwegian coast (Simpson et al., 2015). Records from the Norwegian tide gauge network show that relative sea level (RSL) is already rising in several locations, and this rise is expected to accelerate in the future (Richter et al., 2012; Simpson et al., 2015). This thesis aims to expand the observational data to help bridge the gap between geological and instrumental records of RSL change which will improve future GIA models that, in turn, will help develop more accurate estimates of present-day vertical land motion in Norway and improve century-scale RSL projections for Norway (Simpson et al., 2015).

This thesis reports new Holocene RSL observations for the past ~1500 years from the upper meter of the sedimentary record of a salt marsh in Tranevåg, southernmost Norway, based on X-ray fluorescence (XRF) measurements of Ti and U, calculated accretion rates, vegetation zone data and analysis of foraminiferal assemblages. Our results characterize RSL trends, focusing on the temporal gap between the youngest established geological evidence of RSL fall (1530 – 1370 cal. a. BP; Romundset et al., 2015), and the instrumental record of measured RSL rise from the tide gauge in Tregde which was installed in 1927 AD. The foraminiferal data presented in this thesis demonstrates that RSL continued falling until 519±22 cal. a. BP, followed by continued fall indicated by vegetation zone data. Rapidly increasing accretion rates, a common response of salt marshes to rising RSL (Müller-Navarra et al., 2019), correlates with increasing minerogenic influx to the salt marsh reflected by rapidly increasing Ti- and decreasing U elemental abundances. Our results show that RSL transitioned from falling/standstill to rising approximately 135 years ago in 1885 BP.

Sammendrag på Norsk

Mot slutten av det 21. århundre kan raten av relativ havnivåstigning nå eller overgå ~10 mm/år for store deler av den Norske kystlinjen om vi følger FNs klimapanel utviklingsbane 8.5 (Simpson et al., 2015). Målinger fra norske tidevannsmålere viser at relativt havnivå allerede øker flere steder, og denne økningen er forventet å akselerere fremover (Richter et al., 2012; Simpson et al., 2015). Denne avhandlingen forsøker å redusere den temporale avstanden mellom geologiske observasjoner og instrumentelle målinger av havnivå. Dette vil kunne forbedre fremtidig modellering av glasialisostatiske bevegelser, som vil være til nytte for utviklingen av mere nøyaktige estimater av vertikal landhevning og senkning i Norge, og dermed forbedre havnivåprojeksjoner for Norge (Simpson et al., 2015)

Denne avhandlingen rapporterer nye observasjoner av havnivå for de siste ~1500 årene, fra den øverste meteren av sediment fra en tidevannsmyr i Tranevåg, helt sør i Farsund kommune, basert på Røntgenfluorescensmålinger av Ti og U, sedimentasjonsrater, vegetasjonssoneringsdata og sammensetningen av foraminiferer i sedimentene. Våre resultater karakteriserer havnivåendringer med fokus på det temporale mellomrommet fra det yngste etablerte geologiske beviset på relativt havnivåfall (1530 – 1370 cal. a. BP; Romundset et al., 2015), og de instrumentelle målingene fra tidevannsmåleren i Tregde som viser en relativ havnivåøkning siden den ble montert i 1927 evt. Foraminiferdatane presentert i denne avhandlingen demonstrerer at relativt havnivåfall fortsatte frem til 519±22 cal. a. BP, etterfulgt av fortsatt fall frem mot moderne tid indikert av vegetasjonssoneringsdata. Raskt økende sedimentasjonsrater, noe som er vanlig for tidevannsmyrer når relativt havnivå øker (Müller-Navarra et al., 2019), korrelerer med en økt mineralsk tilstrømming til tidevannsmyren er indikert av raskt økende Ti- og synkende U konsentrasjoner i sedimentene. Våre resultater viser at relativt havnivå gikk fra en synkende/stillestående trend til en økende trend for omlag 135 år siden i 1885 evt.

Acknowledgements

First of all, I would like to thank my thesis supervisor professor Chantel Nixon of the Department of Geography at the Norwegian University of Science and Technology. Your door was always open, and I cannot overstate my gratitude for your continual guidance throughout the past three years. Thank you for introducing me to this project, which allowed me the contribute meaningfully to the body of science.

I would also like to thank the scientists Thomas lakeman, Anders Romundset and Lina Gislefoss, that invited me to join their fieldwork and helped with the lab work at NGU. Without your help, this thesis would not have been possible. And, Chris in Nova-Scotia, I never learned your last name, but your offer to do XRF-measurements on my cores, has been incredibly helpful for the analysis.

Contents

List of Figures

List of Tables

Chapter 1 Introduction

The majority of Norway's coastline will experience relative sea level (RSL) rise in the next 100 years, however, this will likely be less than the anticipated mean global rise (Church, 2013a; Simpson et al., 2015). Relative sea-level rise projections commissioned by Klimadirektoratet in 2015 give projected ensemble means for the 21st century in Norway of 10 to 30 cm (under the IPCC 2013 Representative Concentration Pathway 2.6 scenario; RCP henceforth), 0 to 35 cm (RCP 4.5), and 15 to 55 cm (RCP 8.5), depending on location. These projections are based on the Fifth Assessment Report of the Intergovernmental Panel for Climate Change (IPCC, Church 2013b), and the Coupled Model Intercomparison Project phase 5 output (Simpson et al., 2015). Records from the Norwegian tide gauge network show that RSL is already rising in several locations, and this rise is expected to accelerate in the future (Richter et al., 2012; Simpson et al., 2015).

For the Norwegian coast, long-term trends in RSL are mainly a function of glacial isostatic adjustment (GIA) and global mean sea level rise (GMSL). The coastal municipalities in Norway experience present day rates of vertical uplift (rebound) of 1 to 6 mm/yr due to the unloading of the Fennoscandian ice sheet. This vertical land motion counteracts the rise in GMSL caused by the addition of meltwater to and thermal expansion of the ocean, resulting in locally reduced rates of RSL rise. The rates of GIA along the Norwegian coast have slowed down significantly since the retreat of Younger Dryas glaciers about 11000 years BP (Sørensen, 1987). As rates of vertical crustal uplift continue to slow or cease, and as GMSL accelerates, local rates of RSL rise will increasingly reflect GMSL. For the majority of the Norwegian coast, this will mean accelerating rates of RSL rise for the rest of the century, and likely well into the next due to the long response time of the oceans and ice sheets to global warming. By the end of the 21st century, the highest projected rates following RCP 8.5, might approach or exceed ~10mm/yr for most of the Norwegian coast (Simpson et al., 2015).

Some of the anticipated coastal impacts from rising sea levels include flooded and damaged infrastructure (e.g. roads, submarine cables, fishing and port facilities, etc.), farmland, heritage buildings, and archaeological sites, submergence or inland migration (if possible) of coastal habitats and sediments, and increased shoreline erosion (Forbes et al., 2011; Church et al., 2013a). The occurrence and extent of these impacts will not be the same everywhere due to the wide variety of natural and anthropogenic factors that vary depending on location. Detailed knowledge of future sea-level rise in Norway, including how it will vary and change across space and time, and how it will manifest itself at the coast, is crucial for land-use planning, coastal management, and informing the general public (Simpson et al., 2015).

Several sea-level curves for various locations in Norway have been reconstructed from geological records (mainly based on sediment cores taken from isolation basins; outlined in Svendsen & Mangerud, 1987). The temporal resolution of these curves is low, especially for the past few millennia (Simpson et al., 2015). Currently, RSL histories for Norway for this time period include those reconstructed from geological data (e.g. Svendsen & Mangerud, 1987; Vorren et al., 1988; Romundset et al., 2015), and tide gauge data going back ca. 50-100 years (Richter et al., 2012; Wahl et al., 2013; Simpson et al., 2015). The uncertainty in RSL trends vary greatly in accordance with the length and quality of observational data.

The Agder region in southern Norway is among the regions expected to be most adversely affected by future RSL rise due to low rates of vertical uplift (Overpeck et al., 2006; Fjeldskaar et al., 2000). The geological Holocene RSL reconstructions from the area show a long period of RSL fall since the Tapes transgression peaked, approximately 7000 years ago, until present, however, measurements from the tide gauge at Tregde show that RSL has been rising, and is accelerating, since the beginning of measurements in AD 1927 (Romundset et al., 2015). The discrepancy between the geological record and tide gauge measurements is due to a temporal gap of ~1400 years between the youngest established geological evidence of RSL fall, the isolation of a basin from the sea dated to 1530-1370 cal. a BP, and the beginning of measurements at the tide gauge in Tregde in AD 1927.

1.1 Thesis Aim, Focus and Research Question

This thesis aims to contribute to Holocene sea level research by providing new insight into the nature of recent RSL change in southern Norway, and extend the observational data to help bridge the gap between geological and instrumental records which will improve future GIA models that, in turn, will help develop more accurate estimates of present-day vertical land motion in Norway and improve century-scale RSL projections for Norway (Simpson et al., 2015).

The main focus of this thesis is to address the uncertainty in the current RSL curve published by Romundset et al (2015) as to when the transition from RSL fall or standstill to RSL rise began. As such, the past ~1500 years defines the primary temporal scope of this thesis.

The primary research question that this thesis seeks to address is, thus: At what point in time did the transition from RSL fall or standstill to RSL rise in southern Norway occur?

To address the research question, a salt marsh in the Agder region was cored (figure 1.1). Two cores were subjected to magnetic susceptibility measurements, x-ray and high-resolution Red, Green, Blue (RGB) scanning, geochemical analysis (X-ray fluorescence), and palaeoecological analysis using foraminifera (where foraminifera are single-celled, cosmopolitan, marine and brackish organisms) and vegetation. To establish the timeframe for RSL change, organic matter was sampled from the cores for radiocarbon dating, and supplemented by interpretations of Pb concentrations in relation to the global atmospheric pollution history of Pb. An additional core was subjected to magnetic susceptibility measurements, x-ray and high resolution RGB scanning, as well as sampling for foraminifera.

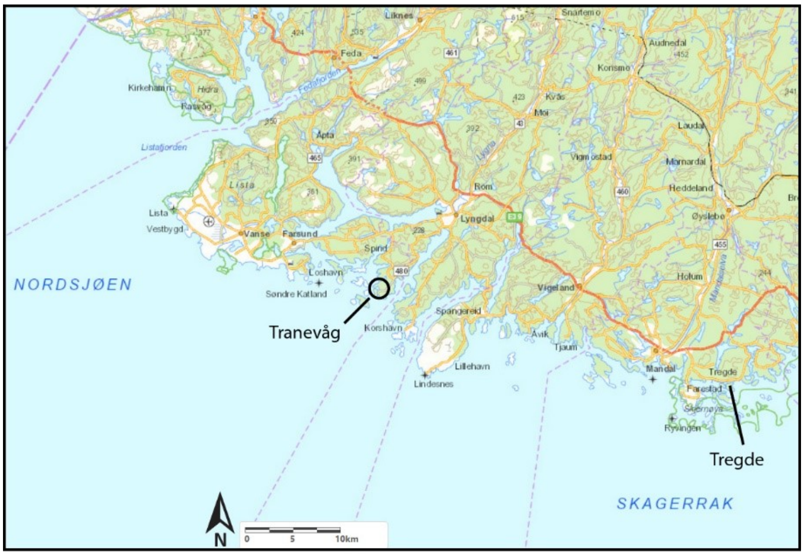

Figure 1.1 The location of the study area above a small bay near Tranevåg in the municipality of Farsund (coordinates: 58,060606 °N 6,9462 °E) and the nearest tide gauge in Tregde. Map from Kartverket (2019d)

Species identification of foraminifera and their abundance at specific levels in the subsurface (core) sediments were originally intended to be the basis for this thesis, however, due to problems with equipment, time constraints, and poor preservation of the foram tests (shells; discussed in chapter 3), a complete dataset was not acquired. Additionally, subsampling for cryptotephra layers was intended to be a part of this thesis, but was not carried out due to time constraints. However, if future studies allow, sampling for cryptotephra may be guided by the cryptotephra pre-screening (identifications of depths most likely to contain cryptotephra layers) presented in chapter 5.

As such, this thesis has two secondary foci: an assessment of the feasibility of using a foraminifera-based approach in southern Norway for sea level research and, an assessment of the use of cryptotephra layers for establishing core chronology (age model) is possible in the sedimentary records from southern Norway. The relevant literature, analytical concepts, methods, results and conclusions relating to these foci are therefore also included in this thesis.

1.2 Thesis Structure

This chapter (chapter 1) outlines the scientific background related to the research question this thesis seeks to address. Chapter 2 discusses the relevant literature relating to sea level, salt marshes and analytical concepts used in this thesis, as well as a detailed description of the study area. Chapter 3 describes how the field and lab-work were conducted.In chapter 4, the relevant data for this thesis is presented. The complete XRF-datasets and scans of additional sediment cores sections that are not relevant for the thesis aim are included in appendix 2 and 3, respectively. Chapter 5 includes an analysis and discussion of the results, followed by the resulting conclusions and recommendations in chapter 6.

Chapter 2 Theory and Background

2.1 Sea Level

Mean sea level (MSL) is an average of sea level measurements for a specific location, region, or ocean over a time period. Global mean sea level (GMSL) is MSL averaged over all of the Earth's oceans. Global mean sea level does not represent the sea surface height at any specific location, but changes in this measurement is an important measure of climate change due to its close correlation with ice sheet melting (Simpson et al., 2015; Benn & Evans., 2010; Overpeck et al., 2006).

The two main drivers of GMSL change on centennial to millennial timescales (of most relevance to this thesis) are ocean mass and density. Changes in ocean mass are controlled through the relationships between the oceans and any part of the hydrologic cycle where water mass is stored on land. Within the hydraulic cycle, glacio-eustacy, variations in the amount of water stored as land-based ice, is the dominant factor (Benn & Evans, 2010). This is well established in the geological record, which clearly shows that the growth and decay of glaciers and ice sheets have had a profound effect on GMSL (e.g. Overpeck et al., 2006). Thermosteric processes, controlled by thermal expansion/contraction, and haline contraction, also play a major role in GMSL change. Of these, temperature is considered the most dominant globally, however in the colder regions (e.g. Arctic ocean), salinity can also have a significant role. On geological timescales, tectonic activity modifies the shape and size of ocean basins, affecting local and global MSL (Benn & Evans, 2010).

Gravity plays an important role in determining how the sea water mass distributes itself globally, and thus also in local sea levels. Areas that have a stronger gravity field pull on the ocean mass causing a regional rise in the elevation of the sea surface, while lowering occurs in areas of weaker gravity fields. Any redistribution of mass on the Earth's surface, for example, during glacial-interglacial cycles between the ocean and ice sheets, will affect the gravity field, and subsequently readjust regional MSL. Likewise, winds in particular, but also ocean currents, redistribute water masses which, in addition to directly affecting water levels, changes the gravity field (Simpson et al., 2015; Benn & Evans, 2010). Glacioisostatic adjustments (GIA), which are defined as vertical movements in Earth’s crust due to loading and unloading of ice (Benn & Evans, 2010; discussed in section 2.1.2), of both seafloor and land, also contribute to changes in the gravity field (Simpson et al., 2015) and to local relative sea level (see next section).

Over very short timescales (days to weeks), atmospheric pressure plays an important part in water distribution and sea level heights. High pressure systems, which have more weight (air mass), exert a greater downward force on the ocean surface than low pressure systems, causing a depression of the water surface in high pressure areas and an upward bulge in low pressure areas. As such, low pressure systems generally cause higher water levels locally (Simpson et al., 2015).

2.1.1 Relative Sea Level

The relationship between land and sea surface heights is an aspect of great concern for coastal societies facing future sea level rise (Overpeck et al., 2006). At any coastal location, sea level can change due to elevational changes of both the ocean and land surfaces (Benn & Evans, 2010). In this thesis, Relative sea level (RSL) is defined as the difference between the sea surface and the solid surface of the Earth at a geographic location (Shennan, 2015).

Over centuries to millennia, which are the timescales of most relevance to this thesis, the main factors affecting RSL are changes in GMSL (i.e. ocean mass and density), gravitational effects due to the timing and magnitude of melting of different ice masses, and vertical land motion due to GIA (Benn & Evans, 2010; Simpson et al., 2015). Over interannual timescales, atmospheric pressure is dominant (Simpson et al., 2015).

2.1.2 Vertical Land Motion

Vertical land motion is an essential aspect of RSL change that must be considered at any coastal location of inquiry. Tectonically-driven land motion can have dramatic impacts on RSL on variable timescales. Earthquakes, for example, can cause immediate uplift or subsidence. If such movements occur in coastal areas, local RSL is affected (Nixon et al., 2009). Slower tectonic land-level changes related to plate boundary movements are also important, but generally only over very long timescales (Okuno et al., 2014).

Isostasy, meaning "equal standing" in Greek, is the term that describes the buoyant relationship between the Earth's lithosphere and the underlying mantle. In effect, the addition of mass to the Earth's crust (e.g. the build-up of an ice sheet) will cause it to sink into the asthenosphere (upper mantle). Crustal rigidity causes the loading to spread, which creates a peripheral depression beyond the outer margins of the load. Lateral displacement in the asthenosphere due to loading furthermore causes areas beyond the peripheral depression to experience uplift. A subsequent unloading, for example, the melting of an ice sheet or erosion of a mountain range, causes a reversal of these effects over time (Benn & Evans, 2010). Glacioisostatic adjustments and their long-lasting impact on RSL are discussed in further detail in the next section.

Two other forms of isostasy impact RSL change over the timescales relevant to this thesis: hydroisostasy and isostasy related to loading and unloading due to fluvial erosion, transport, and deposition (Benn & Evans, 2010). Hydroisostasy refers to crustal loading due to the changing distributions of water masses on continental shelves, for example, when ice sheets retreat and meltwater is added to the oceans, the extra weight of that meltwater over continental shelves can causes local depression of the crust (Benn & Evans, 2010). Erosion and deposition of rocks and sediment due to glacial-interglacial cycles or deltaic deposition, for example, redistribute mass from continental interiors via rivers, out onto continental shelves and beyond, which can result in large local changes in isostasy over century to millennial timescales (or longer; Benn & Evans, 2010). In Norway during the Holocene, glacio-isostasy is generally considered to be the most important driver of vertical land motion; contributions from other kinds of isostasy and neotectonics are thought to be few and highly localized (Simpson et al., 2015).

2.1.3 Glacial Isostatic Adjustment in Southern Norway

As stated in the previous section (2.1.2), vertical adjustments of the crust due to the growth and decay of glaciers is termed glacioisostatic adjustment (GIA). Glacial isostatic recovery (referred to as GIA in this thesis) is the period of uplift during and after deglaciation. Complete readjustment after unloading can take in excess of 10,000 years, meaning that any point of equilibrium is unlikely to be reached in a glacial-interglacial cycle (Benn & Evans, 2010). Glacial isostatic recovery can be subdivided into three periods. During the initial restrained rebound period, rates of uplift increase as the ice load is progressively removed via melting and thinning, but is not recorded in the geological/geomorphological record due to the presence of ice, and must therefore be determined through geophysical modeling. Next, unrestrained post glacial uplift is the rebound that takes place following deglaciation, and can be reconstructed with geological, biological, and geomorphological evidence. Finally, residual rebound is the future uplift that has not taken place yet (e.g. Fennoscandia is still uplifting at rates of up to 7 mm per year, and this is expected to slowly decrease over the next many thousands of years; Fjeldskaar et al., 2000; Benn & Evans, 2010). In Norway, most land areas still experience vertical uplift due to GIA, which is slowly diminishing with time. However, over decadal and centennial timescales, such movements can be thought of as essentially constant (Simpson et al., 2015).

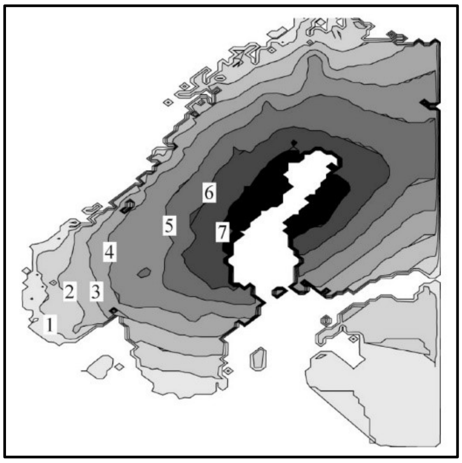

Figure 2.1 Observed rates of uplift for AD 2000, in mm/a calculated using data from tide gauges, precise leveling, GPS and gravity-measurements (Fjeldskaar et al. 2000). Figure adapted from Fjeldskaar et al. (2000).

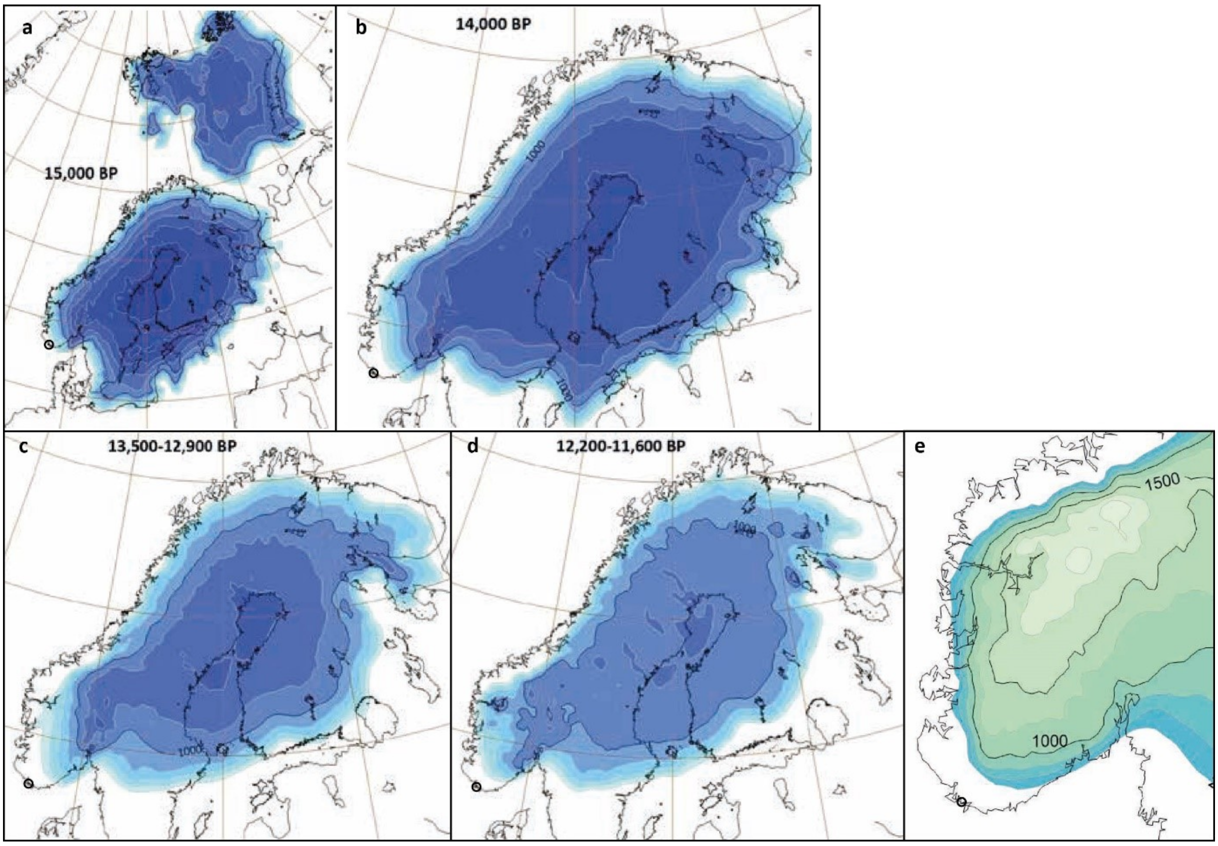

Figure 2.2 Figure adapted from Fjeldskaar & Amantov (2018) showing modeled ice extent and thickness. a) 15,000 years BP, b) 14,000 years BP, c) during the warm Allerød oscillation (~13,900– 12,700 BP) and, d, e) the subsequent Younger Dryas (~12,700–11,500 BP) cold period, when ice sheets and glaciers readvanced. Note that Tranevåg (encircled) remained ice free during these periods. For the complete set of figures of modeled ice extend and thickness during the late Weichselian (20,000 – 9,000 BP), the reader is directed to Fjeldskaar & Amantov (2018).

Measurements of rates of vertical land motion in Fennoscandia (Figure 2.1) are chiefly explained as GIA, resulting from the melting of the Fennoscandian Ice Sheet (FIS) during the late Weichselian (~20’000 – 9’000 BP; Fjeldskaar et al., 2000). Geophysical modeling shows that the FIS was thickest in the northern parts of the Gulf of Bothnia (Figure 2.2, Fjeldskaar & Amantov, 2018).

Based on modelling results presented in Fjeldskaar et al. (2018), Tranevåg was deglaciated approximately ~15,000 years BP (figure 2.2: a) and remained ice free during the Younger Dryas readvance (figure 2.2: d). Its peripheral position in relation to the late Weichselian ice sheet means the area experienced less loading during the late Weichselian and Younger Dryas readvance and consequently less GIA following deglaciation compared to areas of greater former ice sheet loading, farther inland (Fjeldskaar et al., 2018; Romundset et al., 2015). Present day uplift patterns from Kierulf et al. (2013) show a local uplift of about 1.5 mm/a near Tranevåg (Figure 2.3, as presented in Romundset et al., 2015).

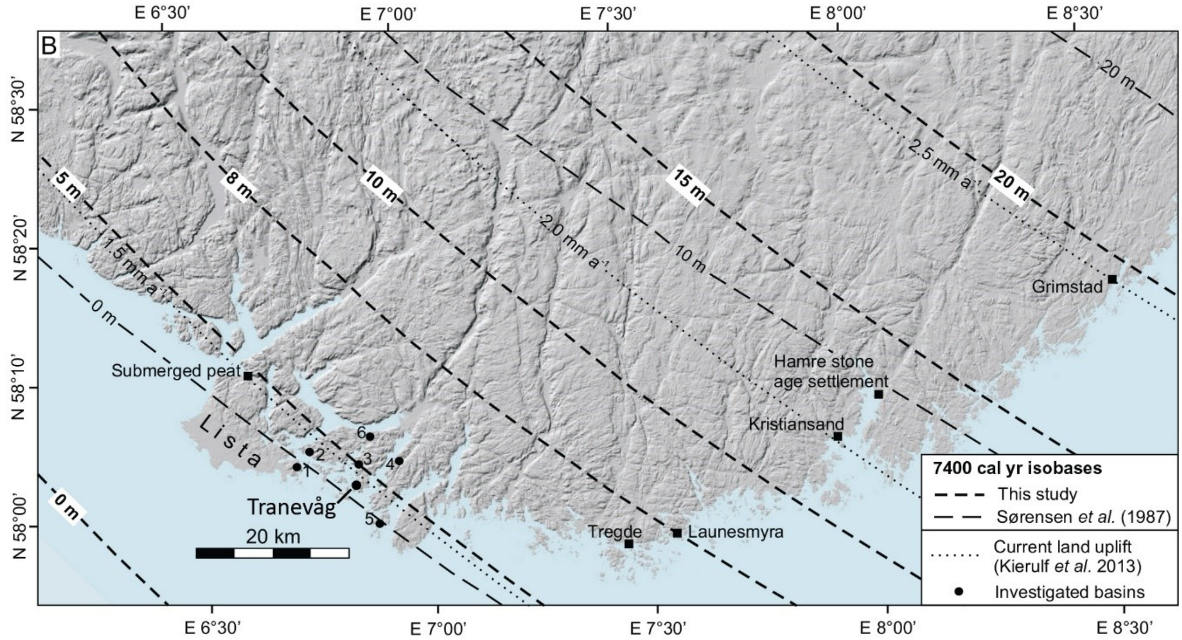

Figure 2.3 Map from Romundset et al. (2015) over the Agder region in southern Norway, showing two different interpreted 7400 cal yr BP isobases (shorelines) at the time of the Tapes highstand, around 7400 cal yr BP (Sørensen et al. 1987; Romundset et al. 2015). Contour lines showing current rates of crustal uplift from Kierulf et al. (2013) are also shown as dotted black lines. The black, numbered circles are the isolation basins used for the reconstructed RSL curve in Romundset et al. (2015) (presented in section 2.4.1; Figure 2.5) for the westernmost part of the former Vest-Agder region. This map also shows the location of the Tregde tide gauge. The location of Tranevåg is added to the figure, 2.8 km south of basin 3.

Generally, rates of vertical uplift around Tranevåg can be thought of as very slowly approaching zero, and that other processes may overprint GIA at shorter timescales both regionally (e.g. neotectonics activity) and locally (e.g. erosion, deposition and seasonal variability) (Fjeldskaar et al., 2000). However, at the timescales of the sediment cores presented in this thesis (~1000 years and ~3000 years), GIA is still most likely the dominant contributor to vertical land motion at a rate of approximately 1.5mm/a (Kierulf et al., 2013).

2.1.4 Storm Surges

During severe storm conditions, water levels can significantly exceed the astronomical tidal range, causing coastal flooding (Simpson et al., 2015). The difference between the normal tidal levels (predicted), and the measured water height is termed storm surge or storm tide (Holden et al., 2012). Storm surges may be dominant morphological agents at costal localities (Holden et al., 2012, Vis et al., 2015).

The severity of storm surges are determined by three key factors. First, the low atmospheric pressure of storms causes a local elevation of the water surface of approximately 1 cm for every millibar of decrease in pressure. Second, winds can exert significant pressure on a watermass, pushing it up against the coast, further elevating the water surface locally. Finally, coastal topography plays a key role in how storm surges develop. Low-gradient, funnel-shaped morphologies can significantly enhance storm surge heights (Holden., 2012).

2.2 Salt Marshes

Salt marshes are wetland areas that experience brackish conditions due to tidal inundation. These intertidal flats are highly productive ecosystems dominated by salt-tolerant vegetation species and host an abundance of terrestrial and marine biological life. Typically, salt marshes border freshwater environments (e.g. river mouth) that, in combination with tidal inundation, create varying salinity levels (brackishness) throughout the marsh system. Salt marshes are mainly found occupying the upper intertidal zone of relatively low energy environments in inlets, estuaries, lagoons and embayments along temperate coastlines. Where low-energy conditions persist over time, salt marshes can also be found facing the open sea (Schwartz, 2005).

2.2.1 Formation

In the lowest parts of the tidal range, inundation is frequent and salinities are high, meaning that growth conditions for vegetation are suboptimal. Accretion in these areas occurs through tidal deposition, mostly clays and silts, which results in the formation of depositional platforms known as mudflats. Salt marshes form where accreting mudflats are elevated higher up in the intertidal zone, where growth conditions are more tolerable and consequently colonized by salt tolerant vegetation (Schwartz, 2005).

Being positioned in the upper tidal range in sheltered locations, salt marshes are characterized by low-velocity currents due to the shallow waters and high rates of friction due to the vegetation. This friction facilitates a depositional preference towards finer grained, inorganic sediment, typically clays, silts, although fine sand to gravel can occasionally be deposited here during storms and heavy rainfall events. Most of the deposited sediments are subsequently reworked and modified by plant roots and biological activity (e.g burrowing of worms), making bioturbation a characteristic feature of salt marsh sediments. The *in situ* biological life also introduces a biological component to the deposited material. Tests, shells and skeletal remains from *in situ* organisms are commonly preserved and, roots and plant detritus from *in situ* vegetation may form peat as they accumulate and decompose (Schwartz, 2005).

2.2.2 Morphology

The topography of salt marshes include a multitude of small-scale features, such as tidal creeks, levees, cliffs, puddles and salt pans. The morphology of such features are controlled by factors such as: vegetation species and the extent of vegetation cover; availability and composition of sediments as well as the depositional and post depositional processes relating to these (e.g. compaction); tidal range, wave and current energy and general stability of the coastal area, and; the activities of *in situ* organisms (Schwartz, 2005).

Usually, the most noticeable feature of salt marshes is the network of meandering creeks and connected levees that channel the ebb and flow of tidal currents trough the marsh system. Typically, creeks are wide and shallow in early stages of saltmarsh development, becoming increasingly well defined as the salt marsh platform expands and develops trough continued accretion. The seaward edge of the salt marsh platform may take varying forms like an abrupt vertical microcliff, an irregular series of channels separated by ridges or a gradual transition into a mudflat (Schwartz, 2005).

2.2.3 Accretion Processes

Salt marsh accretion is a highly complex eco-geomorphic system, representing an interplay of biotic and physical processes (Kirwan et al., 2010). The physical processes (e.g. tidal currents and surface wash) mainly serve to transport and deposit silts, clays and organic matter from outside the marsh itself. Tides and storm surge tides typically represent the major transportation vector for the sediments to the marsh surface (Kirwan et al., 2010). However, rainfall-induced surface wash and floodwater (e.g. from a nearby river) can be significant contributors. The biotic processes introduce organic material via the *in situ* biological life in the marsh, mostly plant roots and detritus. Collectively, this combination of biotic and physical processes result in a gently sloping depositional platform, usually between mean high water spring (average of high water heights occurring after a new or full moon when the tidal range is largest; Shennan et al., 2015) and mean tidal level (Schwartz, 2005; Kirwan et al., 2010).

The importance of different depositional processes varies from site to site. In areas/periods of very low tidal energy or sediment availability, regular tides are not major depositional contributors and storm tides might deliver most, if not all sediments to the marsh surface due to the low potential for sediment suspension and erosion by regular tides (Müller-Navarra et al., 2019).

When tidal currents approach the intertidal zone, their energy is attenuated by friction generated by the marsh surface and marsh vegetation and/or settling of wind and waves, causing suspended sediments to be deposited. Wave backwash and tidal ebbing exert potentially erosional/remobilizing forces on the deposited sediments, however, friction with salt marsh vegetation imposes a limitation on this force. Storm surges deposit sediments onto salt marsh surfaces in the same way, but with a longer inland reach and generally higher temporary sediment influx (Müller-Navarra et al., 2019). Surface wash and flood waters transport and deposit material from the watershed/hinterland, introducing a sediment influx from the inland border of the marsh system. Whereas regular tides only allow accretion within the tidal range, storm surges, surface wash and flood waters facilitate sediment deposition above the mean high tidal level.

The ability of salt marshes to cope with rising RSL has been a matter of great debate (e.g. Kirwan et al., 2010). Salt marsh accretion rates in the North Atlantic vary from < 0 mm/yr (indicative of erosion) to > 10 mm/yr. Most tend to be at an accretion balance with an accretion rate minus the local rate of RSL rise equal to -1mm/yr to +2 mm/yr. Nonetheless, most of the balanced salt marshes are expected to experience submergence in the coming decades as rates of RSL rise increase (Crosby et al., 2016). Kirwan et al. (2010) argue that the ability of a salt marsh to cope with rising sea levels depends on a range of non-linear feedback mechanisms between inundation, plant growth, organic matter accretion and sediment deposition, with the concentration of suspended sediment and tidal range being the key determinants in salt marsh survival in the coming decades (Kirwan et al. 2010). Marshes that are submerged for longer periods of time during daily high tide(s) exhibit higher rates of deposition. This might counteract the predicted submergence of many salt marshes (Kirwan and Megonigal, 2013; Crosby et al., 2016; Müller-Navarra 2019). Nevertheless, only salt marshes where tides have high suspended sediment concentrations are likely to remain stable during rapid rates of RSL rise caused by melting of the ice sheets (Kirwan et al., 2010).

Different vertical zones in salt marshes are impacted differently by storm surges. In the low marsh (see next section), storm strength is the most important factor in determining sedimentation rates, while storm frequency is more important for sedimentation rates in higher marsh zones (high marsh and upper high marsh; see next section). Some modelling results have shown that an increase in storm surge frequency can increase depositional rates and thereby strengthen the ability of salt marshes to keep up with sea level rise, given adequate sediment supply (Kirwan et al., 2010; Schuerch et al., 2013).

2.2.4 Vertical Zonation

Vis et al. (2015) divide low energy, fine grained, coastal environments (e.g. salt marshes) into three main zones: the permanently submerged *subtidal zone,* which is a subaqueous environment below the neap low tide water level (lowest water level during the tidal cycle where the tidal range is lowest); the *intertidal zone* that is emerged during neap tide and submerged during spring high tide, and; the *supratidal zone,* which is a terrestrial environment above spring tidal level that is only occasionally flooded during storm surges. They further subdivide the intertidal zone. The *low tidal flats* subzone is emerged only during the lowest tides. The *middle tidal flats* subzone is regularly inundated and exposed during every tidal cycle. And finally, the *high tidal flats* subzone is briefly inundated during higher tides (Vis et al., 2015)

In intertidal and supratidal zones sediments are typically a combined product of waves and currents moving sediment, forming ripples and crossbedding. Bedding I often not visible in muddy sediments due to bioturbation and paedogenic alterations (Vis et al., 2015). Wave and current energy decrease from the subtidal through to the supratidal zone due to increasing friction with the surface and vegetation. This generally results in a fining of tide deposited sediment grain size with increasing elevation as the larger grain sizes are deposited when the energy of the transportation medium decreases. In the lower tidal flats, salt marsh vegetation can form thin peat beds. The brackish and freshwater vegetation in the middle and higher tidal flats might form thicker clayey-peat beds (Vis et al., 2015).

2.2.4.1 Species Zonation

As mentioned, salt marshes are productive ecosystems for both marine and terrestrial species. However, the physiological (e.g. cyclical shift between inundation and subaerial exposure) and ecological stress (e.g. varying salinity) of the intertidal zone causes a characteristic low species diversity. The salinity levels and frequency and duration of inundations are highly related to elevation. In most salt marshes these vary from near marine to near terrestrial levels. As such, the physiological and ecological conditions within the marsh vary significantly with elevation, resulting in distinct zones characterised by highly specific tidal exposures and brackishness. Consequently, specific species inhabit specific elevational ranges where conditions are tolerable. This leads to an elevational zonation of species within salt marshes (Schwartz, 2005), and is often visible by eye and in infrared aerial photography in relation to vegetation species (e.g. section

2.4.2; figure 2.9). In marshes with a low tidal range (e.g. < 50cm), zonation can be compressed (e.g. Alve and Murray., 1999).

Foraminiferal zonation (discussed in section 2.3.6) is often categorized into high marsh, middle marsh and low marsh based on tidal elevations. Where foraminiferal assemblages allow, further subzones can be applied (e.g. upper high marsh) (Edwards and Wright., 2015).

2.3 Analytical Concepts

2.3.1 Core Chronology

2.3.1.1 Lead Pollution History

The dangers of pollution from heavy metals and other potentially harmful elements to human health and the environment have raised a worldwide concern for industrial practises. In a European context, the pollution legacy of industry and the effects of guidelines and regulatory practises have fostered the emergence of environmental forensics (Croudace et al., 2015). Lead (Pb) was among the first recognized environmental pollutants that was produced by humankind. Among others, its behaviour in air, water and soil has since been granted a lot of attention. It's emergence as a pollutant has accompanied many technological developments that are vital for our current society (e.g. smelting, mining, gasoline-powered engines) (Steinnes et al., 1997).

Lead pollution is often emitted as small particles into the atmosphere, giving it a substantial potential for long range travel before settling (e.g. from mid latitudes to the arctic). A typical scenario enabling long range transport of some heavy metals (e.g. Zn, As, Se, Cd, Sb, Pb) is the release of the metal in a volatile form at the pollution source followed by adhesion to high surface-to-mass aerosols. Because of the air-bourne travel potential, and a great number of emission sources worldwide (e.g. gasoline powered vehicles), lead is now a global pollutant. This means that most anywhere in the world, there is a background concentration of lead in the environment from current and historical anthropogenic sources (Steinnes et al., 1997).

Steinness et al. (1997) suggest that the concentration pattern of Pb in Norwegian soils is predominantly characterized by long range transport, emphasising that regional differences in undisturbed soils are unable to account for this. They emphasize that pre-industrial concentration levels did not exceed 20ppm in any region of Norway. They also point out that they found no indications of local point sources or automobile traffic contributions to the lead concentrations. From this they concluded that most of the anthropogenic lead in Norwegian surface soils is supplied from pollution sources abroad (Steinnes et al., 1997).

Studies on lead concentrations in Norwegian soils (e.g. Berthelsen et al., 1995; Steinnes et al.,1989; Steinnes et al., 1997), show that anthropogenic sources are dominant, effectively overprinting any natural variations. A beneficial aspect to the otherwise tragic environmental damage caused by the industrialization of human society is that variations in Pb concentrations reflect the pollution history of Pb, which is documented and dated in Greenland Ice Sheet (GIS) ice cores (McConnell & Edwards, 2008). As such, the Pb pollution history, particularly in post industrial times can be applied to Pb concentrations in a sedimentary record and help establish chronology (Rizzo, et al., 2009).

In a study of GIS ice cores by McConnell & Edwards (2008), Pb concentrations were found to be low between 1772 and 1860 (dates given in AD). From 1860 concentrations began to increase and accelerated sharply from 1887. The first peak concentration was reached in 1893 (~20 times the pre-1860 average), followed by a highly variable period until 1915, when concentrations declined sharply, reaching a minimum in 1931 during the post WWI period (great depression). Concentrations remained low but increasing until 1949 when the widespread use of leaded gasoline resulted in a sharp increase, remaining high until the second peak in 1970. Following regulations on lead emissions, concentrations decreased between 1971 and 1991 by up to 85%, approaching pre-industrial levels (McConnell and Edwards, 2008).

2.3.1.2 Tephrachronology and Screening

Tephra is a layer of rock, dust and ash from an explosive volcanic eruption. Coarser particles are deposited close to the volcano vent, whereas the smallest particles can be deposited over 1000 kilometres away. Proximal to volcanic eruptions, tephra layers can be millimetres to centimetres thick and often visible to the naked eye, making them relatively easy to identify. At distances greater than 1500 km from the source, shards can be smaller than 10 microns. The resulting layers, termed *cryptotephra*, are usually invisible to the naked eye and can be as thin as two shards thick (Kylander et al., 2011). *Tephra stratigraphy* is the study of sequences of tephra layers, related deposits, sources and ages (Mayhew, 2015). *Tephrochronology* is a tool for dating and correlating sediment cores, where layers of glass shards emitted by volcanic eruptions can be used as isochronous markers (Kylander et al., 2011).

Locating tephra layers in sediment cores is normally accomplished using a combination of methods including, sieving, point counting, magnetic susceptibility measurements, reflectance variations and density separation techniques (Kylander et al., 2011). X-ray fluorescence (XRF) has been used in recent years as an efficient pre-screening tool to narrow down the probable location of cryptotephra layers in sediment cores (Kylander et al., 2011). For tephra layers to be detectable in an XRF dataset, the shard concentration needs to exceed a critical threshold to be detectable by the x-ray beam. Kylander et al. (2011) found multiple rhyolitic tephra layers with low concentrations of <864 shards/cm^3 that were undetectable with XRF, whereas basaltic tephra layers of ~1000 shards/cm^3 were detectable. In addition to demonstrating the existence of a critical threshold in terms of layer thickness, this finding also shows that the geochemistry of tephra layers influences the efficiency of XRF-detection (Kylander et al., 2011).

The signal of cryptotephra layers in the elemental profiles of an XRF dataset can be inflated or distorted by its surrounding matrix. Sediments with contrasting geochemistry in relation to tephra (e.g. diatom-gyttja) is optimal. On the other hand, sediments with similar geochemistry to tephra makes this method more difficult (Kylander et al., 2011). It is also not uncommon for tephra layers to be patchy due to uneven depositional processes, and might be reworked by, for instance, sedimentation processes and bioturbation. Multiple volcanic eruptions might give concentrations of glass shards throughout larger segments of a core that are hard to differentiate and pinpoint to a specific location in the core (Kylander et al., 2011).

2.3.2 Sea Level Indicators

Sea level indicators are biological, geological, archaeological, or geomorphological features that can be tied to former sea level heights. For example, preserved assemblages of organisms that only live within a specific elevation above or below the contemporaneous mean sea level; archeological features such as harbors, and; morphological features related to a specific sea surface height, such as erosional platforms created by wave action. A sea level index point is a sea level indicator that has four, precisely defined attributes: geographic location, age, elevation and tendency (Shennan et al., 2015).

The geographic location is the coordinates of the indicator, typically in relation to a national reference grid and/or latitude and longitude. The age of the indicator is commonly derived from calibrated radiocarbon measurements of in situ organic material at or near the indicator. For elevation, the indicative meaning of the indicator is the key aspect. The indicative meaning is the combination of a reference water level and indicative range. The reference water level is the elevation at which a modern equivalent of the indicator occurs in reference to a tidal level. The indicative range is the elevational range at which this modern equivalent occurs. Shennan et al. (2015) explains this using barnacles as an indicator. In their example, the upper limit of barnacles is around the mean high tide (reference level) and varies with about ±30cm in elevation (indicative range). As such, barnacles indicate a past RSL at mean high tide ±30cm. The tendency relates to if the indicator indicates an increase or decrease in marine influence. For instance, finding barnacles at a higher elevation than present-day RSL indicates a decrease in marine influence over time.

Using sea level indicators to reconstruct precise former RSL heights is beyond the scope of this thesis and is therefore not discussed in further detail. However, to determine the timing of the onset of RSL rise, as indicated by the local tide gauge at Tregde, interpretations of the vegetational environment that sediments originate from are used as sea-level tendency indicators (section 5.3).

2.3.3 Preserved Plant Remains

Plant species are highly sensitive to their environment. In salt marshes, zonation of vegetation occurs mainly because of differences between plant species' tolerance to salinity and ground water levels. Plant macrofossils (hereafter referred to as preserved plant remains and visible organic matter/fragments) are defined as plant remains, which can be seen with the naked eye, encompassing a wide variety of preserved remains such as roots, leaves, woody parts (twigs), etc. (Waller, 2015). The identification of preserved plant remains, and determining their stratigraphic position, can provide invaluable information on paleoenvironments and therefore RSL movements. For example, *in situ* fragments of vegetation from, for instance, terrestrial environments, in modern intertidal zones demonstrates RSL change over time (Waller, 2015).

Whereas pollen has the ability of relatively long-range travel, preserved plant remains can generally be assumed to be indicators of local presence. The analysis of preserved plant remains is also less technically difficult than of pollen, and does not require expensive equipment compared with most other RSL proxies (Waller, 2015).

Although plant communities in intertidal environments are strongly affected by the tidal regime and are thus zoned according to elevation with respect to msl, there is considerable geographic variation in the species composition of these. The nature of the underlying sediment, freshwater variability and land use of the marsh itself, as well as proximal and hinterland areas, can all have a significant environmental influence on plant species zonation. Therefore, knowledge of local plant ecology is a prerequisite for detailed analysis. Furthermore, the production and dispersal of preserved plant remains is highly variable. A large quantity of sediment is often required as preserved plant remains often are produced in small quantities (Waller, 2015). Moreover, the destruction of plant remains due to decomposition and transport of above-ground remains by tidal currents and surface wash are obvious limitations for this method. The humification process is also often enhanced in intertidal areas due to oxidation by fluctuating water-levels (Waller, 2015).

Above-ground parts of vegetation usually decompose, resulting in sediment consisting largely of roots and rhizomes. Where this is the case, it can be assumed with a strong degree of certainty that the plants grew in situ. However, the downward growth of roots can introduce younger plant remains in the sediment underneath, resulting in mixed assemblages of plant communities with different environmental tolerances. Particularly roots and rhizomes from *Phragmites* species (large reed species) cause this and are a common feature of coastal sediments. These mixed assemblages are most likely to occur close to sedimentary boundaries. Furthermore, if sedimentary facies (e.g. peat) is overlain by, for instance, a marine or brackish environment, or followed by a period of little sedimentation, younger material may be introduced by burrowing organisms. Because of these bioturbation processes, it's important to consider their influence when assessing if any sedimentary facies is transitional or just a mixed assemblage (Waller, 2015).

With the help of preserved plant remains, sediment core data can be interpreted as progressive or regressive through time (figure 2.4). Progressive and retrogressive series are defined here as successions of preserved plant remains in stratigraphic sequence that indicate an increase or decrease, respectively, in the vertical position of the sediment surface relative to ground water level and tidal heights (i.e. RSL) (Waller, 2015).

The vegetation zones illustrated in figure 2.4 provide an idealized example of the nature of the sediment that results from different vegetation and tidal regimes. For example, mudflats have generally no, or very scant, rooted vegetation. The sedimentary facies in such environments therefore can be characterized by clayey and/or silty organic-rich mud. This is very similar to the expected sedimentary facies from salt marsh sediments, however; the low growing vegetation leaves behind fragments (most commonly roots), and makes the distinction possible if decomposition is partial (i.e. roots still present in recognizable form). Reedswamp facies usually consist of clays, silts, roots and/or detrital peat from reeds, which is relatively easy to distinguish from saltmarsh and mud flat sedimentary facies (Waller, 2015).

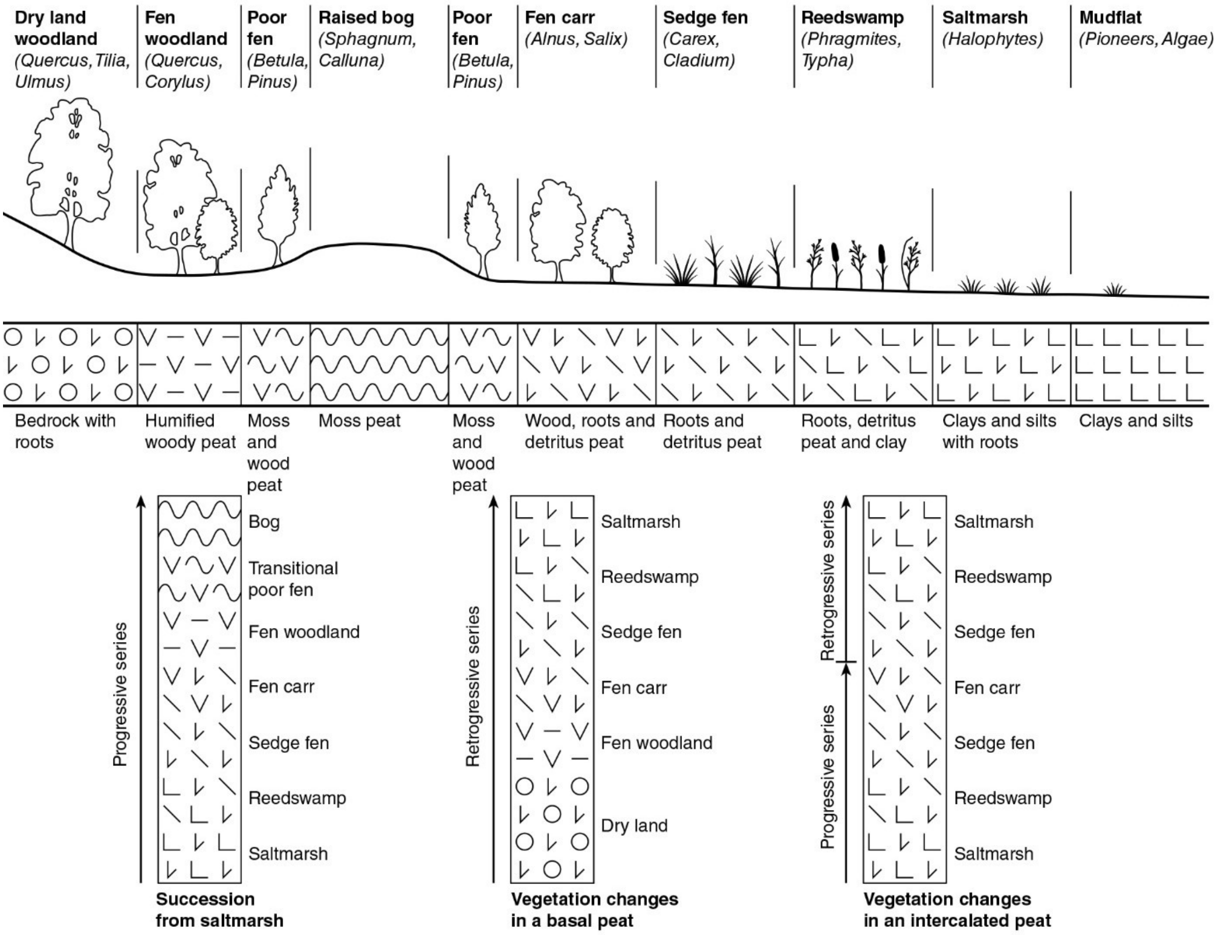

Figure 2.4 “Idealized natural coastal vegetation zonation for northwestern Europe showing characteristic taxa, the nature of the sediments deposited and likely conformable stratigraphic relationships.” (Figure from Waller, 2015, p. 187).

A sedimentary sequence going from mudflat to saltmarsh and reedswamp sediment facies, respectively, is a good example of a progressive series, indicating an increase in elevation of the sediment surface in relation to MSL. The reverse of this sequence is indicative of a retrogressive series. This is, however, an idealized example, and sedimentary sequences are often more complex. For instance, fluctuating RSL and/or groundwater would cause multiple progressive and retrogressive series. Accretion rates are also different during RSL rise and fall, which affects the ratio between *in situ* organic and deposited material and, may significantly differentiate facies from the same vertical vegetation zone. Differential decomposition conditions can also significantly diversify facies. Tectonic events and erosion can cause abrupt changes, skipping one or more vegetation zones and/or remove facies from the sequence. Still, evaluating the impact of vegetational zonation on sedimentary sequences can be of critical importance in sea-level studies based on sediment cores (Waller, 2015).

2.3.4 X-Ray Radiography

X-Ray radiography is a helpful technique for identifying primary and secondary structures in sediment cores that has been used in sediment studies since 1962 (e.g. Hamblin, 1962; as stated in Bouma, 1964). Sediment-core radiographs are produced by passing x-rays through the sediment. While passing through the sediment, part of the radiation is absorbed by the individual particles that the x-ray passes through. The non-absorbed radiation is recorded on the other side of the sediment and used to produce a radiograph-image. As x-rays follow straight paths, the remaining radiation reflects the sorption qualities of all particles between the point of emission and recording device. The resulting x-ray image will reflect differences in the radiation sorption qualities of the sediment throughout the sediment core. Perfectly homogenous sediment would produce a blank x-ray image (Bouma, 1964).

Lithological properties like variations in grainsize between sands, silts and clays might be discernible as sandy grainsizes generally absorbs more or the x-ray radiation. A darkening in the x-ray might then reflect a coarsening in grainsize. Denser sediments will also appear darker because the x-ray beam passes through more particles than less dense sediments. However, different minerals vary in their sorption qualities and a darkening might therefore reflect a change in the mineralogical composition. Plant remains, for instance *in situ* roots, absorb less radiation than sediments and appears as brighter traces contrasting the darker surrounding sediment. Burrows from *in situ* organisms might also appear as bright traces or ovals depending on the direction of the burrow. X-ray images are useful in sediment core studies, however, care is needed when interpreting. Prominent features, for instance cracks, might reflect operational errors rather than the properties of the studied sediment (Bouma, 1964).

2.3.5 X-Ray Fluorescence

When climate change and pollution were recognized as serious environmental and political concerns in the 1980s, the demand for rapidly acquired, high-resolution data from whole sediment cores to investigate changing environmental conditions heralded the development of X-ray fluorescence (XRF) core scanners. As the technology and methods were further developed and refined, and became increasingly available and affordable, the number of sediment core studies using XRF technology grew almost exponentially, especially from the mid 2000s, and it is now a well established and widely used method in sediment core studies (Rothwell and Croudance, 2015).

X-ray fluorescence presents a rapid way of producing detailed data that are very useful in identifying and describing lithological units and textural/mineralogical variations, even where they appear similar visually. The usefulness of elemental profiles as proxies for Earth processes was recognized prior to the development of XRF-core scanners, however, the number of recognised elemental proxies have since been extensively expanded upon as data collection became more rapid and accessible. Such elemental proxies have been established as important indicators of, for instance, climate change, anthropogenic pollution, weathering, erosion, reducing conditions, organic productivity and water mass changes (Rothwell and Croudace, 2015). Discrete events often cause abrupt changes in XRF-derived elemental profiles, that can usually be characterized and identified based on their elemental composition (e.g. tephras, discussed in section 2.3.1.2; Rothwell and Croudace, 2015; Kylander et al, 2012).

2.3.6 Elemental proxies

The basis for using elemental proxies for studying Earth processes and environmental conditions is that variations in one or a combination of elemental profiles vary in accordance to the process or condition of interest. If such a relationship can be established, the elemental profile can be used as a proxy for variations in the process or condition of interest, thereby indicating how the process or condition has changed through time (Rothwell and Croudance, 2015). A classic case is determining changes in hinterland climate based on depositional processes where, for instance, aeolian and fluvially derived deposits have different geochemical compositions (e.g. Hanebuth & Lantzsch, 2008) (Rothwell and Croudance, 2015).

Importantly, elements relationships to processes can be highly site specific and vary between sites. This is exemplified by the multiple uses for any one element in the expansive XRF literature summarized by Rothwell and Croudance (2015). Determining what variations in elemental profiles reflect is very much an exercise in system thinking where erosional, depositional, weathering and biological processes as well as source areas of deposited material form a complex interplay and might affect the elemental composition of sediments. Hence, formulating statements about such relationships should be done with care, and interpretations require consideration of the site-specific system.

In their chapter on XRF core scanning of marine sediments, Rothwell and Croudance (2015) compiled some 60 elemental integrals and ratios that have been used in paleoenvironmental or process studies in a marine context. This summary has directed the selection of the elemental proxies used in this thesis, and are described briefly, below.

Calcium (Ca) is a commonly used elemental proxy in palaeoenvironmental reconstruction. It may be deposited as detrital sediment, but biogenic sources are usually of volumetrically greater importance (Rothwell and Croudance, 2015). This is because many large groups of marine plankton, for example, foraminifera and coccoliths, form their tests out of $CaCO_3$. Because of this, Ca is recognised as a well-established proxy for oceanic productivity where variations in Ca usually reflect $CaCO_3$ stratigraphy in pelagic cores. Detritally-sourced Ca is important in near shore and estuarine environments, where carbonate bedrock is present (Rothwell and Croudance, 2015).

Over glacial – interglacial timescales, Ca is often a good climatic indicator and an effective proxy for establishing a stratigraphic framework, where biogenic production of Ca is typically low during glacials and comparatively high during interglacials. In this context, Ca typically anticorrelates with terrigenous elements (e.g. Fe) (Rothwell and Croudance, 2015).

The main limitation of using Ca as an elemental proxy is that Ca variations can reflect dilution by terrigenous material rather than variations in biogenic productivity (Rothwell and Croudance, 2015). Moreover, low concentrations of Ca might reflect carbonate dissolution (e.g. removal due to low pH). Detrital Ca can be indicated by its covariance with terrigenous elements (e.g Fe, Ti) (Rothwell and Croudance, 2015). Covariation with strontium (Sr) may indicate that most of the Ca is of biogenic origin, since calcifying organisms typically fix Sr in addition to Ca to their tests. Where both biogenic and detrital Ca are present, these can often be distinguished by the Ca/Sr ratio (Rothwell and Croudance, 2015).

Compared to glacial – interglacial timescales, the timescale studied in this thesis is several orders of magnitude smaller, reducing the usefulness of Ca as a climatic proxy of marine productivity. Furthermore, because of the terrestrial to marginal marine environment of salt marshes, any changes in marine productivity are unlikely to be detectable using XRF data. However, in a salt marsh setting, where calcareous foraminifera tend to inhabit the more marine zones and agglutinated (non-calcareous) foraminifera tend to inhabit the brackish zones (Edwards and wright, 2015), changes in total abundance of Ca could potentially help distinguish between marine and brackish facies.

Titanium (Ti) predominantly occurs in the mineral form, TiO_2 and generally varies directly with the coarse terrigenous grainsize fraction. It is commonly found in rocks such as gneiss and schists and therefore, often indicates a terrigenous continental source. Concentrations may increase with biotite enrichment. It is not involved in any organic processes and can thus be regarded as representing minerogenic allochthonous inputs (Rothwell and Croudance, 2015).Titanium can be used to record sediment delivery through runoff. In that context it has been used to asses hinterland climate, particularly rainfall (e.g. Haug et al., 2001). In addition to runoff, Ti can be used as a proxy for aeolian inputs such as tephra and dust (e.g. Sluijs et al., 2008; Rothwell and Croudance, 2015). A limitation of using Ti is its tendency, like many other elements, to increase with depth due to compaction and decrease towards core tops due to lower compaction. Ti concentrations can also be offset by variations in grainsize as it tends to be more abundant in coarser grain-sizes (Rothwell and Croudance, 2015).

Iron (Fe) is the fourth most abundant element in the earth's crust. It usually has a high abundance, high signal to noise ratio and a high signal relative to other elements. This has made Fe a commonly used proxy in environmental and process studies. Generally, variations in Fe concentrations relate to the terrigenous fraction and, in marine settings, changes in carbonate/clay ratios. Iron also commonly correlates with other terrigenous markers like Ti. However, Fe is redox sensitive, meaning that Fe can be mobilised in oxidized conditions, distorting its relationship with other environmental processes. Therefore, using Fe as a proxy for terrigenous sediment supply should be conducted in conjunction with other terrigenous proxies like Ti (Rothwell and Croudance, 2015).

Potassium (K) is often associated with terrestrial siliciclastics, illite clays and potassium feldspars. In fine grained sediments, a high concentration of K can often be attributed to a high illitic component. K may be used as an indicator of terrigenous input, often used as a proxy for fluvial input (Rothwell and Croudance, 2015).

By mass, Silicon (Si) is the second most abundant element in the earth's crust (27.7%) after Oxygen. Silicate minerals are the largest group of rock forming minerals, comprising about ~90% of the earth's crust. Because of its abundance, Si can be derived as detrital material from mechanical weathering, and therefore reflect terrigenous detrital sediment deposition. However, Si can also be derived from a range of organisms, for instance siliceous pythoplankton (e.g diatoms). Distinguishing between terrigenous and biogenic Si can be helped by normalising with a terrigenous divisor such Ti (Rothwell and Croudance, 2015).

Sulphur (S) resides in the biomass of marine plants and as mineralized S in their dead remains. In this way, S is closely associated with organic matter. Organically sourced S may return to seawater through oxidation, or remain in various forms, susceptible to bacterial reduction. In marine settings, S may serve as a proxy for oxygen depletion of bottom waters where it has undergone a reduced iron-sulphate phase and been bound to organic rich mud layers. Together with other suboxic indicators (e.g. Fe), high S concentrations may indicate reducing conditions (Rothwell and Croudance, 2015).

In reconstructing past tsunamis, Chlorine (Cl) has been used as a chemical proxy for seawater as it is a common component of sea salt (Chagué-Gott et al. 2012).

Zirconium (Zr) chiefly occurs as the dense and resistant mineral Zircon ($ZrSiO_4$), which is ubiquitous in the Earth's crust. In sediments Zr is usually a product of weathering of igneous rock. As Zircon is resistant, it usually maintains it morphology during weathering and transport and is therefore associated with coarser grain-size fractions (Rothwell and Croudance, 2015). Zirconium has also been associated with volcanically sourced material in provenance studies, and with tephra layers (Rothwell and Croudance, 2015; Hunt, 2017).

2.3.6.1 Uranium

Increases in the concentration of uranium (U) in salt marsh sediment cores may be a useful tool for identifying and describing peat/peat-like facies due to peats excellent sorption qualities (outlined below; Brown et al., 2000; Ahmad et al., 2015) and a relatively high concentration of solved u in seawater (Shvartsev, 2008; discussed in appendix 1), and areas with exposed granitic bedrock and short weathering histories (e.g. deglaciated during the late Weichselian; Banks et al., 1988; Discussed in appendix 1).

Peat formation starts with initial inhibited physical and biological breakdown of plant detritus in waterlogged environments, such as marshes, bogs and swamps. The vegetation is then slowly oxidized by micro-organisms to form peat. This biochemical metamorphism normally occurs in the top meters of sediment. Over time, this then results in sediment facies that is mainly comprised of partially decomposed vegetation. However, the precise composition is dependant on factors such as vegetation type, climate, acidity of the water and the degree of metamorphosis (Brown et al., 2000).

Peat has gained significant attention as a sorbent for dissolved metals in the context of waste water treatment. It has also been confirmed that peat bogs have the ability to retain heavy metals (e.g. Pakarien et al., 1981; Glooschenko and Copobianco, 1982; Brown et al., 2000). Peat has several characteristics that facilitate the sorption of dissolved metals, such as the production of specific acids during humification, high porosity and a large surface area. Ion-exchange is believed to be the most important mechanism for sorption of metals onto peat (Brown et al., 2000). The sorbtion capacity and rate is dependent on peat type, but also affected by other factors. For instance, pH plays a crucial role in the sorption rate. Optimal pH for sorption varies depending on the specific metals but, is usually between 3.5 and 6.5. Furthermore, loading rates affect the sorption rate where increasing loading rates generally decrease the sorption rate. The presence of multiple metals in the water might also cause competition for available adsorption sites favouring ions with higher affinity for sorption, however the sorption capacity might also increase (Brown et al., 2000).

In controlled experiments by (Ahmad, 2015), peat (type not disclosed) sorbed >99% of U in highly contaminated water within 24 hours. His thesis demonstrates that, at least certain types of peat are excellent at sorbing U rapidly and in high concentrations. Assuming a stable supply of U from sea and groundwater over time, U should generally reflect the sediments sorption capacity, being highest in peat facies. Therefore, as the sorption capacity of peat is largely attributed to its organic matter content (Brown et al., 2000), U concentrations may reflect the vegetative organic matter fraction of sediments.

2.3.7 Foraminifera

Foraminifera are microscopic, single-celled organisms inhabiting a wide variety of marine and brackish environments. They form hard shells called "tests" made from calcareous material or grains held together with organic cement with an interior organic "lining" (agglutinated tests), both of which have good preservation potential when buried. Their often, high abundance and sensitivity to environmental factors, makes them a favourable indicator of past environmental conditions (Edwards and Wright, 2015). Pioneering work on oxygen isotopes in calcareous planktonic and benthic foraminifera started as early as 1950s, revealing an isotopic signature that reflects the physio-chemical properties of the surrounding seawater and was famously linked to the growth and decay of terrestrial ice sheets over glacial-interglacial timescales (Edward and Wright, 2015).

2.3.7.1 Intertidal Foraminifera in Sea Level Research

Salt marsh deposits are clear indicators of marginal marine environments since they accumulate within and just above the intertidal zone. Reconstructing sea level heights solely based on the presence of salt marsh peat can yield large error margins depending on the local tidal range and the range in elevation between the lowest (Low Marsh) and uppermost (Highest High Marsh) surfaces. Therefore, differentiating the marsh deposits and determining their vertical position above or below MSL at the time of deposition increases the accuracy of reconstructions significantly. The vertical zonation of salt marsh foraminifera within the tidal range, coupled with their high abundance and preservation potential, makes them a solid tool for differentiating marsh sediments and determining how high in the intertidal zone the sediment accumulated (Scott and Meliodi, 1978; Edwards and Wright, 2015). Salt marsh vegetation also exhibit strong tendencies for vertical zonation, however these are comparatively poorly preserved in the low pH environments that are characteristic of subsurface salt marsh sediments, making them less suited for analysis (Scott and Medioli, 1978).

Intertidal foraminifera have a history in sea level research going back to the 1970s. They are now a popular means of bridging the gap between short instrumental records and geological data, making them a central part of evaluating recent changes in RSL (Edwards and Wright, 2015). Seminal work in the 1970s and 1980s by David Scott and colleagues observed that distinct assemblages of foraminifera in salt marshes characterize certain height intervals within the tidal zone. (as stated in Edwards and Wright, 2015) Based on this pioneering observation, abundant empirical evidence has been gathered in later works, establishing that saltmarsh foraminiferal species assemblages tend to correlate with tidal elevation. This kind of vertical zonation of taxa is a common feature of saltmarsh and mangrove environments regardless of differing climate, salinity, vegetation and tidal regimes (Edwards and Wright, 2015).

Within the intertidal zone, changes in relative sea level cause changes in salinity, vegetation, and decreasing inundation with increasing elevation. In turn, this directly affects the environment of existing foraminiferal species, causing changes in type of species and species abundance within local assemblages. This is related to the fact that certain species of foraminifera tolerate a limited range of salinity values, making them highly sensitive to changes in RSL. For example, a rise in sea level would create a more saline environment. This will, in turn, cause a change in the local species assemblage where more salt tolerant species thrive, and less salt tolerant species decline in abundance, disappear, or migrate to more elevated parts of the marsh where conditions are more favourable (Edwards and Wright, 2015).

Because some of the most dominant factors influencing foraminiferal species assemblages are directly determined by RSL, sea level heights can be inferred for the time of deposition. This makes foraminifera useful sea-level indicators for determining local sea level changes over short timescales where they are preserved in a sedimentary record. Still, it is important to note that sea level in and of itself does not determine foraminifera species assemblage, but rather influences a range of important factors (e.g. salinity, vegetation, circulation of water). Other factors that are independent of sea level, such as creeks, precipitation and local geology, can also strongly influence the local environment and therefore, local species assemblages. Using intertidal foraminifera as sea level indicators implies the assumption that the local species assemblages are mainly determined by factors controlled by RSL, and not offset (in any meaningful way) by factors independent of sea level (Edwards and Wright, 2015).

From early studies, two aspects of the distribution pattern of foraminifera in salt marshes are of particular significance for foraminifera-based sea level reconstructions. Firstly, Scott and Medioli (1978) observed that the total abundance of foraminifera individuals was highest in the upper limits of marine influence, with a marked decrease and eventual absence around the high-water mark. This occurrs even where freshwater input and seawater raised by capillarity create a humid and mildly brackish environment and therefore, theoretically good living conditions for foraminifera. This suggests that marsh foraminifera require some tidal activity for their survival, meaning that they are highly unlikely to be found above the high-water mark, even in marsh-like sediments (Scott and Medioli, 1978).

Secondly, there is a bipartite split between high marsh and low marsh foraminiferal assemblages. High marsh assemblages are dominated by agglutinated species whereas lower marsh assemblages are characterized by foraminifera with calcareous tests. This divide is broadly coincident with the divide between vegetated saltmarsh platform and unvegetated tidal flats. Although not universal, a transitional zone is commonly observed with a combination of the agglutinated species *Milammina fusca* and calcareous taxa (Edwards and Wright, 2015).

Scott and Medioli (1978) underline that the differentiation of high marsh sediments results in the smallest error margins. Because of this, and the high abundance of foraminifera in the high marsh, foraminifera-based sea level studies have typically focused on the agglutinated foraminiferal species that are vertically restricted to the higher elevations. In this upper tidal zone, common species such *as Jadammina macrescens* and *Trochamina Inflata* are widely used to delimit subzones. More restricted assemblages are sometimes identifiable and allow for finer subdivisions. However, when identifying finer subdivisions, spatial variability emerges between sites. This variability persists after normalizing the tidal ranges of different sites and is suggested to originate from other site-specific environmental influences (Edwards and Wright, 2015).

The early work on vertical assemblage zones is largely based on visual assessment of the data, describing vertical assemblage zones based on their dominant taxa and delimiting their elevational signal by matching with modern analogs (Vertical distribution patterns of present-day foraminifera), whereas more recent work tends to incorporate various statistical methods to discriminate between assemblages. Commonly used techniques include cluster analysis that seek to group samples together into "natural groups" based on their degree of similarity, and detrended correspondence analysis (DCA) that distributes samples along a primary with the most dissimilar at each end forming a theoretical environmental gradient. In DCA, the process is repeated with an uncorrelated secondary axis to maximize dissimilarity. When using these two techniques, only assemblages recognized by both should be used in determining assemblage zones (Edwards and Wright, 2015).

In recent literature, Edwards and Wright (2015) identify two main principles of foraminifera-based approaches to sea level research (table 2.1). The first principle is that the vertical zonation of certain taxa needs to correlate with elevation within the tidal zone. This must be quantifiable and time-invariant. The second principle is that the foraminifera contained within the sediment are autochthonous and that the assemblages are unchanged since their incorporation into the sediment. In essence, this means that meandering rivers, streams, anthropogenic adjustments, bioturbation and other influences can disturb the foraminiferal record, distorting their elevational relationships to local sea level. Where these principles are considered to be *acceptably* upheld (by the researcher(s)), species assemblages can be used to infer sample height above mean tide level in accordance with the principle of uniformitarianism (Edwards and Wright, 2015).

Table 2.1 Principles for using formainifera-based approaches in sea level research from Edwards and Wright (2015). The positive and negative column states what should positively and negatively influence the decision to use this approach.

Principle	Positive	Negative
1.1	There is a significant correlation between vertical zonation and elevation within the tidal range.	There is no correlation.
1.2	Local taxa vertical zonation does not change (meaningfully) within the time period.	Vertical zonation has changed (meaningfully) within the time period.
2	Foraminifera are autochthonous and remain undisturbed.	Foraminifera are transported and deposited into the sediment from somewhere else, and/or the sediment is disturbed between deposition and extraction

Foraminifera-based approaches to reconstructing past sea level change have some inherent complicating factors. Firstly, spatial variability in species assemblages, particularly in the high marsh, can show significant variability between sites both regionally and globally (Edwards and Wright, 2015). Secondly, the environmental gradient across the intertidal zone (i.e. elevation) encompasses a range of factors such as inundation frequency, salinity, clay content, percent organic matter and pH. Only if the underlying factors maintain a stable relationship with tidal range over time, can preserved foraminiferal assemblages be used to reconstruct past changes in RSL (Edwards and Wright, 2015).That being said, foraminifera-based methods to reconstruct paleo sea level seek to reduce the complexity and explain the relationship between changes in foraminifera assemblages (observed pattern) and the RSL(target variable). The goal is ultimately to extract an elevational signal from the dataset. As long as the elevational relationship to RSL from the data is detectable above the noise introduced from other factors, sea level reconstruction is possible (Edwards and Wright, 2015).

Thirdly, some foraminifera species are observed to be infaunal, living up to several decimeters below the sediment surface. This means that individuals of different age and environment might exist together at the same core depth (or depth below the marsh surface) and therefore be lumped into the same species assemblage. Introduction of infaunal species might distort, or even overprint, the epifaunal (living at the surface) assemblage. However, infaunal foraminifera are rarely found in large numbers, and are often restricted to the top centimeter of sediments (Alve and murray, 2001; Edwards and Wright, 2015).

Fourthly, sediment mixing might remove *in situ* individuals and introduce allochthonous components to species assemblages, but this is rarely a problem in cohesive sediments in the low energy, sheltered environments that are typical of salt marshes (Edwards and Wright, 2015).

Finally, the destruction of tests can remove the foraminiferal record altogether, and preferential destruction of tests can introduce a mismatch between preserved (fossil) and modern analogs (Edwards and Wright, 2015). Calcareous foraminifera are most prone to test destruction by dissolution of Ca in low pH conditions associated with salt marsh sediments (Concheyro et al., 2014). Destruction of agglutinated foraminifera tests are attributed to bacterial activity affecting the test itself or the organic cement holding the grains together. Even though preferential destruction of, for instance, calcareous tests, complicate comparisons to modern analogs, assemblages might still retain valuable environmental information (Edwards and Wright, 2015).

2.3.7.2 Foraminiferal Species

In 1999 Alve and Murray conducted a detailed ecological investigation of living, shallow water foraminifera species along the Skagerakk - Kattegatt coast, including marsh assemblages. This serves as a guideline for what species to expect in salt marsh sediments from southern Norway.

Twenty-five different species of foraminifera were identified in this region and were divided into six categories based on their preferred environments (Alve and Murray, 1999). Of these, six species from the three first categories are of interest for this thesis: "(1) species associated only with marsh plants, (2) species basically, but not entirely, associated with marsh plants, (3) species basically, but not entirely, restricted to non-marsh areas." (Alve and Murray, 1999; p. 171)

Category one comprises two agglutinated species. The first, *Balticammina pseudomacrescens*, was found clinging to algal sheets in Hunnebotn (a salt marsh in eastern Oslo fjord). The species is also associated with rotting leaf litter in the higher parts of *Phragmites* marshes (Alve and Murray, 1999). Since *B. pseudomacrescens* was observed to increase in relative abundance towards the more elevated areas of Hunnebotn, Alve and Murray (1999) argue that this species may define the uppermost limit of influence of marine water.

The second agglutinated species associated with marsh plants is *Tiphotrocha comprimata* (original name: *Throchammina Comprimata*; Cushman and Brönnimann, 1948), and was observed by Alve and Murray (1999) in three locations in the Oslo fjord, also observed clinging to filaments of algal sheets. However, they did not specify any tendency towards a specific height within the tidal range. Gehrels (1994) found peak abundances of *T. comprimata* above mean high water in Maine, USA. However, observations from northeastern North American marshes do not necessarily extrapolate well to the microtidal marshes in southern Norway.

Category two comprises three agglutinated species: The first, *Trochammina inflata*, was observed to be abundant in sediments associated with marsh plants in Bunnefjord (inner Oslo fjord) and Kildehuse (western Zealand, Denmark), but not attached to plant fragments. Rather, *T. inflata* is commonly found to live within the sediment without a symbiotic relationship with algae or algal chloroplasts (Alve and Murray, 1999). *Trochammina inflata* is broadly considered indicative of the upper quarter of the tidal range (Edwards and Wright, 2015).

The second, *J. macrescens*, was observed at 11 sites along the Skagerakk - Kattegatt coast. Like B. pseudomacrescens, it was found attached to filaments in fresh algal sheets. However, its peak abundances were observed on decaying leaf fragments of *Carex Acuta* (acute sedge / kvass-starr). Alve and Murray (1999) also noted that *J. macrescens* seems to dominate the landward zones of salt marshes. Like *T. inflata*, *J. macrescens* is considered indicative of the upper quarter of the tidal range (Edwards and Wright, 2015).

Jadammina macrescens and *B. pseudomacrescens are* morphologically similar, making them difficult to differentiate. Regardless of their close resemblance, they exhibit different distributions in modern salt marsh assemblages as *B. pseudomacrescens* is less tolerant towards salinity than *J. macrescens*. A differentiation between these two species can be used to differentiate facies from the highest tidal elevations (Edwards and Wright, 2015).

The third species, *Haplophragmoides wilberti*, was found by Alve and Murray (1999) at 7 sites. However, they did not specify any tendency towards a specific height within the tidal range. Other studies show that *H. wilberti* usually occupies high marsh environments. For example, Kemp et al. (2009) used *H. wilberti* as indicative of high marsh facies in North Carolina, USA. Likewise, Gehrels et al. (2008) used this species as indicative of near extreme high water in New Zealand. Therefore, it is reasonable to assume that this species, if present in southern Norway, reflects a high marsh environment.

Category three comprises four agglutinated and two calcareous species. From these, the agglutinated species *Miliammina fusca* is of most interest to this thesis. *M. fusca* tolerates a wide range of salinities (<1 – 35‰), is reported to live at or very near the sediment surface, and on some occasions to cling to filamentous algae (Alve and Murray, 1999). Alve and Murray (1999) observed living *M. fusca* at 25 sites, noting that it seems to live in all environments, but tends to dominate the seaward zone of salt marshes. *Miliammina fusca* in combination with calcareous foraminifera is a commonly used indicator of transitional zones in the lowest marsh fringe (Edwards and Wright, 2015).

2.3.7.3 Testate Amoeba

Foraminifera based methods of RSL reconstruction commonly encounter testate amoeba in the counted samples. These are small, single celled organisms that form chitin tests (sometimes with embedded sand grains). They are found in a wide range of terrestrial environments, particularly wet sediments, but also in brackish environments like salt marshes. Vertical zonation of testates can be used in a similar fashion to foraminifera in RSL studies (e.g. Barnett et al., 2017). In salt marsh environments, testate amoeba are restricted to parts of the intertidal and supratidal zone, and are therefore indicative of brackish or freshwater conditions. Compared to foraminifera, testate amoeba are generally more susceptible to physical and chemical destruction. The tests of most species do not resist destruction during reworking, meaning that they can be assumed as autochthonous of the sediment they are found in (Charman, 2015).

2.4 Study Area

2.4.1 Sea Level History of Southernmost Norway

Contrary to most of Norway, the southernmost region (Here with reference to the municipalities Lista, Farsund, Lindesnes) does not have a marine limit (highest postglacial shoreline) resulting from inundation by the sea that immediately followed deglaciation approximately 14,000 years ago (Romundset et al., 2015; Fjeldskaar & Amantov, 2018). Rather, marine limit here is represented by large beach ridges that was deposited on the Lista peninsula during the peak Tapes transgression, a period of rising RSL that ceased at 5 m a.s.l. in ~7000 BP in the early-mid Holocene (Romundset et al., 2015). Early Holocene sea level prior to the Tapes transgression was lower than present-day MSL. Direct evidence of a submerged early Holocene shoreline was first established in 1909 when submerged peat was found below the present-day shoreline (Holmboe 1909; as stated in Romundset et al., 2015).

The latest RSL curve for southernmost Norway from Romundset et al. (2015) is based on well dated sedimentary records of inundations and isolations of basins with traceable bedrock sills, resulting in several solid sea level index points well-constrained by radiocarbon dating (the location of these basins are shown in figure 2.3). Isolation basins (with a traceable bedrock sill) are among the most reliable indicators of RSL change, and generally preferable for reconstructing past RSL change, particularly in with respect to elevational accuracy and sea-level tendency (Romundset et al., 2015).

Therefore, the curve presented by Romundset et al. (2015) is preferable to the older interpretations (discussed below) of the local RSL history.

The RSL curve for southern Norway established by Romundset et al., (2015; figure 2.5) used *in situ* submarine peat, which indicates an early Holocene RSL of 3.7 – 4.2 m below msl. The first record of the Tapes transgression is from basin 4 (Basin 4; Romundset et al. 2015) ca. 8600 cal. a BP. Submergence was rapid at first, with an average rate of ~7 mm/a from 8600 a BP until 8200 a BP, and then slowed to about ~1 mm/a until peaking by approximately ~7000 cal. a BP, reaching an elevation of ~5 m above MSL. Land emergence following peak transgression was slow at first with an average rate of about ~0.4 mm/a until 3900 a BP. In the next 300 years, it accelerated to a rate of 2.6 mm/a. After this short period of relatively rapid emergence, rates gradually slowed, reaching an average rate for the past 2000 years of ~0.2 mm/a (Romundset et al., 2015). Tide gauge measurements at Tregde, which began in AD 1927, show a mean rate of RSL rise of 0.4 mm/a between 1927 and 2010, and 1.4 mm/a between 1980 and 2010 (calculated for differential uplift (GIA); Romundset et al., 2015). This period of measured RSL rise is not reflected in the RSL curve.

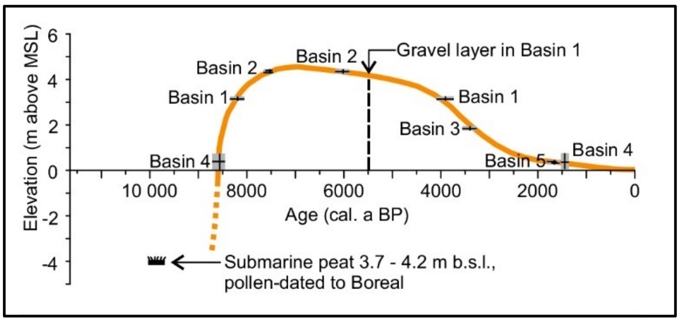

Figure 2.5 This figure from Romundset et al (2015) plots sea level index points derived from multiple isolation basins in the municipalities in Lista and Farsund (specific locations shown in section2.1.3; figure 2.3), and the resulting curve. Note how the most recent part of this sea level cure does not reflect the ongoing transgression recorded by the tide gauge at Tregde.

Older studies of RSL change in southern Norway, from deglaciation to present day, have been published since the 1900s (e.g. Holmboe 1909; Sollesnes & Fægri 1951; Andersen, 1960; Prøsch-Danielsen 1997; Ryen et al., 2009; as stated in Romundset et al., 2015). Different interpretations of sea level indicators have resulted in conflicting sea level curves for the area (figure 2.6). In particular, some reconstructed sea-level histories of southwestern Norway have hypothesised that multiple sea-level transgressions occurred in the Holocene (e.g. Andersen, 1960, Ryen et al., 2009; as stated in Romundset et al., 2015). Romundset et al. (2015) disproved this hypothesis with their isolation basin study in 2015. The discrepancy between the older studies and the Romundset et al. (2015) study are discussed below.

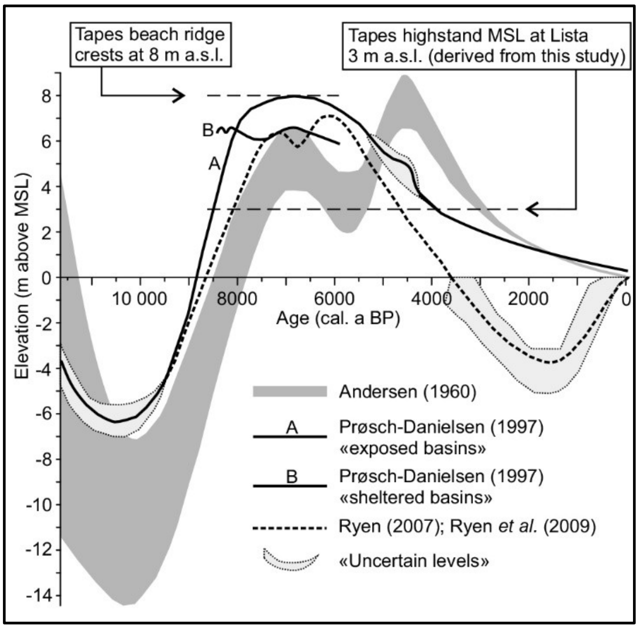

Figure 2.6 Sea level curves published prior to the 2015 publication of the Romundset et al. (2015) curve (Figure from Romundset et al., 2015). Despite the divergences and multiple transgressions, all of the RSL curves follow a similar pattern.

The first record interpreted as multiple transgressions came from two lake records from Bølmo (municipality in Hordaland county) and Jæren (region in Rogaland county) where two marine facies were identified (Fægri 1940, 1944; as stated in Romundset et al., 2015). The first of these marine facies was later identified as originating from inundation by the Storegga tsunami, which occurred before the Tapes transgression. Most of the later sediment core studies in the area focused on basins without traceable bedrock sills; in other words, these basins are depressions in unconsolidated deposits that have formed present day lakes and marshy land. Discontinuous and often short sedimentary records from these with both marine and lacustrine diatom assemblages have been interpreted to represent multiple transgressions (e.g. Høeg 1995; Prøsch-Danielsen 1997, 2006; as stated in Romundset et al., 2015). No undisturbed record of multiple transgressions has been found in a basin with a traceable bedrock sill to date in southern Norway (Romundset et al. 2015). Alternating layers of terrestrial peat and beach gravel have sometimes been interpreted as stratigraphic evidence of sea level fluctuations. However, strong storm events can build beach ridges over inland peat deposits without being related to longer-term RSL change. Ryen et al. (2009) suggested that the current transgression (as indicated by the tide gauge at Tregde) started at ~5 m below present-day sea level about 1500 years ago. This hypothesis was based on ground penetrating radar showing a stratigraphic feature interpreted as a drowned beach ridge, but was later rejected by the Romundset et al. (2015) isolation basin study.

2.4.2 Tranevåg Saltmarsh

The Tranevåg saltmarsh system (figure 2.7) is located in the back of a protected marine basin connected to the sea through a narrow inlet passage. The initial passage point is about ~3 - 3.5 m wide at its narrowest, with a sandy bottom approximately 1 m below MSL. This passage point is the basin threshold, however, the true depth of the threshold (i.e. depth to bedrock) is not known. Moreover, it is believed that this passage point has been expanded at some point prior to 1966 (from the oldest aerial photography of the basin), likely to allow passage for small boats. Moving landward, the inlet passage widens to ~80 m, then narrows to ~40 m, visibly shallowing.

The back of the basin is very well-sheltered from the open sea and is ideally situated for salt marsh formation. The outer inlet itself is separated from the open sea by islands and skerries (figure 1.1), although the main sheltering effect comes from the basin morphology itself. As the tidal wave approaches the basin, it must first move through the very narrow outer passage and the wider inner passage. In addition to attenuating direct wave energy and sheltering the inner basin, the multiple islands and skerries also cause considerable bed friction that further reduces tidal energy.

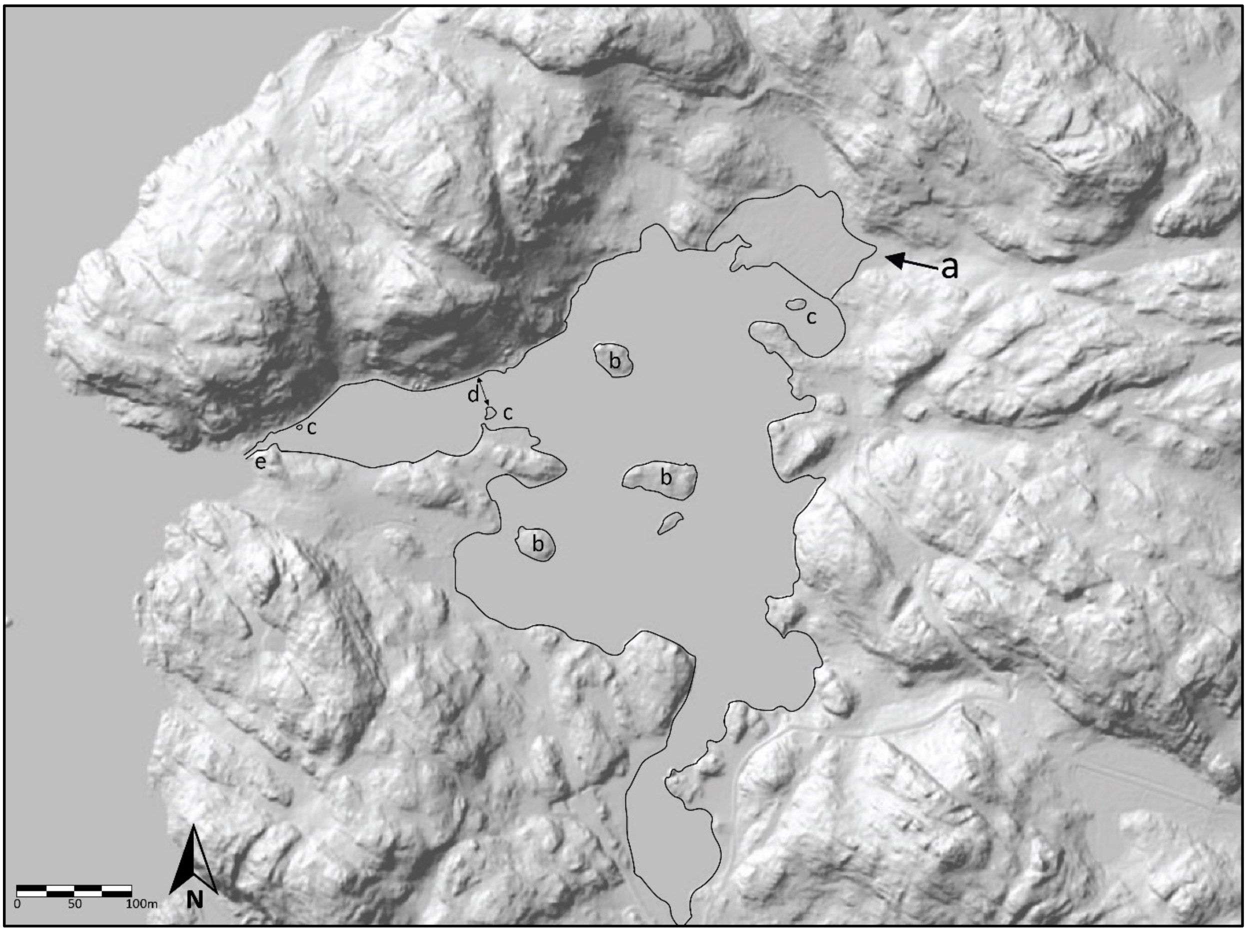

Figure 2.7 Hillshade of the Tranevåg basin with a) marsh outlined. The basin has multiple b) islands and some c) skerries. The e) initial inlet is approximately 3.5 m wide and the d) second narrowing is approximately 40 m wide. The hillshade is from InnlandsGIS.no (Kartverket, 2019a).

The salt marsh surface (figure 2.8, 2.9) has a characteristic undulating topography with multiple ponds and raised platforms. Moving inland, the surface becomes smoother in the reedswamp zone. Further inland still, the sedge fen zone has a hummocky topography. The reed swamp and saltmarsh surfaces are dissected by multiple drainage channels of anthropogenic origin, as well as some linear features interpreted as possible animal trails. The woodland area at the back of the marsh system is situated on exposed/partly exposed bedrock. Zonation of vegetation is apparent in the infrared aerial photograph (figure 2.9).

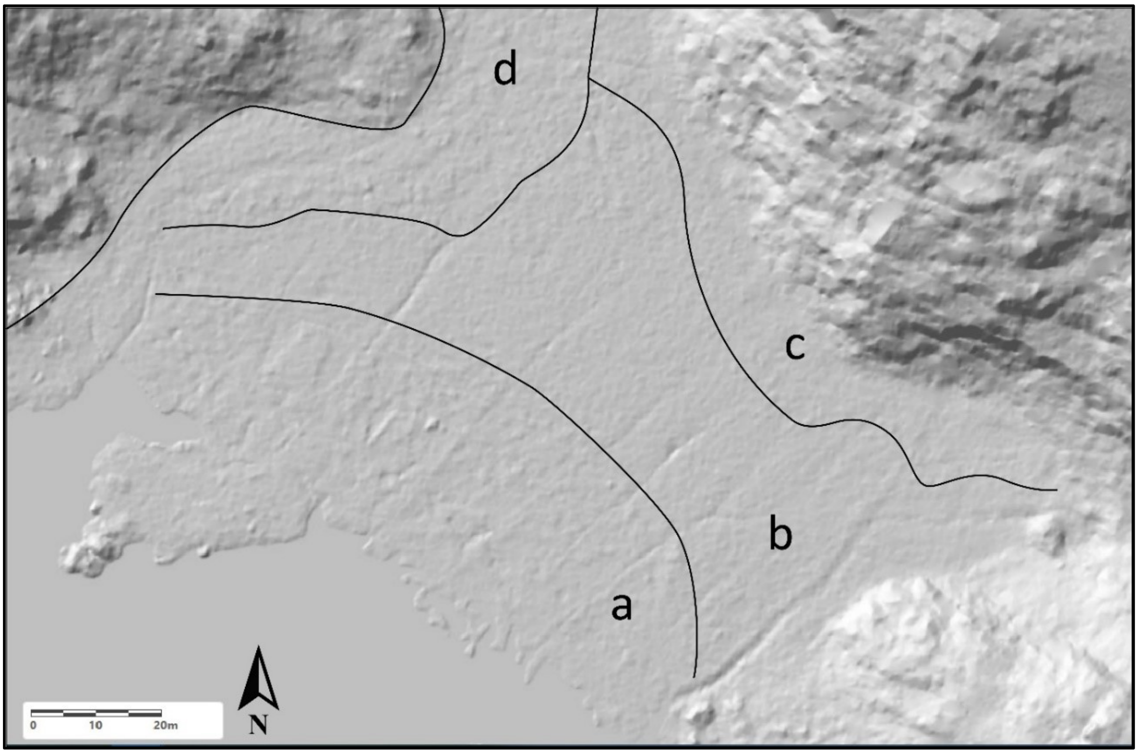

Figure 2.8 Hillshade of the surface of the salt marsh at Tranevåg from a 0.25m resolution DTM published online by the Norwegian mapping authority. a) Vegetated salt marsh platform. b) Reedswamp. c) Woodland. d) sedge fen. Notice the undulating topography of the salt marsh surface, relative smoothness of the reed swamp zone and hummocky sedge fen. The hillshade is from InnlandsGIS.no (Kartverket, 2019a)

The elevational range is difficult to establish accurately. The DEM raster available for this thesis work has a 1 m resolution and online tools are based on elevation curve interpolation. Both of these are simply not adequate to capture the subtleties of the marsh surface. However, it is reasonable to assume that elevational zonation follows the general pattern of the local vertical RSL datums (modelled based on proximal measurements, presented below relative to the NN2000 vertical datum.), published online by the Norwegian Mapping Authority (Kartverket, 2018). Mean sea level between 1996 and 2014 is -10 cm and mean high tide is -3 cm. From the vertical datums it is likely that the intertidal zone spans from the lower tidal flats that begin at approximately -20 cm, up to the upper boundary of the higher tidal flats at +8 cm (highest astronomical tide), and that the supratidal zone reaches approximately +57 cm (annual highwater). Above +57 cm, the environment can be considered terrestrial.

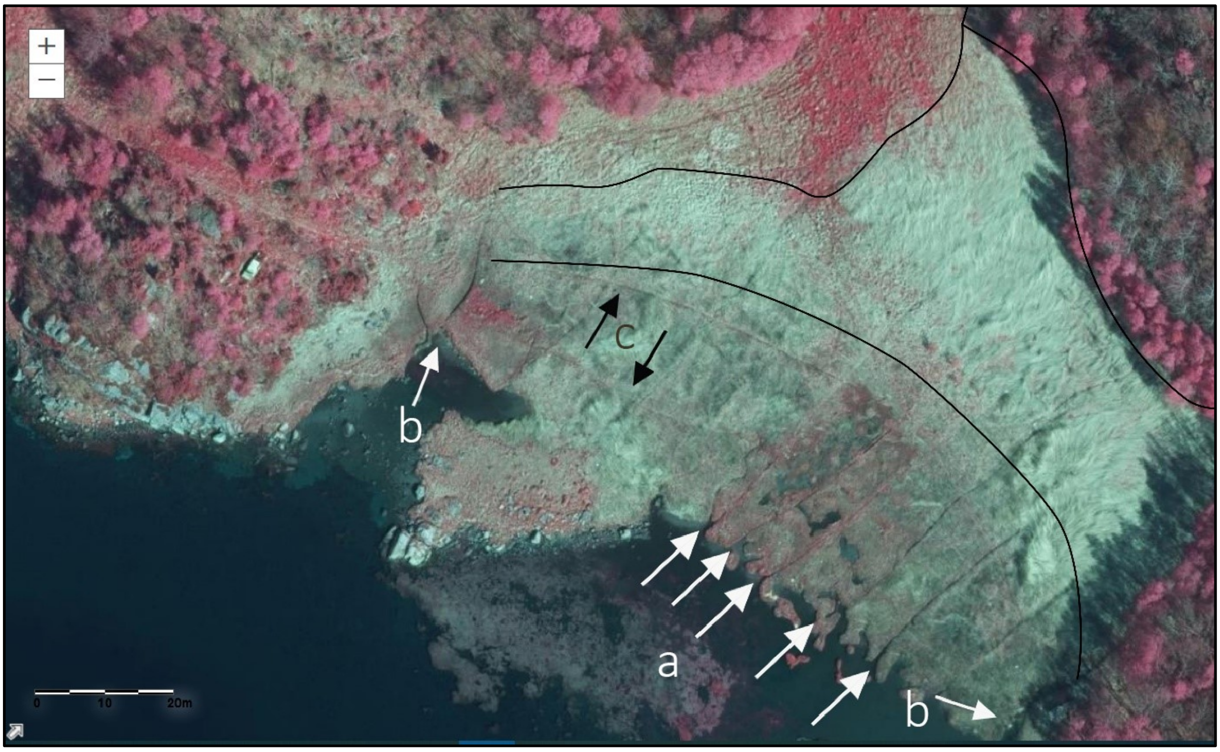

Figure 2.9 Infrared aerial photograph from the 27th of Mars, 2014. A) Anthropogenic drainage channels of unknown age. B) Natural creeks. C) Animal trails or anthropogenic channels excavated by people at an unknown time in the past. The colour changes in the infrared spectrum also provide an indication of the vegetation zonation. The upper red area corresponds well with the sedge fen zone. The teal area represents the inland reedswamp. Note the abrupt, irregular boundary between salt marsh and mudflat (underwater), and the algae floating at the water surface. Photograph is from NorgeIBilder.no (Kartverket, 2019).

2.4.3 Basin Tidal Dynamics

The inlet connecting the basin to the open sea might cause *flood-depression*, a lowering of the upstream high-water levels. Additionally, the narrow inlet passage of this basin causes a *flood-basin effect*. That is, a delay in filling and draining of the basin in conjunction with the outer tidal level. In effect, the morphology of the inlet decreases the rate at which water can enter the basin, causing a delay, and therefore difference, in tidal levels outside and inside of the basin. When the outside water level reaches high-water and subsequently starts to decrease again, the water level inside the basin is still at a lower level and increasing. The basin water level will only start to decrease when it reaches the same height as the outer sea level. This causes a lowering of the basin high water level, the magnitude of which is determined by the rate at which water can enter the basin. This effect also works in reverse, where low rates of draining can cause a higher low-water level than the outer water level (Vis et al., 2015).

The magnitude of these effects in the basin at Tranevåg is unknown as they were not measured. The small size of the basin likely makes these effects negligible during regular tides. However, during two days of field work in September 2018, as the storm

"Knud" (Holm-Nilsen & Wergeland, 2018) caused destructive wave energy along the coast, wave energy was extremely reduced within the basin. Water levels peaked at 55 cm above MSL (Kartverket, 2018) with only wind generated ripples present at the water surface at the marsh-basin interface. The observed calmness of the water during such a large storm event demonstrates that even storm surge tides do not reach the marsh system with any considerable energy. As the flood-depression effect is closely tied to bed friction, and flood-basin effect is tied to narrow passage-points, it can be argued that these have some impact in this location, especially during short-lived extreme sea level events such as storm surges.

2.4.4 Source of Terrigenous Sediment

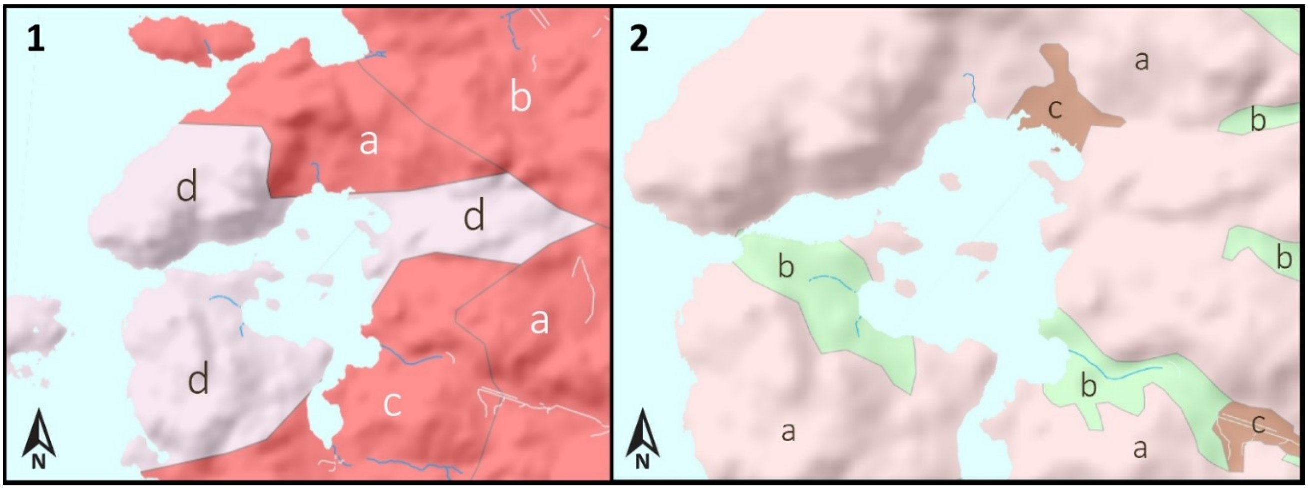

Figure 2.10 1) Geological bedrock map of the study area from the Norwegian Geological survey's online map service. 1a = Red alkali feldspar granite; 2b = Hornblende granite, sporadic biotite; 2c = Biotite granite; 1d = Granitic gneiss, enriched in quartz and feldspar. 2) Map of Soils from the Norwegian Geological surveys online map service. 2a = exposed bedrock (>50% exposed); 2b = till; 2c = marshy soil and/or peat (>0.5m depth).

Due to the low tidal energy, even during storms, it is likely that surface wash is an important process delivering minerogenic (and organic) sediments to the surface of the saltmarsh. The watershed draining through the saltmarsh at Tranevåg is very small (~0.115 sq. km) and there are no rivers connecting the system to hinterland areas except possibly during floods. As such, terrestrially deposited material is expected to originate from the exposed bedrock at the back of the marsh.

Based on the geological bedrock and soil maps (figure 2.10) available at the Norwegian Geological Survey's (NGU) online map service, the source of the weathered material is expected to be red alkaline feldspar granite, Hornblende granite and quartz- and feldspar enriched granitic gneiss. Some contribution from glacial till is also possible, but likely limited to the very east area of the marsh.

2.4.5 Anthropogenic Activity

Through their online map service, the Norwegian mapping authority (Kartverket) has made available multiple aerial photographs of the study area. The oldest photograph is from 1966 (figure 2.11). There is a 36-year gap before the second oldest photograph (2002). After 2002, there are aerial photographs from, 2004, 2009 (figure 2.12), 2014 and 2018. The aerial photographs present a way of assessing the land use, and therefore some of the anthropogenic impacts on the marsh system.

Figure 2.11 Aerial photograph from the 19th of May, 1966. The channels are present and harvesting of the upper reedswamp and sedge fen is evident. Photograph is from NorgeIBilder.no (Kartverket, 2019b)

The upland area of Tranevåg saltmarsh, including parts of the reedswamp, were actively harvested, likely for animal feed or roof thatching (*Phragmites Australis* / common reed) (figure 2.11, 2.12). The anthropogenic channels that dissect the marsh were dug prior to 1966 (figure 2.11). These are interpreted as a means of draining the upper areas of the reedswamp. Active harvesting likely continued until ~2009, the last photograph showing visible indications of harvesting (figure 2.12). However, it does not look like the area was tilled. There is also a possibility that the area was used for seasonal grazing. Firstly, the hummocky sedge fen zone shares morphological similarities to fields used for grazing (i.e. a hummocky morphology due to preferential grazing and cattle footprints). Secondly, lines crossing the marsh perpendicular to the dug channels could result from livestock trailing the marsh (i.e. animal trails). However, these could also be dug out channels. Interestingly, these were not present in 1966.

Figure 2.12 Aerial photograph from the 1st of May, 2009. a) Recent harvesting visible in the uppermost area outside of the wetlands. b) Traces of harvest still visible in the sedge fen and upper reedswamp area. Photograph is from NorgeIBilder.no (Kartverket, 2019c)

Chapter 3 Methods

3.1 Field work

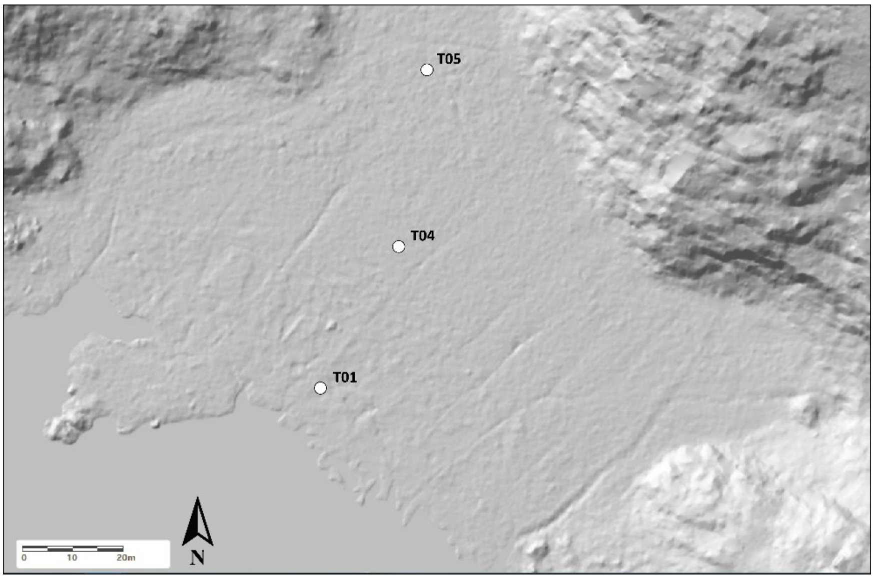

Figure 3.1 Hillshade of Tranevåg saltmarsh showing the three coring sites. The hillshade is from InnlandsGIS.no (Kartverket, 2019a)

Field work was conducted with partners, Anders Romundset, Thomas Lakeman and Lina Gislefoss, from the Norwegian Geological Survey (NGU) between 17.09.2018 and 22.09.2018. The salt marsh chosen for this thesis was visited and cored the 21.09.2018 and 22.09.2018. The cores presented in this thesis were extracted the 22.09.2018.

Coring locations (figure 3.1) in the salt marsh were chosen in the field, aiming to capture the surficial and subsurface sedimentary records from specific tide-related intervals in the marsh. These were chosen based on the vertical zonation of vegetation, assessed on site (see section 4.6). The first core (T01; $58° \ 03.635 \ \mathrm{N} \ \ 006° \ 56.775 \ \mathrm{E}$) was cored as far out onto the vegetated saltmarsh platform as could be reached by foot. At the time of coring (12:00) this area was submerged to a depth of 36 cm, giving an approximate elevation of +2 cm (NN2000), which is 5 cm above mean high tide.

The second coring location (T04; $58° \ 03.652 \ \mathrm{N} \ \ 006° \ 56.785 \ \mathrm{E}$) occurs approximately midway across the reedswamp zone, a few meters landwards into the *P. australis* subzone. At the time of coring (13:10) this area was submerged to a depth of 18.5 cm, giving an approximate elevation of +21.5 cm (NN2000), which is about midway between annual high water and mean high tide.

The third coring location (T05; 58° 03.671 N 006° 56.786 E) was at the boundary between the landward reedswamp zone dominated by *P. australis* and the sedge fen zone (picture in section 4.6; figure 4.11). At the time of coring (14:00) this was submerged about 1 cm, with an approximate elevation of +42 cm (NN2000), which is 15 cm below annual high water. This area was assumed to be inundated infrequently, only during storm surges.

3.1.1 Russian Coring

The coring equipment available for this thesis was a 1 m long, 10 cm wide, Russian-style corer (figure 3.1). A Russian corer is a hollow half cylinder made of steel. Through the middle of the corer there is a rotatable steel rod with a flat blade attached, sealing the hollow chamber. The bottom of the core has a conical shape for easier penetration through fine-grained sediments. At the top of the core, a handle or extension rod can be fastened.

Once coring locations were selected, the core was pushed down to the desired depth. To reach deeper than the top meter, extension rods of 1.5m are attached to the core. When at the desired depth, the core is rotated and extracted (figure 3.2, 3.3).

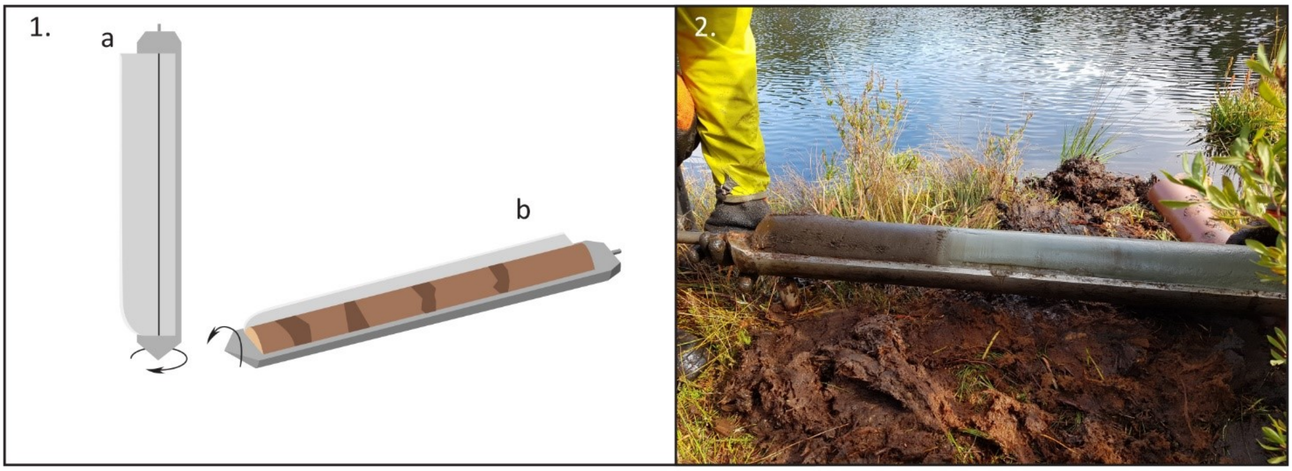

Figure 3.2 1.a) Russian corer before coring (arrow indicates direction of rotation to trap the sediment inside the core barrel). 1.b) Russian corer after extraction with the sample exposed (arrow indicates direction of rotation to open the core barrel). 2) Picture of Russian corer (from an isolation basin near Kristiansand) after extraction with the sample exposed.

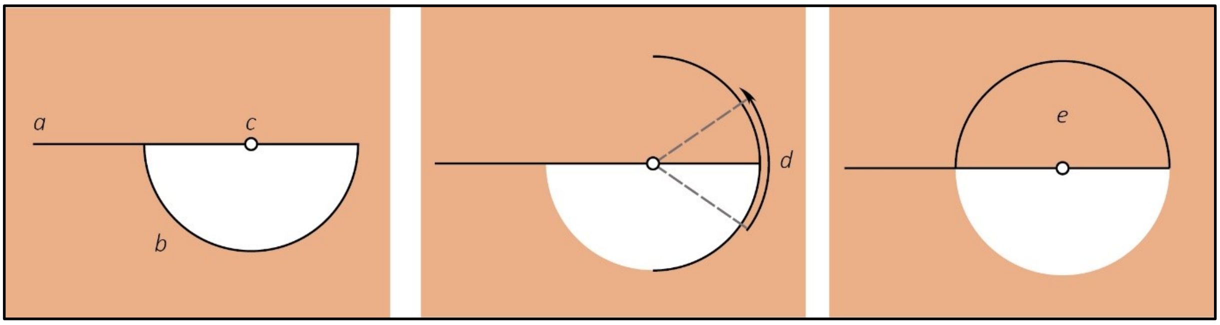

Figure 3.3 1) The core's initial position when inserted into the subsurface. a indicates the blade attached to c, a rotatable steel rod. b = chamber of the core. 2). The core is turned, rotating around the steel rod, fixed in place by the blade. d= direction of rotation. 3. The core's final position before extraction. e =trapped sediment in the chamber.

3.1.2 Sample Handling and Transport

After extraction, the cores were overlain by a thin plastic film and placed into a half pvc tube (ø110 mm), cut to the same length as the core (1 m). The tube ends were sealed with duct tape. If the core was less than 1 meter, the open space was filled with paper towels, separated from the core by the plastic film. Finally, the tube was labeled, wrapped in plastic film, put in a plastic bag and sealed with more duct tape. Notably, during this process, nearby insects were drawn to the core, and some were trapped during the wrapping process. Some of these were still alive when the cores were unwrapped in the lab. This might introduce noise in the form of modern carbon in the core. After wrapping, the cores were stored horizontally in a van and transported to back to the NGU lab in Trondheim, where they were stored horizontally in a fridge at 4° C, approximately 32 hours after extraction.

3.2 Lab work

3.2.1 Core Logging

All cores were logged by hand on a standard core-log form. During extraction the core surface becomes irregular and, during transport and storage, oxidation and drying can cause the surface to darken in colour. Therefore, to properly log the cores, the distorted surface of the cores scraped, taking care not to move sediment up or down the core. This cleaning process also makes the stratigraphy more visible. Characteristics that were visible by eye, such as colour changes, deformations and some lithological changes were logged.

3.2.2 Subsampling for Foraminifera

Samples for foraminiferal analysis were extracted at a 5 cm interval and wet sieved at 125µm, 63 µm and 45 µm, keeping the 125-63 µm and 63-45 µm fractions, totalling 40 samples from T01 (0-2m), 20 samples from T04 (0-1m) and 19 samples from T05 (0-1m). Samples were extracted as centrally in the core as possible to avoid any contamination at the boundaries where some disturbance to the stratigraphy may have occurred during the coring process. The samples were extracted using a modified syringe (with the bottom cut off) and, if necessary, a razor blade was used to cut any roots that hindered the syringe from penetrating the sediment. All samples consisted of 10 ml of sediment and were mixed in a solution of water and ethanol to keep them wet and inhibit growth of fungi, bacteria and other biological activity. Between sampling and analysis, samples were kept refrigerated at 4°C. Samples taken from the upper 15 cm of the core were additionally treated with the Rose Bengal stain. This stain allows the distinction of foraminifera that were still alive at the time of treatment (and by extension, collection) as the cytoplasm of the cell absorbs some of the stain and acquires a pink colour.

Foraminiferal assemblages in T01 were believed to most strongly reflect recent RLS change. The counting strategy was to broadly characterize sea level trends, narrowing down the horizon at which the sea level trend changes, by counting samples at a 20 cm interval, up core from 2m depth in T01. Following, the horizon where the sea level trend changes could be counted at a higher resolution. However, counting was discontinued after counting 9 samples.

3.2.3 Wet Splitting and Counting

Even though wet picking (as opposed to dry picking, where samples are first dried, then the foraminifera are picked out for identification and counting) is the preferred method for identifying saltmarsh foraminifera, it is a lengthy endeavour (Charrieau et al., 2018). To produce the number of counts of individual foraminifera sufficient to answer the research question within the timeframe of this thesis, the samples needed to be split into eighths using a wet splitter. This splitter was constructed using the design outlined in Charrieau et al. (2018; figure 3.4), consisting of 4 3d-printed pieces, a 1m clear pvc tube with a diameter of 110 mm, rubber stoppers, and a rubber drainage hose. The 3d-printed parts were printed by a fellow student, Lars-Arne Boge, at the Institute for Nanotechnology at NTNU, by a Ultimaker 2+ and 3DTouch 3d-printer using the printing materials Spot-HT for pieces in hard plastic and Spot-E for the soft plastic seal.

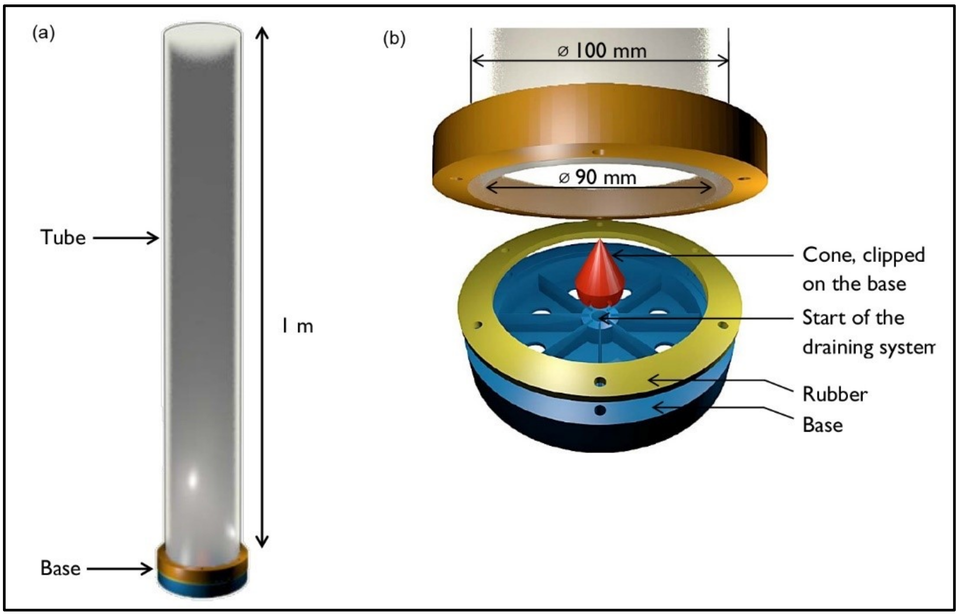

Figure 3.4 Illustration of the wet splitter from Charrieau et al. (2018) A) full view. B) Base detail. Figure adapted from Charrieau et al. (2018).

During initial testing, the splitter had some leaks between the upper ring and the plastic tube, and through the screw holes. The screw-leaks were sealed using glue designed for sealing rubber boots. The plastic tube leaks were more difficult to seal, however, inserting a plastic foil between the outer ring and the plastic tube worked well. I (the author) never managed to seal the leaks completely, however, after a few test runs the splitter had leaks thought to be minimal (<0.1 liters over 24 hours).

Six samples were split before the wet splitter was discarded. The first three splits were relatively successful. Nevertheless, some particles stuck to the plastic tube itself rather than settle into the chambers. Partial draining (~1/4 of the water volume) of the splitter seemed to loosen these from the tube. This is problematic as it can possibly introduce partial settling, however, no alternative was apparent. The leaks, although minimal, can introduce partial settling and sample loss. From the fourth split, the leaks began to worsen, and the splitter was discarded. Only the first three split samples (1-2cm, 40-41cm and 90-91cm) were kept for counting. The main reason for the failure of the splitter is believed to be the fragility of the 3d-printed parts.

Samples were always kept wet to prevent the destruction of the fragile agglutinated foraminifera. Counts were conducted using a Nikon SMZ1270i stereo microscope following the methods outlined by Edwards and Wright (2015). The eighths were counted one at a time (selected at random) until reaching a total foraminiferal count of at least 300 individuals (excluding organic linings) per sub sample in line with common practice for acquiring robust data (Edwards ad Wright, 2015). After the wet splitter was damaged and remaining samples could not be split, full samples were counted. If samples had an excess of particles smaller than 63microns and/or tended to excessively coalesce during counting, these were treated with *Calgon* ($Na_6O_{18}P_6$) to loosen particles from each other and wet sieved again.

3.2.3.1 3.2.4.1 Species identification

Species were identified based on scanning electron microscope (SEM) images published in Hayward & Brook., (1994), Riveiros et al, (2007a, 2007b), Camacho et al., (2015) and Edwards and Wright (2015; figure 3.5), of the foraminifera species in Alve and Murray (1999), and descriptions presented in Edwards and Wright (2015).

Figure 3.5 Example of images from scanning electron microscope (SEM) that were used for species identification. In this figure, the SEM images are of *Jadammina macrescens* (4a-f), and *Miliammina fusca* (5a-g). Figure adapted from Edwards and Wright (2015). Scale bars: 100 µm.

3.2.4 Radiocarbon Dating

Four samples of organic matter were picked from T01, two from T04 and one from T05 (Table 4.1) and sent to the Poznan Radiocarbon Laboratory in Poznan, Poland for dating. Where possible, seeds and leaves from the same species were selected for dating as wood is more likely to be transported onto the marsh surface, rather than *in situ*. Machine ages were calibrated using Calib version 7.0.4 (Stuvier et al., 2019).

3.2.5 Core Scans

The cores were subjected to three scans at NGU, in Trondheim: x-ray, magnetic susceptibility (every 5mm) and very high resolution (approximately 520 pixels pr. inch) RGB photography.

3.2.6 X-ray Fluorescence Sub-Sampling

Samples for XRF analysis were taken at 1 cm resolution for the top meter of the T01 and T04 cores. One cm^3 chunks were cut out using a razor blade and pushed into a teaspoon (5 ml) and excess sediments were scraped off to keep samples approximately similar in volume. These were then air dried for >48 hours and packed in plastic bags. The samples were then sent the Geological Survey of Nova Scotia, Canada, and scanned using a X-5000 Olympus portable XRF spectroscopy instrument.

The XRF data from the cores was analysed following the principles outlined in section 2.3.1.1, 2.3.1.2, 2.3.5 and 2.3.6. The choice of which elemental profiles to include in the analysis was based on based on the usage of specific elemental profiles as proxies as described by Rothwell and Croudance (2015) in their XRF-handbook and from additional literature reviews. Correlations between elements were checked using the statistical software IBM SPSS Statistics 25 and elements that showed statistically significant correlations or anticorrelations were investigated.

3.2.7 Vegetation Zonation

To aid the interpretation of the sediment cores the idealized coastal vegetation zonation for northwestern Europe (Waller, 2015; Fig. 2.4) was compared to vegetation zones at the study site (see section 4.6). The zones were identified based on field observations and images taken in the field. The online map service of the Norwegian Biodiversity Information centre (Artsdatabanken, 2019) was used to establish known plant species that grow at proximal sites (between Lindesnes and Lista). These species were assumed to be the most likely species to inhabit these vegetation zones.

Chapter 4 Results

4.1 Radiocarbon Dates

Presented below in table 4.1 are the radiocarbon dated samples of organic matter extracted from the Tranevåg sediment cores T01, T04, and T05. Those samples that were deemed spuriously young or old based on their position in the cores and with respect to other radiocarbon dates and Pb time marker data (see section 5.1) were not included in our analysis and are marked red in the tables. Ages included in our age model are marked green. Radiocarbon dates were calibrated using the software *CALIB* version 7.0.4 (Stuiver et al., 2019). The calibrated dates are presented in years BP, using 2019 AD as the 0-age datum. Later in the thesis, the calibrated dates are presented in text as the midpoint of the age ranges for readability.

Table 4.1 Radiocarbon dates for cores T01, T04 and T05. Green ages are accepted, and red ages are discarded. Calibrated age is the midpoint of the 2-sigma range

Core	Depth in cm	Weight	Material	C-14 age	Calibrated age
T01	35-36	50 mg	Bark	565 ± 30 BP	528 – 611 BP
T01	48-49	850 mg	Pine cone	1730 ± 30 BP	1564 – 1707 BP
T01	70.5	17.8 mg	Seeds from *Ruppia* and other species	475 ± 30 BP	497 – 541 BP
T01	82	17.2	Wood	925 ± 30 BP	769 – 772 BP / 781 – 924 BP
T04	58.5 – 59.5	300 mg	Wood	2125 ± 30 BP	2028 – 2189 BP
T04	97 – 98	7.9 mg	Twig	2950 ± 30 BP	3001 – 3188 BP/ 3193 – 3204 BP
T05	94 - 95.5	26.1 mg	Bark	4230 ± 35 BP	4762 BP

4.2 Core Scans

4.2.1 High-Photographs and X-ray Imagery

Presented below are High resolution RGB photographs and X-ray images of cores T01 (0 – 1, 1.05 – 2.05 and 2 - 3 m; figure 4.1), T04 (0 – 1 m; figure 5.2) and T05 (0 – 1 m; figure 5.2). The top meter of sediments are separated into segments based the colour of the sediments, structures and textures in the x-rays and the visible organic matter. The following results and analysis of the cores are discussed within the context of these segments. High resolution RGB photographs and X-ray images of cores from T01 5-7m depth are included in appendix 3.

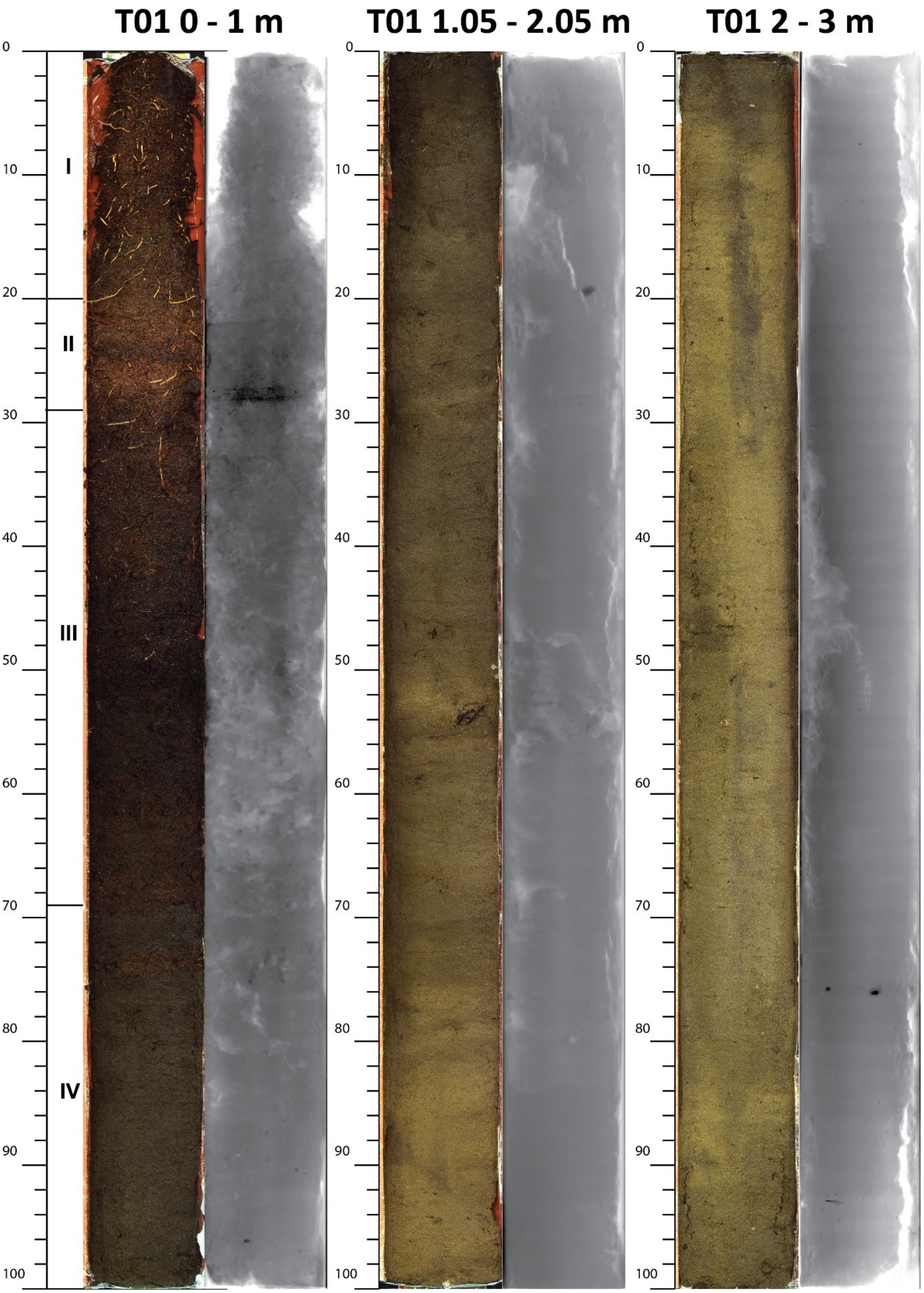

Figure 4.1 High resolution RGB photographs and X-ray images of T01 sections 0 – 1 m, 1.05 – 2.05 m and 2 – 3 m.

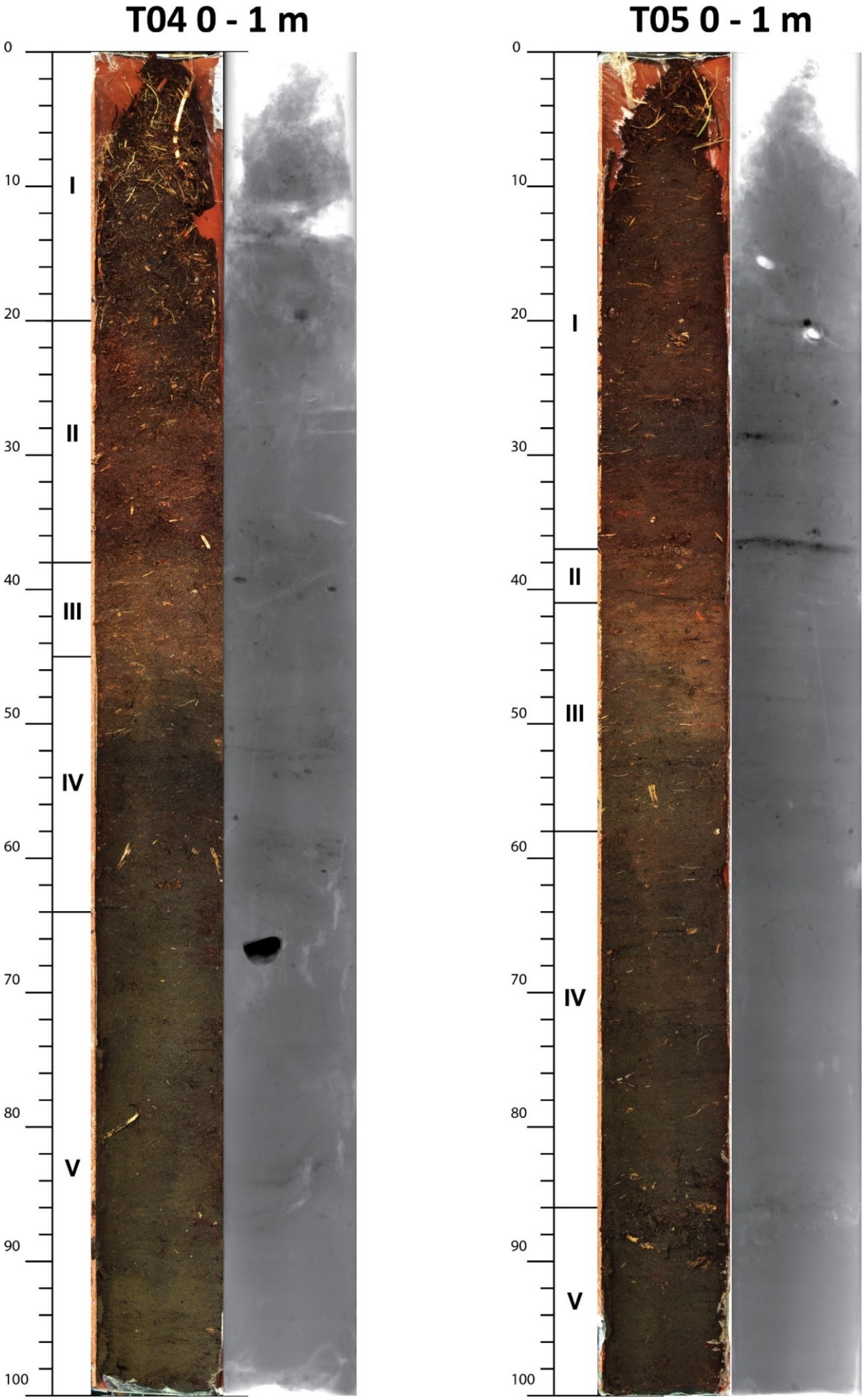
T04 0 - 1 m

T05 0 - 1 m

Figure 4.2 High resolution RGB photographs and X-ray images of T04 0 – 1m section.

4.2.2 4.2.2 Magnetic Susceptibility and XRF-Measurements

Magnetic susceptibility and XRF measurements are presented and discussed below in the subsections for each core. The magnetic susceptibility measurements from T01 cores between 5-7 m depth are included in appendix 3. The complete XRF measurements (spreadsheets) are included in appendix 2.

4.3 Core T01

4.3.1 Stratigraphy

At site T01 (figure 3.1), a 7 m sedimentary record was recovered from Tranevåg, however only the upper 1 m is analyzed in this thesis because this captures the most recent RSL history. A brief description of the sediments between 2-7 m is included below.

Sediments between 7 m and approximately 6.1 m are likely glacial lacustrine facies (Anders Romundset, personal communication, 2018), with roots appearing at ~6.3m. These basal sediments are overlain by peat from ~6.1 to a marine shelly contact followed by marine sediments at ~5.5m dated to approximately 9,500 years BP (Anders Romundset, personal communication, 2019). The two cores between 5-3m were interpreted as organic-rich marine silty clay in the field and discarded.

Between 2-3m in T01 (figure 4.1), sediments are uniform in colour (greyish amber) and texture, with no clear breaks, however, x-rays show ~1 cm thick, horizontally bedded, lighter (less dense) and darker (more dense) layers throughout the core. In T01 1-2m (figure 4.1), the horizontal bedding becomes less pronounced towards the core top and, preserved remains of plants and/or wood are visible. From 2 m towards 1 m, the colour grades to a dark gamboge with some larger preserved organic fragments in the between 60 and 45 cm and roots above 40 cm (figure 4.1).

The 0-1 m section of T01 was broken up into four segments using colour, structures and textures visible in the x-ray and RGB photo of the section as well as organic matter visible in the RGB photo.

Beginning at the base of T01 (0 - 1 m section, figure 4.1), Segment IV (100 - 69 cm) can be characterized by a dark greyish gamboge colour (Hex value: #403626), with sparse visible organic matter. X-ray of the section show faint horizontal bedding of alternating lighter and darker layers, that are on average, ~1 cm thick throughout this segment.

The contact between segments IV and III at 69 cm occurs where x-ray imagery shows a switch from smooth-textured, horizontally-bedded sediments in segment IV, to massive, mottled sediments without any structure in Segment III. This switch is also characterised by an abrupt colour change to a dark greyish vermillion (#48261a), and a change from sediments with sparse visible organic matter to sediments that appear abundant in visible organic matter. Segment III (69 - 29 cm core depth) grades upwards from dark greyish vermillion in colour to a very dark vermillion (#1f1714) at 51cm and then to a dark greyish vermilion (#3c271f) at 30cm. Above 51cm, roots are abundant.

A distinctive dark, horizontal band (ca. 1 cm thick) in the x-ray data mark the transition to Segment II. Otherwise, segment II (29 – 20 cm) is mottled in appearance and shows little structure except for a sharp transition at 22 cm from darker (denser) to lighter (less dense) sediments. Visible organic matter in this layer include densely packed roots and detritus. The x-ray shows faint root traces extending from segment II about 7 cm down into segment III. The colour of the sediments are a moderate gamboge (#80643f).

The transition between segment II and I is characterized by a colour change to a dark tangelo (#553924) and reduction in visible organic matter. Finally, Segment I is characterized by faint root traces and no observable structures on the x-ray images. Organic matter includes both living and preserved roots. The colour of the sediment grades upwards from moderate gamboge to a dark tangelo (#3c2518).

4.3.2 Magnetic Susceptibility and Elemental Profiles

In sediment core T01, magnetic susceptibility (figure 4.3) hovers around 1.5. From 29 cm, magnetic susceptibility gradually decreases upwards to ~0.9 at the core top. There are two significant spikes showing higher mag sus values of 4.76 and 3.17, at 97 and 99 cm, respectively. Mag sus values decrease to 0.73 SI units between ca. 50-53 cm down core.

The elemental profile of Si (figure 4.3) fluctuates low in the core, ranging from 173,000 to 30,000 ppm, but shows a decreasing trend from the core bottom towards ~44,000 ppm 53 cm. Between 53 and 34 cm, Si hovers around 50,000 ppm with a drop to 13,000 ppm at 48 cm. Upwards from 34 cm, Si generally fluctuates between 100,000 and 50,000 ppm, showing an increasing trend toward the core top. This interval is also characterized by major spikes at 32, 29 and 15 cm, with concentrations of 126,000, 121,000 and 173,000 ppm, respectively.

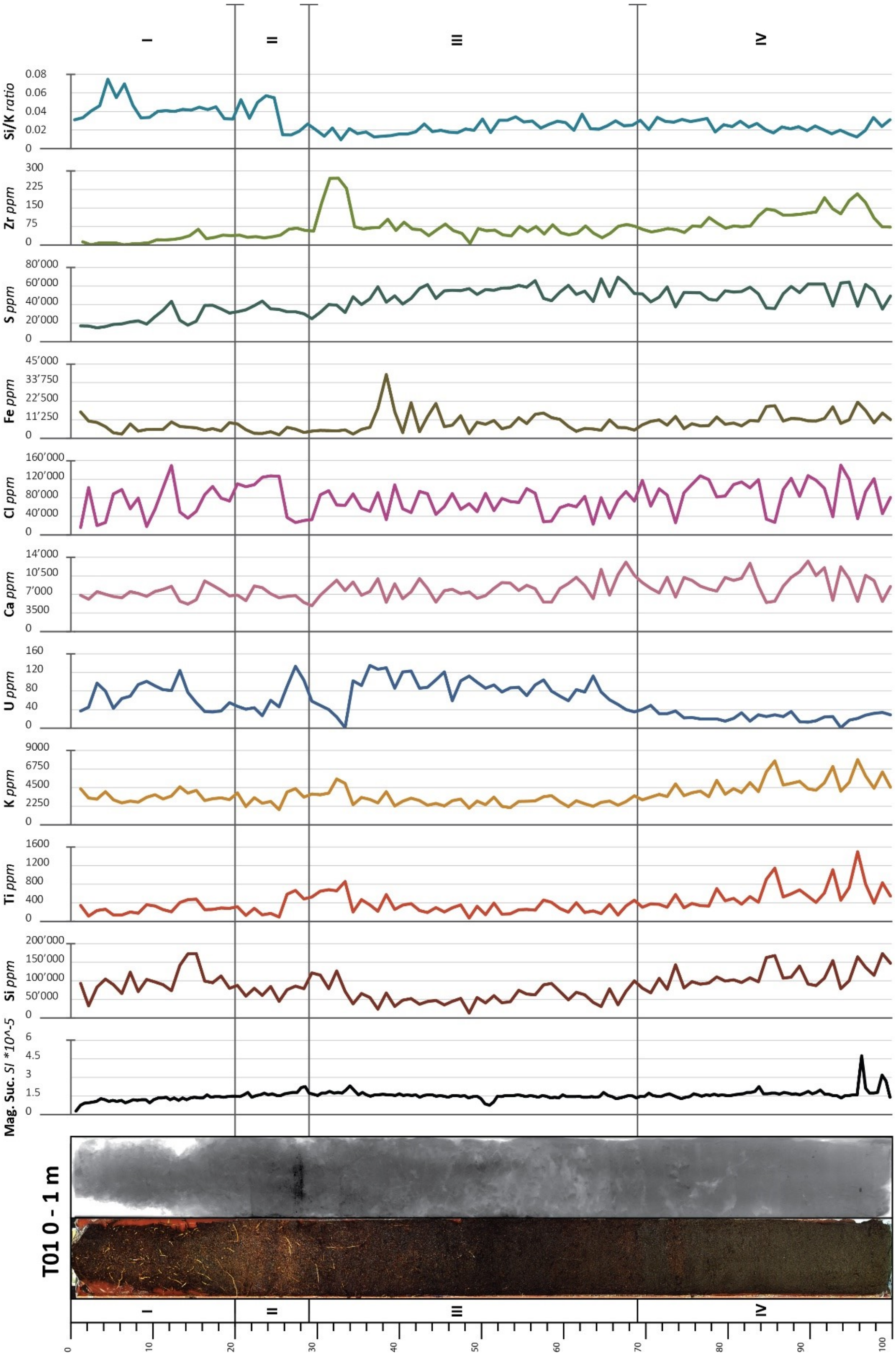

Figure 4.3 Magnetic susceptibility measurements, elemental profiles of Si, Ti, K, U, Ca, Cl, Fe, S and Zr and the ratio Si/Ti for T01 0 – 1 m section.

The elemental profile of Ti (figure 4.3) fluctuates between 400 and 1500 ppm from the core bottom upwards to 83 cm. Upwards from 83 cm, Ti decreases, hovering around 300 ppm between 67 and 34 cm. At 34 cm, Ti increases sharply from 203 to 856 ppm into a peak area between 35 and 26 cm. At 26 cm, Ti drops from 583 to 93 ppm, and remains fairly stable, hovering around 200 ppm upwards to the core top.

The elemental profile of K (figure 4.3) follows the same pattern as Ti, fluctuating between 4000 and 8000 ppm from the core bottom upwards to 83 cm. Upwards from 83 cm, K decreases, hovering around 3000 ppm between 67 and 34 cm. At 34 cm, K increases sharply from 2435 to 5000 ppm into a peak area between 35 and 26 cm. At 26 cm, Ti drops from 3955 to 1829 ppm, and remains fairly stable, hovering around 3000 ppm upwards to the core top.

The elemental profile of U (figure 4.3) starts off low at the core bottom with ~20 ppm. Upwards U increases gradually to 38 ppm at 68cm, and then sharply to 112 ppm at 63cm. From 63 to 34 cm, U fluctuated between 60 and 135 ppm, showing an increasing trend upwards. At 33 cm, U drops sharply below the detection limit of the measurement instrument (U = 1). Upwards from 33 cm, U fluctuates between 25 ppm and 130 ppm with a fairly stable interwall of ~40 ppm between 46 and 36cm.

The elemental profile of Ca (figure 4.3) is characterized by fluctuating values. Peak areas of Ca show a decreasing trend from the core bottom to the core top with peak values decreasing from ~13,000 to 8,500 ppm. Troughs in Ca range from 5,000 to 6,000 ppm throughout the core.

The elemental profile of Cl (figure 4.3) is characterized by highly fluctuating values that covaries with Ca. Peak values suggests a decreasing trend from the core bottom to 30 cm. Fluctuation is highest low in the core, with values ranging from 26,000 to 150,000 ppm from the core bottom to 69 cm. Between 69 and 30 cm, Cl is more stable with values ranging from ~40,000 to ~100,000 ppm. There is a trough area of about ~30,000 ppm between 30 and 26 cm, followed by a sharp increase to ~126,000 ppm. Upwards from 26 cm, values range from 16,000 to 150,000 ppm. Here, trough areas suggest a decreasing trend.

The elemental profile of Fe (figure 4.3) fluctuates low in the core with values ranging from 10,000 to 20,000 ppm from the core bottom to 83 cm, followed by a fairly stable stretch, hovering around 10,000 ppm up to 60 cm. Upward from 60 cm, values start fluctuating again, ranging from 3,000 to 20,000 ppm up to 40 cm, where Fe spikes, reaching 39,000 ppm at 38cm. Upwards from 36 cm, Fe remains stable, hovering around 5,000 ppm.

The elemental profile of S (figure 4.3) remains fairly stable from the core bottom to ~34cm, hovering around 50,000 ppm. From 34 cm, S decreases gradually to 17,000 ppm towards the core top.

The elemental profile of Zr (figure 4.3) increases from 73 to 207ppm from the core bottom to 95 cm. Upwards from 95 cm, Zr decreases to 51 ppm at 74 cm. Between 74 and 34 cm, values range from 7 to 104 ppm, but generally hovers 50 ppm. Between 34 and 29 cm, Zr spikes, reaching 271 ppm at 32 cm. Upwards from 29 cm, Zr gradually decreases from 57 ppm to ~1 ppm at the core top.

The Si/Ti ratio (figure 4.3) remains fairly stable from the core bottom to 36 cm. Upwards from 95 cm, the ratio increases from 100 to 323 at 62 cm, followed by a gradual decrease to 129 at 26 cm. At 25 cm, the ratio increases sharply to 479. Upwards from 25 cm the ratio decreases to 289 at 9 cm, followed by a spike between 9 cm and the core top, reaching 653 at 5cm.

4.3.3 Foraminifera

Presented below (next page) in table 4.2 and table 4.3 are total and relative (percent of assemblage) counts of foraminifera respectively. Counts from samples where one or two eights were counted have been multiplied to represent the same sediment volume as the samples counted in full. Foraminiferal subsamples from all segments in T04 and T05 were investigated for foraminifera, but not counted. These revealed agglutinated species in all segments of core T04 and core T05. Testate amoebae were not identified to species, nor counted; only presence/absence was recorded in subsamples from core T01 (Table 4.2).

Table 4.2 Total counts of foraminifera.

Depth (cm)	*M. fusca*	*J. Macrescens*	*T. inflata*	Unidentified trochamminid spp. type 1	Unidentified trochamminid spp. type 2	Organic Linings (excluding *T. Comprimata*)	Organic Lining *T. comprimata*	total	Testate amoeba
1*	304	2224	32	0	0	48	0	2608	Yes
5	379	3153	51	0	0	38	0	3621	Yes
40*	664	1480	592	0	0	792	0	3528	Yes
60	104	722	166	0	0	205	3	1200	Yes
90**	984	188	44	0	0	1628	0	2844	Yes
140	906	13	12	17	60	2220	739	3967	Yes
160	115	0	18	0	43	690	624	1490	Yes
180	417	6	2	8	37	879	941	2290	Yes
200	131	9	5	1	15	611	594	1366	Yes

*1/8 counted **2/8 counted

Table 4.3 counts of foraminifera expressed as percent of total assemblage.

depth	*M. fusca*	*J. Macrescens*	*T. inflata*	Unidentified trochamminid spp. type 1 and 2	Organic Linings (excluding *T. Comprimata*)	Organic Lining *T. Comprimata*
1*	11.66	85.28	1.23	0	1.84	0
5	10.47	87.08	1.41	0	1.05	0
40*	18.82	41.95	16.78	0	22.45	0
60	8.67	60.17	13.83	0	17.08	0.25
90**	34.60	6.61	1.55	0	57.24	0
140	22.84	0.33	0.30	1.94	55.96	18.63
160	7.72	0.00	1.21	2.89	46.31	41.88
180	18.21	0.26	0.09	1.97	38.38	41.09
200	9.59	0.66	0.37	1.17	44.73	43.48

*1/8 counted **2/8 counted

Five different agglutinated species of foraminifera were observed in the assemblages: *J. macrescens, T. Inflata*, *M. fusca*, and two unidentified trochospiral foraminifera species (presented as type 1 and 2). One species, *T. Comprimata*, was identified based on linings alone. Photos of these six species taken throught the eyepiece of the microscope are presented in figure 4.4. Two more species, *B. pseudomacrescens* and *H. Wilberti*, might be present in the assemblages, but were counted as *J. macrescens* due to difficulty with differentiation.

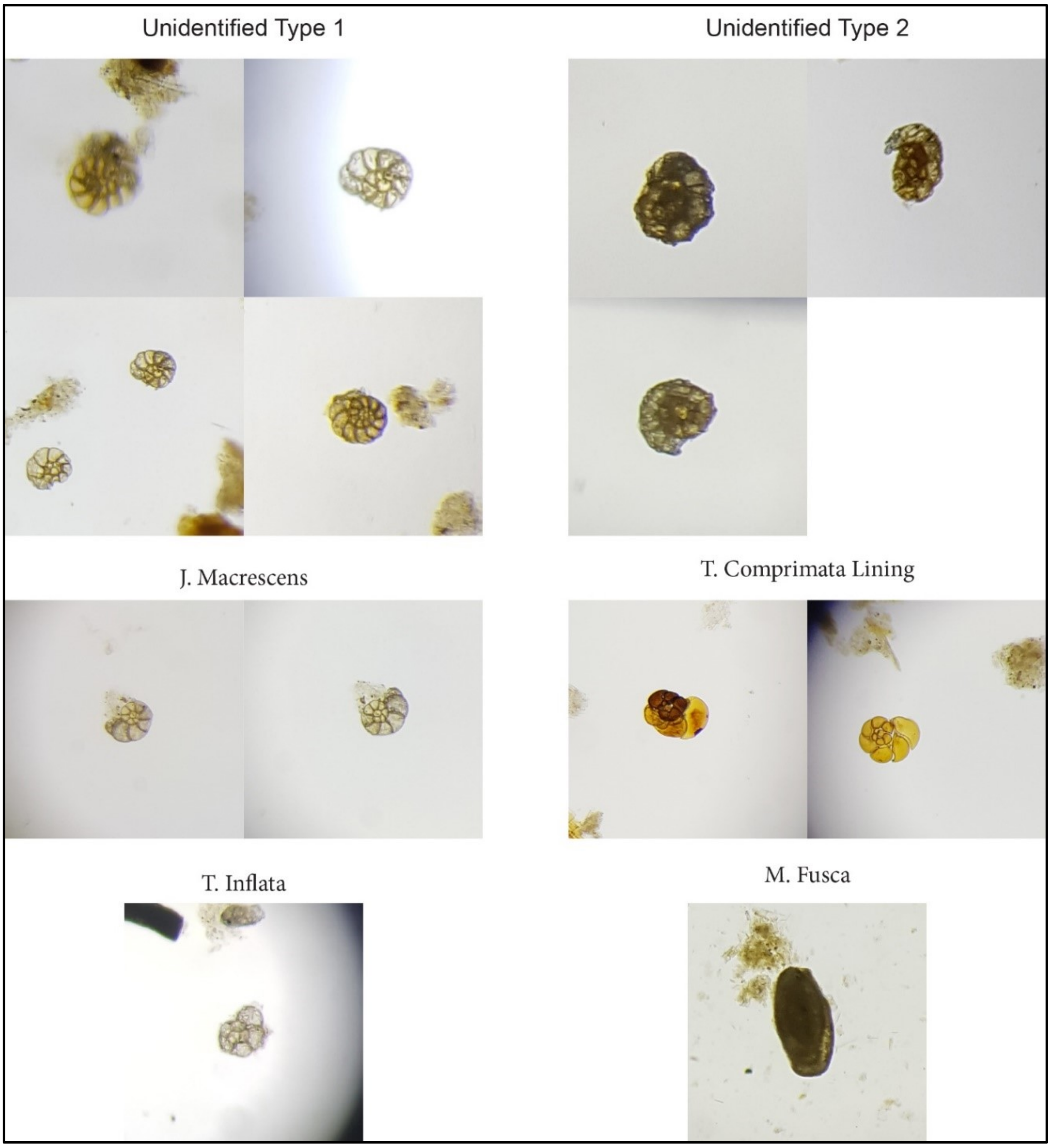

Figure 4.4 Photographs of foraminifera specimens taken with a Samsung galaxy s7 camera through the microscope eyepiece. Scale bar not available. General size between 63 µm and 125 µm.

Unidentified trochaminid type 1 is differentiated from *J. macrescens* due to its general chamber size and number of chambers. It also has a higher degree of trochospiral arrangement of the coil resulting in a dome like shape that is not apparent on the photographs. Unidentified trochaminid type 2 uses coarser grains in their tests than the other foraminifera species making it difficult to identify the shape of the chambers. Individuals are fragile and broke easily when flipping. The aperture of these was not found on any individuals of this species.

Miliammina fusca was the easily identified due to its unique shape and because it does not share morphological similarities to the other foraminifera species of the assemblage. Below ~50 cm, M. fusca individuals were grey in colour, whereas above they were pale brown. This might be due to some variance in their living environment (e.g. sediment available for test formation) and/or the downcore environment (e.g. acidity).

Mature individuals of *T. inflata* and *J. Macrescens* were identified based on the general shape and number of chambers and degree of trochospiral arrangement of the coil. If in doubt, the aperture, if visible, was used to differentiate. Differentiating juveniles from *J. macrescens* was more difficult, however, the inflated shape of *T. inflatas* chambers was used to differentiate.

Based on SEM imagery, a number of individuals in the upper samples looked most like *B. pseudomacrescens*. However, differentiating between *B. pseudomacrescens* and *J. Macrescens* was difficult. In a number of cases key aspects of the investigated individual were distorted (e.g. umbilical side was attached to something else) or missing (e.g. missing final chamber). Therefore, both species were counted as *J. Macrescens*. Similarly, in some few instances individuals interpreted as *J. macrescens* were remarkably similar to SEM images of *H. Wilberti*.

Organic linings were counted as they were increasingly abundant with depth, comprising more than 50% of the total assemblage below 90cm depth, and nearly 80% below 140cm depth. Without their tests, linings are prone to disintegration. Very commonly the final chamber of the linings, containing the aperture, was missing, making identification ambiguous. Differentiation of linings was considered an unfeasible undertaking, and these were therefore counted together. All counted linings were trochospiral. Most are believed to be *J. Macrescens*, and some might have been *B. pseudomacrescens*, *H. Wilberti* and *T. inflata*. Due to the number of linings in the samples, it is likely that a significant amount of these were destroyed during wet-sieving. This also implicates that linings of certain species were preferentially destroyed in the wet-sieving process, and consequently lost to the count.

Although linings were lumped together, a very distinct type of linings appeared below 90 cm, and dominated (~40% of total assemblage) below 160 cm. No similar tests were found, however, their uniqueness allowed for easy differentiation, and they were duly counted separate from other linings. The general shape of this lining is most similar to the descriptions of *T. Comprimata*. Alternatively, they also share morphological similarities to the calcareous subtidal species *Rosalina anomala* which was observed by Alve and Murray (1999) in the Oslo fjord from the intertidal zone to 5m depth, but only making up more then 5% of the assemblage at 2m water depth. These linings are presented as *T. Comprimata* linings.

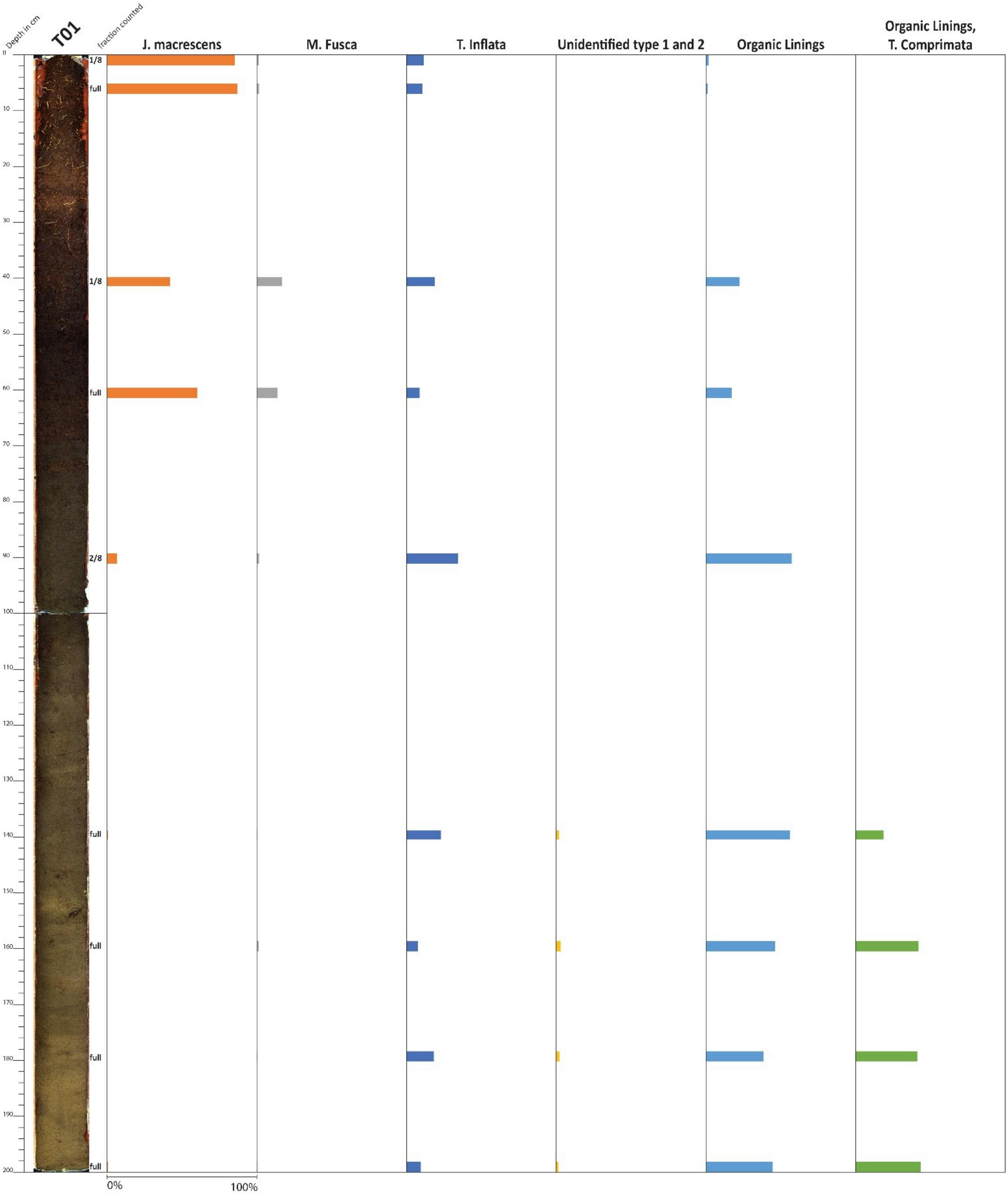

Figure 4.5 Counts of foraminifera presented as percent of total assemblage.

Species diversity appears to increase with depth in the core. Above 90 cm depth, 3-4 species are observed, *J. macrescens, T. Inflata, M. Fusca and T. Comprimata* (linings). Below 140cm depth 5-6 species are observed, *T. Comprimata* (linings), *M. Fusca, T. inflata, J. macrescens* and unidentified trochospiral foraminifera types 1 and 2.

Above 60cm*, J. macrescens* dominates the assemblages, with the highest total (3153) and relative abundance (87.08%) at 5cm. Miliammina fusca was present in every sample in core T01. Peak abundances occurred at 90cm and 140cm (984 and 906, respectively). Organic linings outnumber *M. fusca* tests in all but the upper two samples. When excluding organic linings, a transition from *M. fusca*- to *J. macrescens*-dominated assemblages between 60cm and 90cm is apparent (figure 4.6).

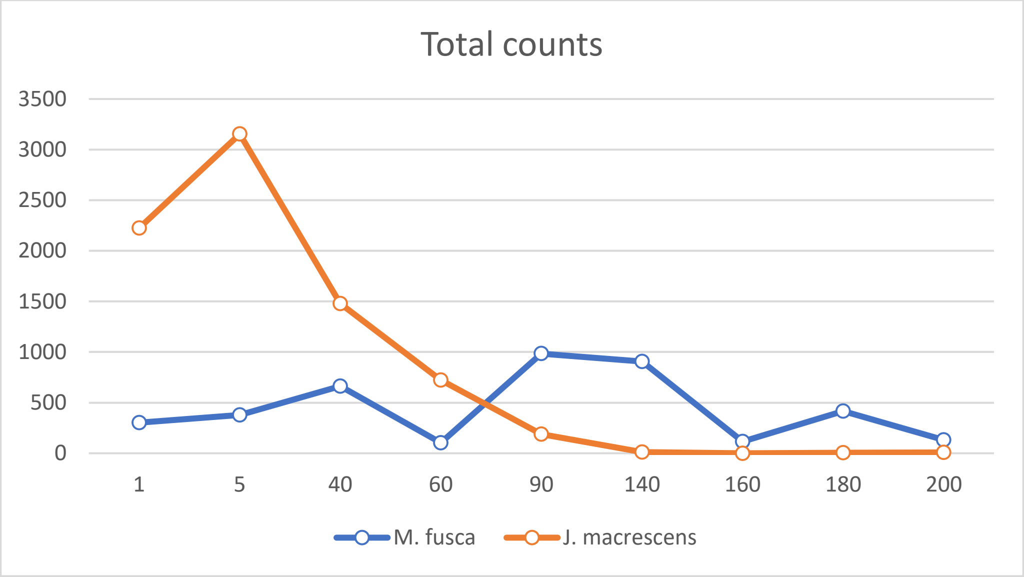

Figure 4.6 total counts of J. macrescens and M. fusca. X-axis not to scale.

4.4 Core T04

4.4.1 Stratigraphy

The 0-1 m section of T04 was broken up into five segments using colour, structures and textures visible in the x-ray and RGB photo of the section as well as organic matter visible in the RGB photo.

Beginning at the base of T04 (0-1m section; figure 4.7), Segment V (100- 64cm) can be characterized by a dark greyish gamboge colour (#5a4d32), with many organic fragments, including roots and reed detritus. The x-ray shows very faint horizonal bedding of alternating lighter and darker layers, that are on average, ~1cm thick.

The contact between segment V and segment IV occurs where the x-ray shows a transition from smooth-textured, horizontally-bedded and less dense (lighter) sediments to sediments appearing more coarse-textured and dense (darker). In segment IV (64cm to 45cm), the colour of the sediment grades from dark greyish gamboge at the contact with segment V to a very dark greyish tangelo (#342a23) at 54 cm. Between 51 and 45 cm the colour of the sediment brightens to a dark tangelo (#5c3c24). Visible organic matter is more abundant than in segment V, including wood fragments, roots and reed detritus. The x-ray shows a structure of slightly inclined, alternating, denser (darker) layers, approximately 6 cm thick that appear coarse-textured and, smooth-textured, less dense (lighter) layers, approximately 4 cm thick. The x-ray also shows lighter root traces, extending down from segments III and II.

The transition between segment IV and III occurs at 45 cm, where the x-ray shows a transition from the thick alternating, slightly inclined layers to, denser (darker), coarse-textured sediments with no structure. In segment III (45 – 40 cm), the sediment can be characterized by a moderate to dark tangelo colour (#6f4529) and no observable structure in the x-ray. Visible organic matter is highly abundant, mostly roots.

The transition from segment III to segment II is marked by an abrupt colour change to dark vermillion (#4b2c1e). This is also reflected in the x-ray as a transition from denser (darker), to less dense (lighter) sediments. In segment II (40 – 20 cm), the sediment can be characterized by its dark vermillion colour and densely packed organic matter, mostly roots and detritus from reeds. The x-ray shows multiple root traces in this segment, one extending down to 59cm.

The transition to segment I occurs where the x-ray shows a transition from less dense sediments to denser, mottled sediments that appear more coarse-textured. Finally, segment I (20 – 0 cm) is characterized by faint root traces and no observable structures in the x-ray. Visible organic matter includes both living and preserved roots. The colour of the sediment is a dark tangelo (#4a3022).

4.4.2 Magnetic Susceptibility and XRF-Measurements

In sediment core T04, magnetic susceptibility (figure 4.7) hovers around 1.5 SI units between the core bottom (100 cm) and 38 cm. Upwards from 38 cm, mag suc hovers around 1 SI unit. There are three significant spikes at 14, 60 and 79 cm, showing mag suc values of 4.77, 6.62 and 5.32 SI units, respectively.

The elemental profile Si (figure 4.7) remains fairly stable low in the core, ranging between 200,000 and 165,000 ppm from the core bottom to 65 cm. At 65 cm, Si concentrations decrease, hovering around 140,000 ppm upwards to 50 cm. At 50 cm, Si drops from 156,000 to 80,000 ppm, remaining at that level upwards to 48cm. Between 48 and 34 cm, concentrations fluctuate somewhat, ranging from 138,000 to 77,000 ppm. Upwards from 34 cm, concentrations drop to 37,000 ppm at 32 cm, and remains fairly stable upwards to 20 cm, ranging between 15,000 ppm and 40,000 ppm. At 21 cm, Si increases to 86,000 ppm, hovering 90,000 ppm upwards to 9 cm. Between 9 cm and the core top, Si ranges between 10,000 and 5,000 ppm.

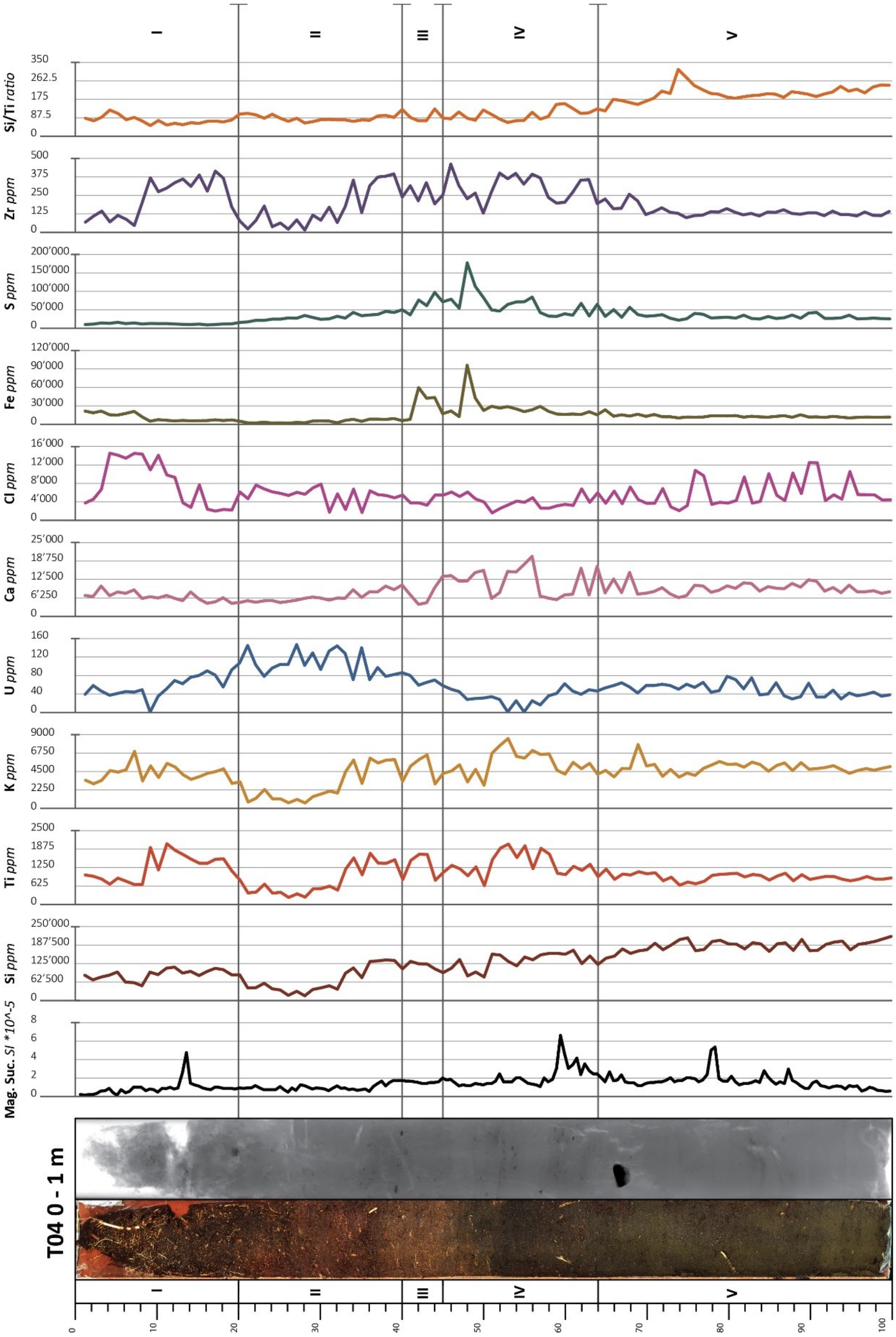

Figure 4.7 Magnetic susceptibility measurements, elemental profiles of Si, Ti, K, U, Ca, Cl, Fe, S and Zr and the ratio Si/Ti for T04 0 – 1 m section.

The elemental profile of Ti (figure 4.7) remains fairly stable low in the core, hovering 900 ppm upwards to 67 cm, with a small drop to 750 ppm between 77 and 72cm. Upwards from 67 cm, Ti fluctuates, but shows a gradual increasing trend, peaking at 2050 ppm at 53 cm, and then drops to 640 ppm at 50 cm. Between 50 and 34 cm, Ti fluctuates, ranging between 640 and 1700 ppm, showing a slightly increasing trend. At 32 cm, Ti drops to 490 ppm, and remains fairly stable upwards to 21 cm, ranging between 250 and 500 ppm. Upwards from 21, Ti shows an increasing trend peaking at 11 and 9 cm (2050 and 1900 ppm, respectively), followed by a drop to 680 ppm at 8 cm, and a slight increasing trend towards 1000 ppm at the core top.

The elemental profile of K (figure 4.7) follows the same general pattern as Ti. Low in the core, K remains stable, hovering 5000 ppm up to 77 cm. Upward from 76 cm, K shows an increasing trend, peaking at 53 cm with 8500 ppm, interrupted by a spike at 69 cm of 7800 ppm. At 50 cm, K drops to 2800 ppm. Between 50 and 34 cm, K fluctuates between 2800 and 6500 ppm, showing a slightly increasing trend. At 32 cm, K drops to 1800 ppm, and remains fairly stable upwards to 21 cm, ranging between 650 and 2000 ppm. Upwards from 21 cm, K increases, reaching 4800 ppm, followed by an increasing trend towards 7000 ppm at 7 cm. Between 7 cm and the core top, K drops to 3400 ppm.

The elemental profile of U (figure 4.7) remains fairly stable, hovering 50 ppm from the core bottom upwards to 60 cm. Upwards from 60 cm, U decreases, dropping below the detection limit of the measurement instrument at 55 and 53 cm (U=1). Upwards from 53 cm, U shows an increasing trend, peaking at 35 cm with 140 ppm. Between 35 and 21 cm, U fluctuates between 70 and 150 ppm, with peaks generally ranging between 140 and 150 ppm. Upwards from 21 cm, U shows a decreasing trend towards 40 ppm the core top, interrupted by a sharp drop below the detection limit (U=1) at 9 cm.

The elemental profile of Ca (figure 4.7) remains fairly stable from the core bottom to 69 cm, ranging between 7500 to 12,000 ppm. Upwards from 69 cm, Ca fluctuates between 17,000pp and 7000 ppm, followed by a stable stretch of ~6500ppm between 61 and 57 cm. At 56 cm, Ca increases sharply to 20,000 ppm. Upwards from 56 cm, Ca shows a decreasing trend toward 4400 ppm at 19 cm, interrupted by sharp drops at 51 and 42 cm (6000 and 4000 ppm, respectively). Upwards from 19 cm, Ca shows a slightly increasing trend towards 10,000 ppm at 3 cm.

The elemental profile of Cl (figure 4.7) fluctuates strongly low in the core, ranging between 2000 and 12,500 from the core bottom to 61 cm, however, there is a decreasing trend in peak values from 12500 at 90 cm to 6800 ppm at 62 cm. Upwards from 61 cm, Cl shows a general increasing trend towards 7600 ppm at 22 cm, interrupted by some sharp drops to ~2000 ppm. Upwards from 22 cm, Cl drops to a trough area between 19 and 13 cm of ~2000 ppm. Between 13 and 11 cm, Cl increases sharply to 14,000 ppm, and remains fairly stable upwards to 4cm before dropping to 4000 ppm at the core top.

The elemental profile of Fe (figure 4.7) is stable at ~12,000 ppm from the core bottom upwards to 66 cm. Upwards from 66 cm, Fe increases gradually to 29,000 ppm at 51 cm, followed by spikes to 96,000 ppm at 48 cm and 60,000 ppm at 42 cm. Upwards from 41 cm, Fe decreases from 8000 ppm to 1700 ppm at 26 cm, before gradually increasing toward 20,000 ppm at the core top.

The elemental profile of S (figure 4.7) is fairly stable, hovering around 30,000 ppm from the core bottom upwards to 69 cm. Between 69 and 61 cm, S fluctuates between 30,000 and 67,000 ppm, followed by a stable stretch of ~37,000 ppm from 61 to 57 cm. Between 57 and 41 cm, S spikes three times, at 56, 48 and 44 cm, with concentrations of 84,000, 177,000 and 97,000 ppm, respectively. Upwards from 41 cm, S gradually decreases from 50,000 towards 10,000 ppm at the core top.

The elemental profile of Zr (figure 4.7) is fairly stable, hovering around 130 ppm from the core bottom to 70 cm. Upwards from 70 cm, Zr fluctuates strongly. Still, Zr shows an increasing trend towards 460 ppm at 46 cm. Upwards from 46 cm, Zr decreases to 20 ppm at 21 cm. Between 21 and 17cm, Zr increases sharply to 415 ppm, and remains high upward to 9 cm, where Zr starts to decrease sharply down to 44 ppm at 7, remaining low toward the core top.

The Si/Ti ratio (figure 4.7) is highest low in the core. Beginning at 241 at the core bottom, Si/Ti shows a slight decreasing trend towards 179 at 81cm. Upwards from 81 cm, Si/Ti increases gradually to 316 at 74cm. Further upwards, Si/Ti decreases, rapidly at first to 202 at 73 cm, and then more gradually towards 65 at 53cm. Between 53 cm and the core top, Si/Ti remains fairly stable, hovering 75.

4.5 Core T05

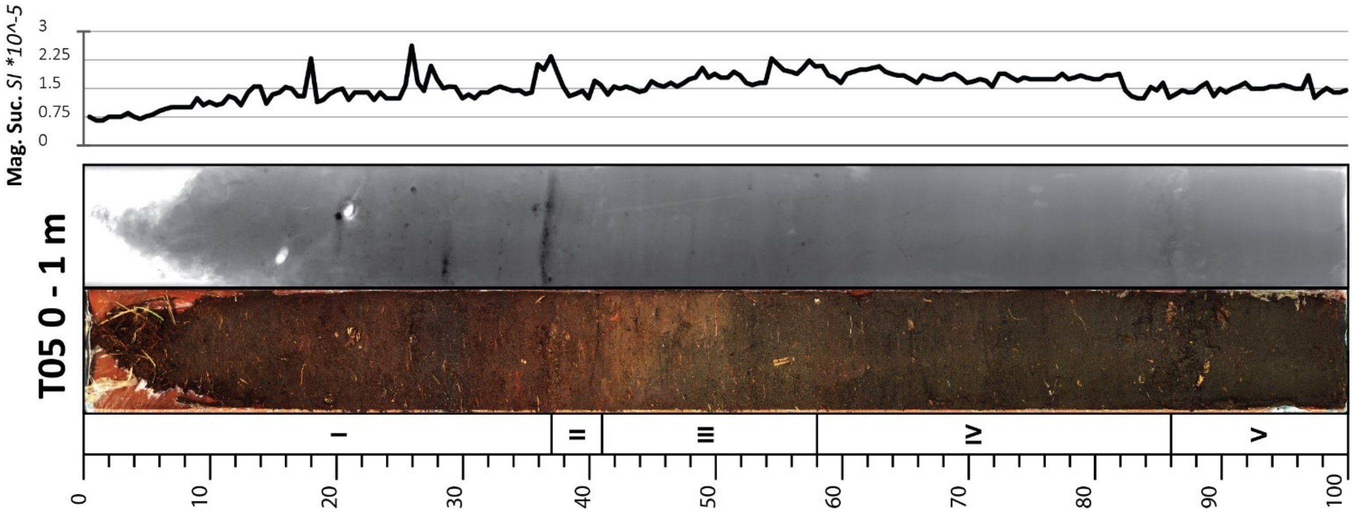

Figure 4.8 Magnetic susceptibility measurements of T05 0 – 1 m section.

4.5.1 Stratigraphy

Beginning at the base of T05 (0-1 m section), segment V (100-86) In segment V, the sediment can be characterized by a dark greyish gamboge colour (#352c20), with visible organic matter including plant detritus and pieces of wood. The x-ray shows smooth-textured sediments and faint, slightly inclined, horizontal bedding of alternating lighter and darker layers, that are on average, ~1 cm thick throughout this segment (Fig. x).

The contact between segment V and IV is marked by a ~4 cm thick layer of mottled sediments, mostly consisting of organic matter. The depth of this contact is set based on the deepest visible root in the core. In segment IV (86 to 58cm) the sediment colour grades from a dark greyish brown (#423526) at the contact with segment V, to a lighter dark greyish Tangelo (#4b3626) at 60 cm. The x-ray reveals a similar structure to segment V. Visible organic matter is more abundant than in segment V, and includes roots.

The transition between segment IV and III is marked by a colour change from a dark greyish tangelo to brown (#5b442c). In segment III (58 to 41cm), the sediment between 58 and 50 cm can be characterized by its brown colour, whereas between 50 and 41 cm, the sediment colour is mixed between brown and a moderate tangelo (#825231). Visible organic matter is more abundant than in segment IV and, includes roots and plant detritus. The x-ray shows that the sediment is denser (darker), appearing more coarse-textured than segment IV. The x-ray also shows a structure, alternating between denser and less dense, slightly inclined layers, ranging in thickness between ~1 to ~0.5 cm. Faint root traces are also visible in this segment, extending down from segment II and I.

The contact between segment III and II is marked by a colour change from moderate tangelo to a dark tangelo (#5a331e). In segment II (41 to 37cm), the sediment can be characterized by its dark tangelo colour. The x-ray shows that the sediment is somewhat denser and appears more coarse-textured than segment III. Visible organic matter includes roots and plant detritus.

The contact between segment II and I is marked by a layer of visible white/opaque sediment grains, appearing as a very dense layer in the x-ray. Finally, in segment I (37 to 0cm) the sediment can be characterized by a dark vermillion colour (#543123), and densely packed organic matter. Visible organic matter includes roots, rhizomes and plant detritus. The x-ray show that the sediment density and texture varies within this segment. Between 37 and 30 cm, the sediment has a faint horizontal bedding and is fairly smooth-textured. Between 30 and 20 cm, the sediment is horizontally bedded, but is denser and appears more coarse-textured than between 37 and 30 cm. Above 20 cm, the sediment is massive, with no structure. In the x-ray, rhizomes appear as white ovals, and some root traces are visible within segment I.

In sediment core T05, magnetic susceptibility hovers around 1 SI unit between the core bottom (100 cm) and 82cm, 1.5 SI units between 82 and 45 cm and 1 Si unit between 45 and 14 cm. Upwards from 14 cm, mag suc gradually decreases to -0.13 SI units. There are three significant spikes at 18, 26 and 37 cm, showing mag suc values of 2.05, 2.51 and 2.12 SI units, respectively.

4.6 Vegetational Zonation

Six vegetation zones, mudflat, salt marsh, two kinds of reedswamp, sedge fen and forest, were observed (summarized in table 4.4) at the Tranevåg study site. The mudflat was inaccessible due to the high storm surge water levels during fieldwork, and therefore, not possible to characterize beyond confirming its presence. The salt marsh (figure 4.9) comprises various low-growing vegetation, including halophytes and reeds, rushes and/or grasses (unidentified). Algae were abundant, floating at the water surface.

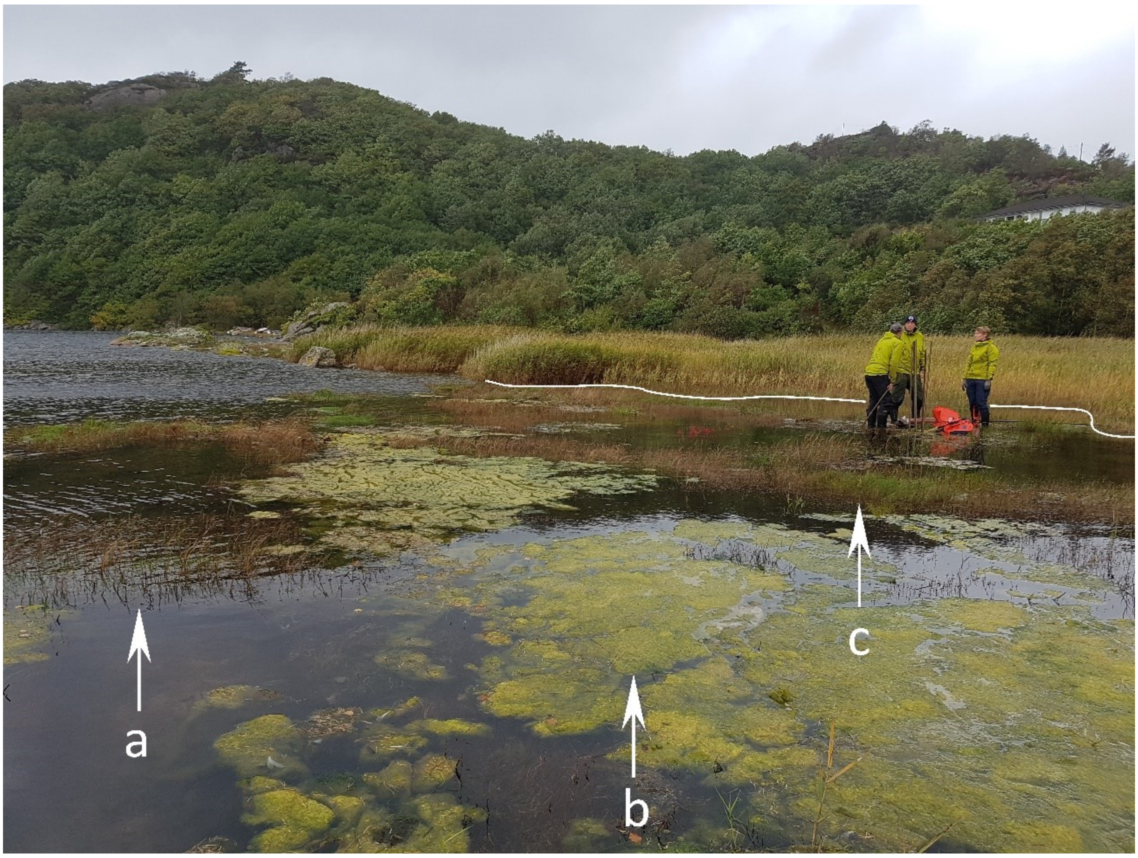

Figure 4.9 High tide inundating the lowest area of the saltmarsh at Travevåg. The white line delineates the upland edge towards the reedswamp. Halophytes (not visible), a, c) various low growing reeds/grass vegetation and b) algae.

The reedswamp at Tranevåg has two distinct zones. Firstly, the seaward zone (figure 4.10) consists mostly of a single species of reed reaching approximately 50 cm tall. The upland zone (figure 4.11) consists almost entirely of tall (up to two meters high) reeds thought be *Phragmites Australis* (common reed). These zones are both within the supratidal zone, above the highest astronomical tide and below annual highwater.

Figure 4.10 Seaward reedswamp consisting of low-growing reeds, unidentified species. The white line delineates the transition to the reedswamp zone dominated by *P. australis.*

The sedge fen zone (figure 4.12) is a hummocky area with a diversity of plant species. However, compact rush seems to be dominat. The sedge fen zone has historically been used for farming purposes (discussed in section 2.4.5) and might have been used for grazing. The hummocky morphology might therefore originate both from compact rushes and preferential grazing of cattle.

The forest zone transitions rather abruptly from the sedge fen and upland reedswamp zones. This zone has several leaf tree species and some pine species. The abruptness of the transition might be due to some threshold change in environmental conditions (likely a transition to exposed or thinly covered bedrock) and/or might be relict from former land use.

Figure 4.11 Upland reedswamp edge consisting of a) reeds thought to be *Phragmites australis* (common reed / Takrør) and, b) rushes thought to be *Juncus conglomeratus* (compact rush / Knappsiv)

Figure 4.12 Transition between reedswamp and sedge fen (black line), and woodland zone.

Table 4.4 Vegetation zones that were observed in the Tranevåg marsh. Species were identified from photos and were confirmed to be present at proximal sites from the online map service of the Norwegian Biodiversity Information Centre (Artsdatabanken, 2019).

Zones	Vegetation type
Mudflat	Pioneers, algae
Saltmarsh	Halophytes, algae, low growing reeds / rushes / grasses
Reedswamp (seaward)	Low growing reeds
Reedswamp (upland)	Tall reeds (*Phragmites australis).*
Sedge fen	Rushes (Juncus Conglomeratis) and various plants and flowers
forest	Pines and leafy trees, mosses

4.7 Elemental Correlations

Correlations between elements in the XRF data are presented below in table 4.2 and table 4.3. These were used to assess the relationships between elements.

Table 4.5 Significance levels (p value) of bivariate correlations for T01 between elements used in this thesis. Anticorrelations are marked red. Correlations that are not significant are marked "-".

Sig. Two tailed	Si	K	Ti	U	Ca	Cl	Fe	S	Zr	Ba
Si	1	.001	.001	.001	-	-	.05	.001	.001	.001
K		1	.001	.001	-	-	.001	-	.001	.001
Ti			1	.001	-	.005	.001	-	.001	.001
U				1	.001	.001	-	-	.001	.001
Ca					1	.001	-	.001	.05	.05
Cl						1	.05	.001	-	-
Fe							1	-	.05	-
S								1	.005	-
Zr									1	.001
Ba										1

Table 4.6 Significance levels (p value) of bivariate correlations for T04 between elements used in this thesis. Anticorrelations are marked red. Correlations that are not significant are marked "-".

Sig. Two tailed	Si	K	Ti	U	Ca	Cl	Fe	S	Zr	Ba
Si	1	.001	.05	.001	.005	.05	-	-	-	.01
K		1	.001	.001	.001	-	.001	-	.001	.001
Ti			1	.001	-	.05	.01	-	.001	.001
U				1	.001	-	.001	.01	.01	.001
Ca					1	-	.005	.001	.05	.001
Cl						1	-	-	.05	-
Fe							1	.001	.05	.01
S								1	.01	.001
Zr									1	.001
Ba										1

Chapter 5 Analysis and Discussion

5.1 Core Chronology

Along with radiocarbon dates (Table 4.1), variations in total Pb from XRF analysis, assumed to reflect primarily atmospheric Pb (see section 2.3.1; Steinness et al.,1997; McConnell and Edwards, 2008; Rizzo, et al., 2009), were used to develop an age model for the upper 40 cm of cores T01 and T04 (figure 5.1).

Dates tied to the Pb pollution history, as established in Greenland Ice Sheet (GIS) ice cores by McConnell and Edwards (2008), were compared to the elemental profiles of Pb in Tranevåg cores T01 and T04. Both T01 and T04 have similar elemental profiles of Pb compared to that of the GIS ice cores. Elemental profiles of Pb in the GIS ice cores can be characterized by a rapidly increasing trend from AD 1860, peaking in 1893 due to pollution by the coal industry, followed by a period of decreasing Pb concentrations, reaching a low point during the Great Depression. Due to the widespread usage of leaded gasoline, Pb reaches a second peak in 1970, followed by a decreasing trend due to regulations on Pb pollution, approaching pre-industrial levels at present (McConnell and Edwards, 2008).

The age model (figure 5.1) shows the elemental profiles of Pb in T01 and T04 and their interpreted ages based on Pb records from GIS ice cores (McConnell and Edward, 2008) as well as calibrated radiocarbon dates (table 4.1). A timeline of historical events is also included to demonstrate how the elemental profiles of lead were interpreted. The radiocarbon date at 70 cm depth in T01 coincides with a pre-industrial peak concentration in Pb. T04 also has a similar peak at 30 cm, and these are therefore interpreted as representing the same age. Based on the calibrated age of 519 ± 22 BP (table 4.1), this peak likely relates to European silver production during the 16th century (Marshall, 2015). The sharp increase at the base of core T01 was not interpreted as it occurs in disturbed sediments, although it may represent the peak pre-industrial European lead production, which occurred during Roman times (Marshall, 2015).

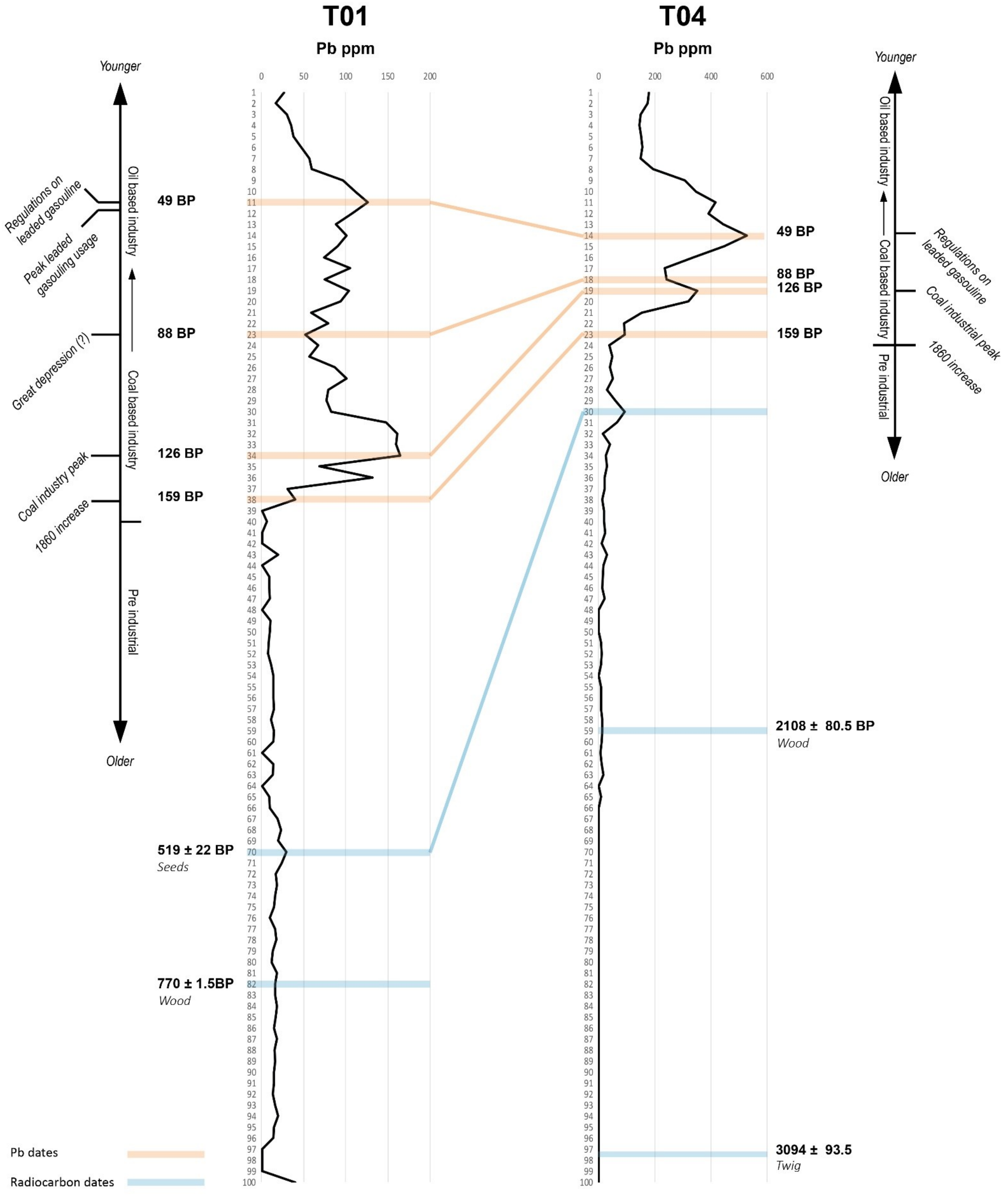

Figure 5.1 Age model based on radiocarbon dates (table 4.1) and variations in Pb as compared to the pollution history of Pb established from ice cores from the GIS.

5.1.1 Accretion Rates

The radiocarbon dates and Pb chronomarkers allow for accretion rates to be calculated between the dated horizons in T01 and T04 cores (presented in tables 5.1 and 5.2). As the analysed cores represent the top metre of sediment, compaction is assumed to be negligible and was not corrected for.

Table 5.1 Accretion rates for T01 0-1m.

Segment	Age range	Accretion rate
0 – 11 cm	Present – 49 BP	2.24 mm/yr
11 – 23 cm	49 BP – 88 BP	3.08 mm/yr
23 – 34 cm	88 BP – 126 BP	2.89 mm/yr
34 – 38 cm	126 BP – 159 BP	1.21 mm/yr
38 – 70 cm	159 BP – 519 BP	0.89 mm/yr
70 – 82 cm	770.5 BP – 519 BP	0.48 mm/yr

Table 5.2 Accretion rates for T04.

Segment	Age range	Accretion rate
0 – 14 cm	Present – 49 BP	2.86 mm/yr
14 – 18 cm	49 BP – 88 BP	1.03 mm/yr
18 – 19 cm	88 BP – 126 BP	0.26 mm/yr
19 – 23 cm	126 BP – 159 BP	1.21 mm/yr
23 – 30 cm	159 BP – 519 BP	0.19 mm/yr
30 – 59 cm	519 BP – 2108.5 BP	0.39 mm/yr
59 – 97.5 cm	2108.5 BP – 3094.5 BP	0.39 mm/yr

Both T01 and T04 show similar changes in accretion rates, which increase by an order of magnitude in the last ca. 500 years. Core T01, extracted from the low marsh, shows a larger increase in accretion rates compared to those of T04, which is positioned higher up on the salt marsh surface (19.5 cm above T01). Increasing accretion rates are a common response of salt marshes to rising RSL (Kirwan and Megonigal, 2013; Crosby et al., 2016; Müller-Navarra 2019), and correlate well with the local tide gauge data at Tregde, which indicates that RSL has been rising since it was installed, 92 years ago (at an average rate of 0.4 mm/yr; Romundset et al., 2015).

5.1.2 Cryptotephra Pre-Screening

In sediment cores, tephra layers have been associated with high magnetic susceptibility values and peak abundances of elements contained in the minerals SiO_2, TiO_2, Al_2O_3, FeO, MnO, MgO, CaO, Na_2O, K_2O and P_2O_5, depending on the geochemistry of the tephra layer (Kylander, 2012). Geochemical analysis of tephra also deomonstrates that some minor elements (e.g. Zr and Ba) can be associated with certain volcanic eruptions (e.g. Selbekk & Tønnes, 2006). Due to the considerable distance between Tranevåg and volcanically active sites (e.g. Iceland), any tephra layers in the upper meter must be cryptotephra (see section 2.3.1.2), meaning that they are impossible to spot with the naked eye. As such, the likelihood of these layers being reworked can also be considered as high, particularly via bioturbation (Kylander, 2012).

Based on the aforementioned minerals and elements, and considering correlations presented in table 4.5 and 4.6, XRF-derived elemental profiles of Si, Ti, K, Zr, Ba and Fe were chosen for tephra analysis in T01 (0 - 1 m section) and compared to the magnetic susceptibility data (figure 5.2). The peak areas in the elemental profiles that correspond to a peak are in magnetic susceptibility (figure 5.2; Kylander, 2012) are interpreted as most likely to contain cryptotephra (highlighted in orange). Note that magnetic susceptibility doesn’t match up perfectly to these peak areas, however this could be due to the different measurement methods (core scanning for the magnetic susceptibility vs discrete sampling at a 1 cm interval for the XRF analysis).

Because the elements considered for cryptotephra screening also occur as detrital terrigenous material, it is important to state that most peak areas may represent other discrete events like storms (i.e. surface runoff, input of detrital material like Fe-Ti oxides). Nonetheless, if future studies allow, the data presented here provides a useful guide or pre-screening tool for sampling potential cryptotephra layers, which if found, would improve the accuracy of our age model.

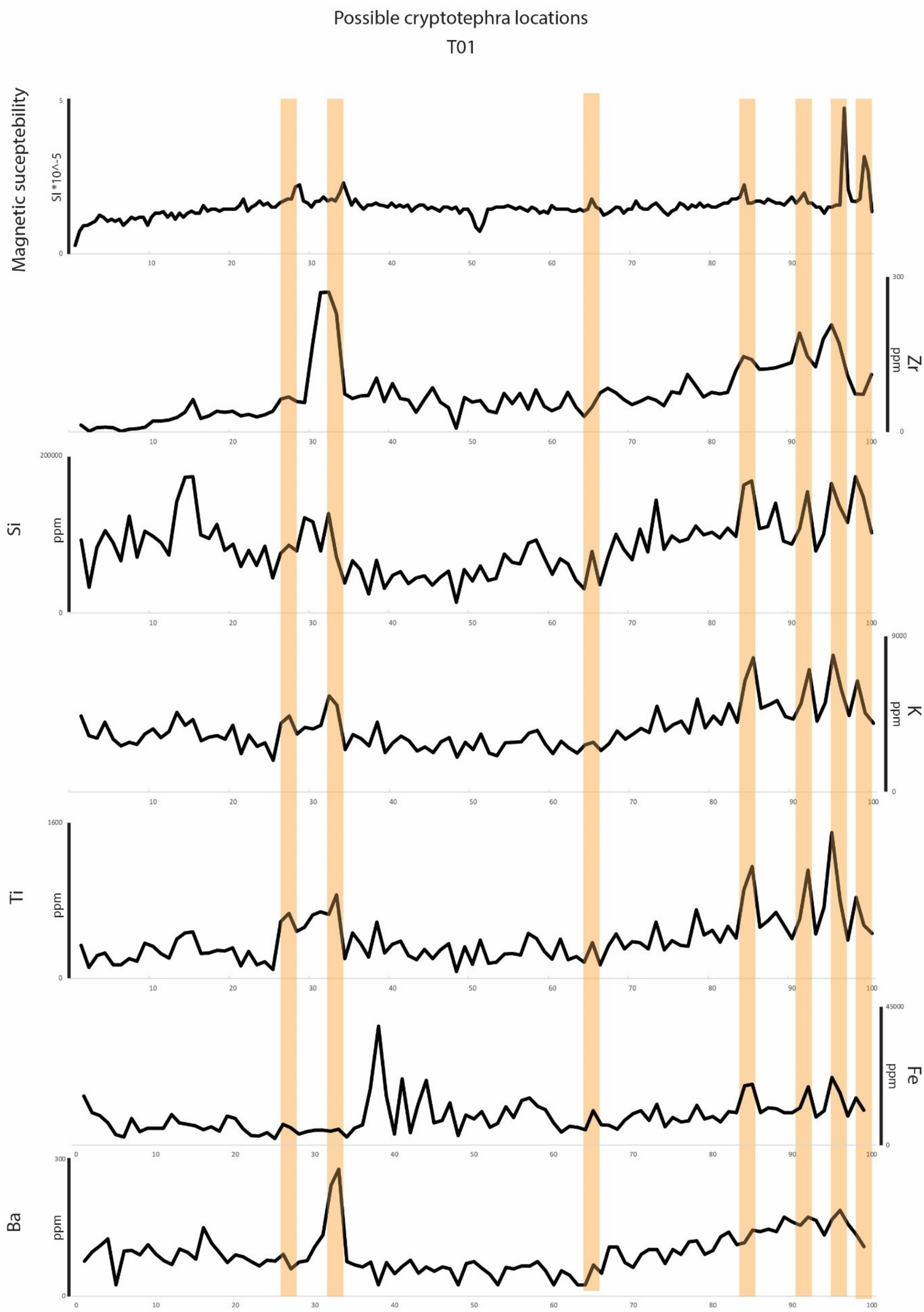

Figure 5.2 Possible locations of cryptotephra layers in T01 based on elements commonly used for tephra screening and magnetic susceptibility (Kylander, 2011; Westerhold et al., 2009). Orange lines indicate where elemental peaks correspond with peaks in magnetic susceptibility.

Halfidason et al. (2000) constructed a framework for Icelandic tephrochronology, compiling most known Icelandic eruptions and their measured geochemistry (SiO_2, TiO_2, Al_2O_3, FeO, MnO, MgO, CaO, Na_2O, K_2O and P_2O_5). Eruptions that are close in age based on our age model (figure 5.1) to the segments highlighted in figure 5.2, are listed in table 5.3. If layers of cryptotephra are present in the highlighted horizons (figure 5.2), these eruptions might represent the source and could therefore serve as additional dating markers. However, to confirm this hypothesis and apply the associated ages to the core chronology, geochemical analysis of the glass shards and comparison to the geochemical profiles of the different volcanic eruptions are needed. The next step to confirm that the peaks in the elemental profiles and magnetic susceptibility do indeed reflect the presence of cryptotephras, is to separate glass shards from the surrounding matrix and apply further geochemical analyses.

Table 5.3 Selected segments, possibly containing cryptotephra and the Icelandic volcanic eruptions that might correspond to these. The segments in the lower half of the core were not correlated to any known eruptions since their age is poorly constrained, making the number of eruptions that might correspond to them high. Eruptions and their ages are from Haflidason et al. (2000).

Depth in core T01	Approximate segment age BP (based on Pb data)	Possible corresponding volcanic eruption event	Eruption age BP	Eruption age AD
14 – 15 cm	55 BP	Surtsey	56 BP	AD 1963
		Askja	58 BP	AD 1961
26 – 27 cm	100 BP	Thingvallavatn	101 BP	AD 1918
		Unspecified	97 BP	AD 1922
32 - 33 cm	120 BP	SW Iceland	116 BP	AD 1903
		Vatnajökull, central iceland	127 BP	AD 1892
		Vatnajökull, central iceland	136 BP	AD 1883
37 – 38 cm	159 BP	Myrdal, S Iceland	159 BP	AD 1860
		Unspecified	157 BP – 155 BP	AD 1862-64
64 – 65 cm	Younger than 519 BP	< Not listed >		
83 – 84 cm	Older than 770 BP	< Not listed >		
91 – 92 cm				
95 – 96 cm				
98 – 99 cm				

5.2 Elemental Proxies

5.2.1 Titanium and Uranium

Elemental proxies associated with variations in terrigenous sediment delivery through time include, among others, major elements Ti, Si, Fe and K (Rothwell and Croudace, 2015). As shown in table 4.2 and 4.3, all terrigenous elements are positively correlated at significant levels in both T01 and T04, with the exception of Si and Fe in T04, suggesting that the major fraction of terrigenous detrital sediment at Tranevåg is derived from the same source, likely via weathering of local bedrock, transported and deposited by surface wash.

Titanium and K are highly correlated with almost identical elemental profiles in both T01 and T04 cores (figures 4.3, 4.4). Of Ti and K, Ti is the more commonly used proxy for terrigenous sediment delivery (Rothwell and Croudace, 2015). Iron is believed to have been remobilised (i.e. reworked) by redox conditions, as indicated by synchronous peaks of Fe and S throughout T04 (figure 4.4; Rothwell and Croudace, 2015). Variations in Si are believed to be influenced by biogenically sourced Si because high values in the Si/Ti ratio suggests that Si concentrations cannot be fully explained by terrigenous sediment delivery at the top of T01 (figure 4.3), and bottom of T04 (figure 4.4). Because of this and because Fe is appears to have been reworked throughout much of T04, Ti is preferred as an elemental proxy for terrigenous sediment delivery in both T01 and T04.

The anticorrelation of U and Ti in both T01 and T04 (table 4.2 and 4.3) indicates that U is not a component of the terrigenous detrital sediment. Based on the observations of Banks et al. (1988, see appendix 1), there is a stable supply of U in the groundwater of Tranevåg derived from the weathering of the local granitic bedrock. The resulting concentration might then also be relatively high due to the geologically short, postglacial weathering history (ca. 14,000-15,000 years; Fjeldskaar & Amantov, 2018). In addition, Shavatsev (2008) show that U is present in Scandinavian soil groundwater and that seawater can also have considerably high levels of U (discussed in more detail in appendix 1).

Based on experiments by Ahmad (2015), concentrations of U can be expected to reflect the U-sorption qualities of the sediment, particularly sorption capacity. Peat facies are expected to have high concentrations of U relative to other soil types due to their excellent sorption qualities (Ahmad, 2015; Brown et al., 2000). In broader terms, as organic material from vegetation and the production of humic acids are major factors for peats sorption qualities (Brown et al., 2000), it can be argued that U reflects the interplay of available U, vegetation type, inorganic-fraction and redox conditions. Assuming a steady supply of U and production of humic acids, the anticorrelation between U and Ti indicates that U reflects the organic fraction of the sediments. When there are higher levels of organic matter in a given volume of sediment, more U can be retained. When the proportion of minerogenic sediments increase, the U capacity is diminished. Measurements of TOC and/or loss on ignition (LOI) could help determine the validity of this assumption and to what degree U reflects the organic component. Without this data, using U as a standalone proxy for vegetation derived organic matter is ambiguous. Nevertheless, peak abundances in U coincide with peat facies in both T01 (segment III and II) and T04 (segment II).

5.2.2 Magnetic Susceptibility

High values of magnetic susceptibility usually reflect higher relative abundances of magnetic elements like Fe and Ti (Rothwell and Croudace, 2015). Such a relationship between magnetic susceptibility and Ti and Fe is recognizable in T01 (see section 5.1.2; figure 5.2) but not in T04 (figure 4.7). However, peaks in magnetic susceptibility correlate well with dense (dark; Bouma, 1964; discussed in section 2.3.4) sediments in the x-rays (see figure 4.8; T05, 37cm). As such, there may be a relationship between the magnetic signature of the sediments and minerogenic content and grainsize in the Tranevåg cores (Rothwell and Croudace, 2015). Nevertheless, the variations in magnetic susceptibility are very slight in T01 and T04 making any trends difficult to interpret.

5.2.3 Chlorine and Calcium

Both Ca and Cl in sediments have been used to interpret marine influence (Rothwell and Croudace, 2015; Chagué-Gott et al. 2012) because Cl is a major component of sea salt (Chagué-Gott et al. 2012) and Ca is associated with marine organisms with calcium carbonate shells or tests. Chlorine regularly fluctuates between higher and lower values in core T01, making any trend(s) difficult to interpret (figure 4.3). This may reflect precipitation, with Cl becoming more concentrated in marsh sediments during drier periods, for example, and more dilute during wetter periods. Periodic, large storm events, would have also increased Cl levels periodically at Tranevåg. In T04, the up-core decreasing trend in segments V and VI (i.e. between 100 and 45 cm) suggests a gradual decrease in RSL (inundation), consistent in time with the established sea level curve in Romundset et al. (2015), followed by a relatively stable period in segments III and II (between 45 and 20 cm; figure 4.7). The sharp Cl increase in segment I, core T04 (Up-core from 13 cm; figure 4.7) might then reflect the current period of RSL rise. This increase in Cl concentration, upwards from 13 cm in T04 (figure 4.7), occurs after the installation of the tide gauge in Tregde in AD 1927. As such, the Cl elemental proxy is not compatible in time with tide gauge measurements. We assume that variations in Cl are significantly influenced by discrete events (e.g. storms) and processes of Cl mobilisation (e.g. solution in groundwater). The peak area of Cl upwards from 13cm in T04 might also reflect the storm surge at the time of sampling, overprinting any trend caused by rising RSL in the upper sediment. As such, Cl was not used as a proxy for the onset of RSL rise at Tranevåg.

Statistically significant correlation between Ca and Cl in T01 (table 4.2) suggests the same source (e.g. tidal currents), however, there is no such correlation in T04 (table 4.3). With no local sources of Ca in bedrock, likely also none from the small till blanket above Tranevåg (see section 2.4.4; figure 2.10), the source of the Ca may be biogenic, derived from marine organisms, and might serve as a marine proxy. Because no calcareous foraminifera were identified during counting (see section 4.3.3), Ca does not reflect calcareous foraminifera abundances in T01 or T04. However, fluctuations in Ca might originate from dissolution of Ca (e.g. calcareous forminifera) due to low pH (Edwards and Wright, 2015; Concheyro et al., 2014) or dilution by terrigenous material (Rothwell and Croudace, 2015). As is, the Ca elemental profiles are assumed to be distorted by dissolution or dilution of Ca, making any trends difficult to interpret, and was not used to determine when the transition from RSL fall to rise occurred.

5.3 Foraminiferal Analysis

To extract RSL information from preserved foraminiferal assemblages, modern vertical distribution patterns of foraminifera spp. can be used under the assumption that the distribution pattern has not changed over time (Edwards and Wright, 2015). This thesis does not include sampling and analysis of the modern vertical distribution of foraminifera in the studied marsh. As such, more general observations of the vertical distribution of specific species in the Skagerakk and Kattegatt straights by Alve and Murray (1999) and general comments on the common vertical distribution of cosmopolitan species of foraminifera in salt marshes in Edwards and Wright (2015) were used to analyse the data from Tranevåg.

Species diversity in all cores from Tranevåg was low, which is expected in marginal marine (brackish) environments (Alve and Murray, 1999). An up-core trend of decreasing species diversity was observed in core T01 (table 4.2; 3-4 species observed in sediments above 90 cm; 5-6 species observed in subsamples below 140cm), which is consistent with the observation by Alve and Murray (1999) that species diversity generally decreases with elevation above MSL. It can therefore be argued that increased diversity downcore is indicative of increasingly marine environments, which is in agreement with the local sea level history of gradually falling RSL for the past ~1500 years, published by Romundset et al. (2015).

If linings are excluded from the assemblages, the up-core transition from *M. fusca*- to *J. macrescens*-dominated assemblages correlates with the vegetational zone change from unvegetated low tidal flats where *M. fusca* dominates (Alve and Murray, 1999; Edwards and Wright, 2015) to vegetated mid/high tidal flats at 69cm depth in core T01 (i.e. from segment IV to III). The up-core transition from *M. fusca*-dominated assemblages to *J. macrescens*-dominated assemblages at from (below) 90 cm to (above) 60cm depth in T01 demonstrates that RSL was still falling in 519 +-22 BP.

Foraminiferal assemblages are heavily dominated by *J. macrescens* in the uppermost core samples in T01 (60 to 1 cm), and likely indicate elevations within the upper quarter of the tidal range (Edwards and Wright, 2015). This is in agreement with the observation made by Alve and Murray (1999) that *J. macrescens* dominates the landward areas of marshes in Skagerakk and Kattegatt. Alve and Murray (1999) also observed that abundances of *J. macrescens* was highest on decaying leaves from *C. acuta* (a sedge species) and, it therefore seems likely that the abundance of *J. macrescens* in Tranevåg is tied to the vegetation species in the upper saltmarsh and reedswamp. Moreover, maximum abundances of *T. Inflata* at 40 and 60 cm (table 4.2) are also generally indicative of the upper quarter of the tidal range (Edwards and Wright, 2015). As such, the up-core increasing trend of *J. macrescens* and *T. inflata* suggets that RSL was falling from 90 cm towards the core top, and species assemblages do not appear to have responded to the current trend of increasing RSL (as determined from the tide gauge record at Tregde). As mentioned earlier in section 4.3.3, a number of individuals of foraminifera may actually be *B. pseudomacrescens,* but were counted as *J. macrescens* because of difficulties with differentiating these species. If tests from *B. pseudomacrescens* are indeed present in core T01, identification and counting of them (i.e. differentiation between *J. macrescens and B. pseudomacrescens*) might help reveal more subtle RSL trends in the youngest (highest) sediments, becaue they are vertically restricted to less brackish enviornments than *J. macrescens* and *T. inflata* (Alve and Murray, 1999).

The high numbers of organic test linings between 160 and 200 cm in core T01 are assumed to originate from the agglutinated salt marsh species *T. comprimata* (>40%; table 4.3), and could indicate a specific height above mean high water, as has been observed in North American salt marshes by Gehrels (1994). Observations from North American marshes do not necessarily extrapolate well to southern Norway, however. Nevertheless, the distribution of *T. comprimata* is closely tied to the distribution of associated plants and have been observed by Alve and Murray (1999) in marshes inhabited by *zoestera, phragmites, carex* and *Salicornia* plants species. However, without knowledge of the modern distribution of *T. comprimata* and what plants this species favours in Tranevåg, the distribution of *T. comprimata* has little indicative value in relation to RSL.

Alternatively, assemblages comprising of *M. fusca* and calcareous foraminiferal spp. are common in transitional zones in the lowest marsh fringe (Edwards and Wright, 2015), and the 1-2m core represents a more marine environment than the 0-1 m core at T01. If the organic linings interpreted as *T. comprimata* between 140 and 200cm are actually linings from a calcareous spp., like *R. anomala*, which shares morphological similarities, they would indicate a near or fully subtidal environment. This hypothesis is plausible, however, the presence of *J. macrescens, T. Inflata*, unidentified agglutinated foraminifera type 1 and 2, and the presence of testate amoeba at 180 cm and 200 cm (Table 4.2), suggests a brackish and vegetated intertidal environment rather than a subtidal environment (Edwards and Wright, 2015). Therefore, this hypothesis was discarded as it is unlikely that *R. anomala,* a mostly subtidal species (Alve and Murray, 1999), makes up more then 40% of the assemblage together with intertidal indicators such as agglutinated foraminifera. Even so, this does not refute the possibility that *J. macrescens* and *T. Inflata* individuals have been transported seaward on leaf debris/algae and that the unidentified agglutinated species are tolerant of near subtidal conditions. Whether indicative or the upper tidal range or near subtidal environments, the abundance of the *T. comprimata* linings do demonstrate a different environment below 160 cm depth in core T01 compared to the sediments above 160 cm, and considering the abundance of *M. fusca* below 90 cm depth, it is a fair assumption that the *T. comprimata* linings represent a more saline environment than *J. macrescens.*

In relation to the research question, the up-core transition from *M. fusca*- to *J. macrescens*-dominated foraminiferal assemblages between 90 and 60 cm does provide evidence that sea level was still falling approximately 519 +-22 years BP. After this transition, increasing abundances of *J. macrescens* and *T. Inflata* suggest a trend of falling RSL. Rising RSL as measured by the tide gauge in Tregde is not reflected in the foraminiferal dataset presented in this thesis.

5.4 Vegetation Zones of Sediments

Vegetation zones in the Tranevåg salt marsh cores, T01 and T04 were assessed within core segments, which were determined based on significant changes in properties such as colour, structures visible in the X-rays and visible organic content (see section 4.2, 4.3, 4.4). To determine when RSL began rising, prior to that indicated by the Tregde tide gauge (AD 1927), the vegetation zones of each segment in T01, T04 and T05 were identified (see below sections: 5.3.1, 5.3.2, 5.3.3), as well as their RSL tendency in relation to the segment below. The following interpretations assume that changes in colour and visible organic matter reflect changes in the vegetation as a response to changes in RSL, and that palaeo-vegetation zones identified in the core sediments have a similar relationship to contemporaneous MSL compared to the modern marsh vegetation zones (see section4.6). For instance, the colour of the sediment reflects, in part, the pigments provided to the sediments from the *in situ* plant life (Deshpande et al., 2014), while visible organic matter, particularly roots, indicate some of the *in situ* plant life at the time of deposition (Vis et al., 2015).

Without direct grain size and total organic carbon measurements (not undertaken due to costs, availability of equipment, and waiting time for analyses), visual classification of sediment into categories like silty-clay vs. clayey-silt is not possible, however organic matter content vs minerogenic content can be estimated to some degree by colour. Water content and grain size of the minerogenic component also determines colour, with drier sediments appearing lighter in colour than wet sediments, and silts and sands being usually lighter in colour than clays, for example.

5.4.1 Core T01

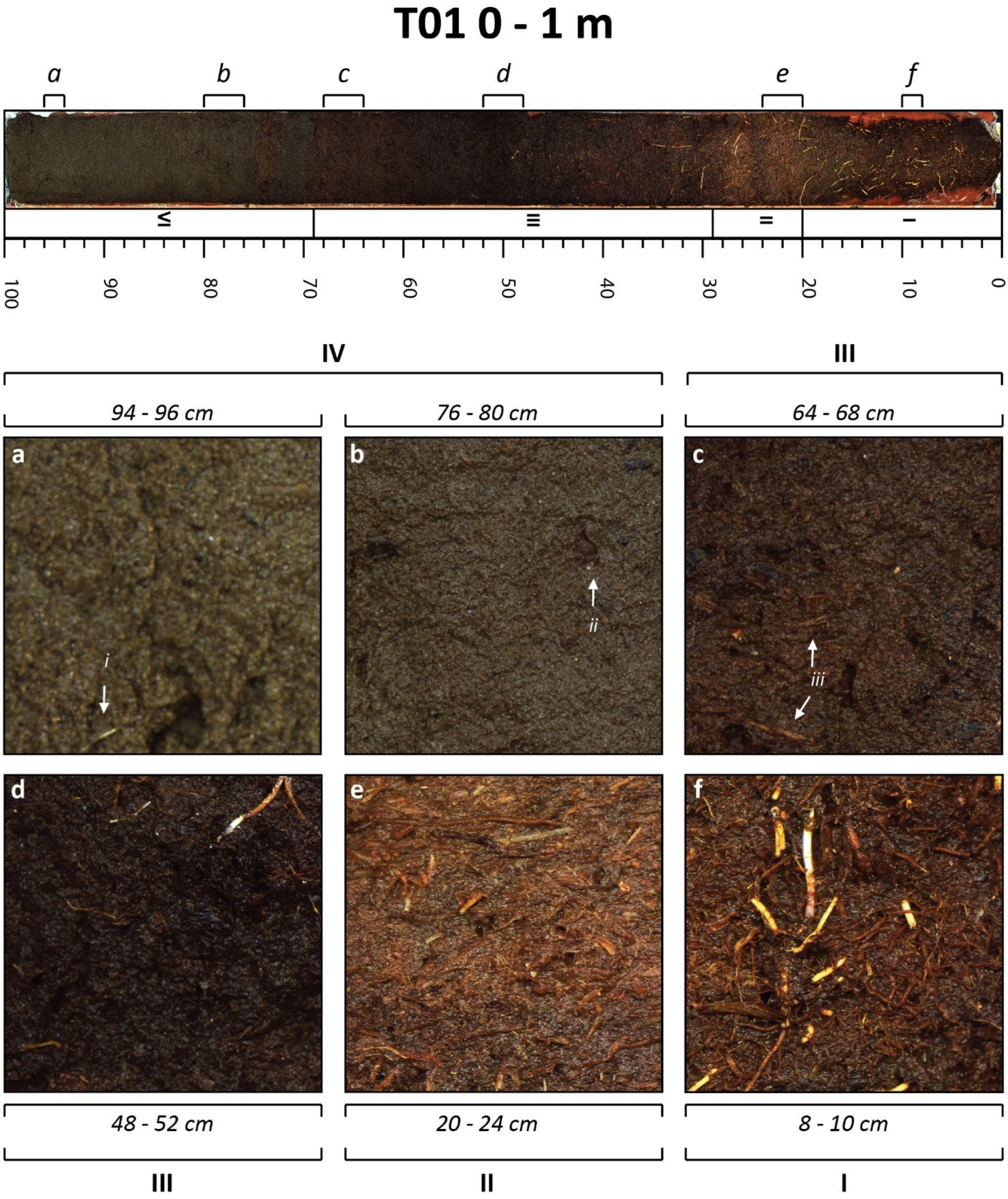

Figure 5.3 Close ups of sediments from T01 core segments. The photos are brightened using adobe Photoshop to make features more visible. a, b) segment IV, salt marsh environment: i, ii) organic fragments that might be roots. c, d) segment III, salt marsh environment: iii) Visible roots. e) segment II, reedswamp environment. f) segment I, salt marsh environment.

In T01, segment IV (68-100 cm; approximate age of sediment: >520 years BP; figure 5.3: a, b) is interpreted as originating from a salt marsh environment, as opposed to a mudflat environment, due to the presence of agglutinated foraminiferal species *J. macrescens* (table 4.2: 90 cm), which is vertically restricted to vegetated intertidal environments (Edwards and Wright, 2015). The dark brown colour of the sediment, suggests high organic matter content, and the sparse, but visible organic fragments that may be *in situ* roots (Figure 5.3; i and ii), suggest a vegetated environment. Mudflat sediments would likely have calcareous foraminifera in the assemblages, a higher minerogenic content which would be reflected in the colour of the sediment, and no roots (Edwards and Wright, 2015; Vis et al., 2015).

Segment III, core T01 (69 - 29 cm; 109 to 520 years BP; figure 5.3: c) is interpreted as peat originating from the salt marsh vegetational platform because of the visible roots amongst other organic matter (Figure 5.3; iii, iv), the dark greyish vermillion colour that suggests a high organic content, and the mottled appearance of the segment in the X-ray. Within segment III, root fragments generally increase in size and abundance up-core (figure 5.3; c compared to d). Decomposition of organic matter appears less complete than in segment IV. This might be a feature of time and/or reflect a change in the environment that affects decomposition. As mentioned in section 5.3, the transition between segment IV and III (69cm) coincides with an up-core transition in the foraminiferal assemblages from being dominated by *M. fusca* to *J. macrescens* (figure 4.5), suggesting a transition from the marsh fringe toward the higher marsh and thus falling RSL (discussed in section 5.4).

Segment II (29 – 20 cm; 78 to 109 years BP; figure 5.3: e) is also interpreted as peat because of its densely packed roots and plant detritus, but from a different vegetational environment than segment III. Segment II is interpreted as reflecting a change in vegetation causing a colour change to a moderate tangelo (i.e. different pigments from the vegetation; Deshpande et al., 2014) and the change in the visible organic matter, which is generally more densely packed and vertically aligned (figure 5.3: e). This might reflect a gradational change in decomposition downcore that is a feature of time, however, the return to darker colours in segment I makes an environmental change seem more likely. Based on the vegetation zonation observed in the field (see section 4.6), segment II reflects the transition from the salt marsh up into the higher reedswamp zone, therefore indicating a falling RSL tendency.

Segment I (0 – 20 cm; Modern to 78 years BP: figure 5.3, f) includes the sediment surface in the present-day salt marsh vegetational zone. Segment I therefore indicates a transition from the seaward reedswamp zone back to the salt marsh vegetational platform, and thus indicates that RSL is now rising. We assume that, excluding segment II, the sediments from the core top downwards towards the transition from segments IV to III at 69 cm, are sediments from the same general saltmarsh environment, and that the down-core differences in colour and visible organic matter reflects the degree of decomposition as a feature of time.

Table 5.4 Core segments in T01, vegetation zones, and RSL trend

T01	Depth in core (cm)	Age	Vegetation Zone	RSL Trend
I	0 - 20 cm	Modern to 78 years BP	Salt marsh	RSL rising
II	20 - 29 cm	78 to 109 years BP	Reedswamp	RSL falling
III	29 - 69 cm	109 to 520 years BP	Salt marsh	RSL falling
IV	69 - 100 cm	>520 years BP	Salt marsh	-

In T01, segments IV, III and II reflect a transition from the salt marsh fringe to a reedswamp environment, in response to a gradual fall in RSL between 770 and 110 years BP (approximate dates for 82 and 29cm, respectively; figure 5.2; table 4.1). The transition to a reedswamp environment occurred approximately 110 BP. Segment I is interpreted as originating from an environment with higher RSL than segment II and therefore suggests that RSL has been rising for at least the past 78 years (date for 20 cm, figure 5.2).

5.4.2 Core T04

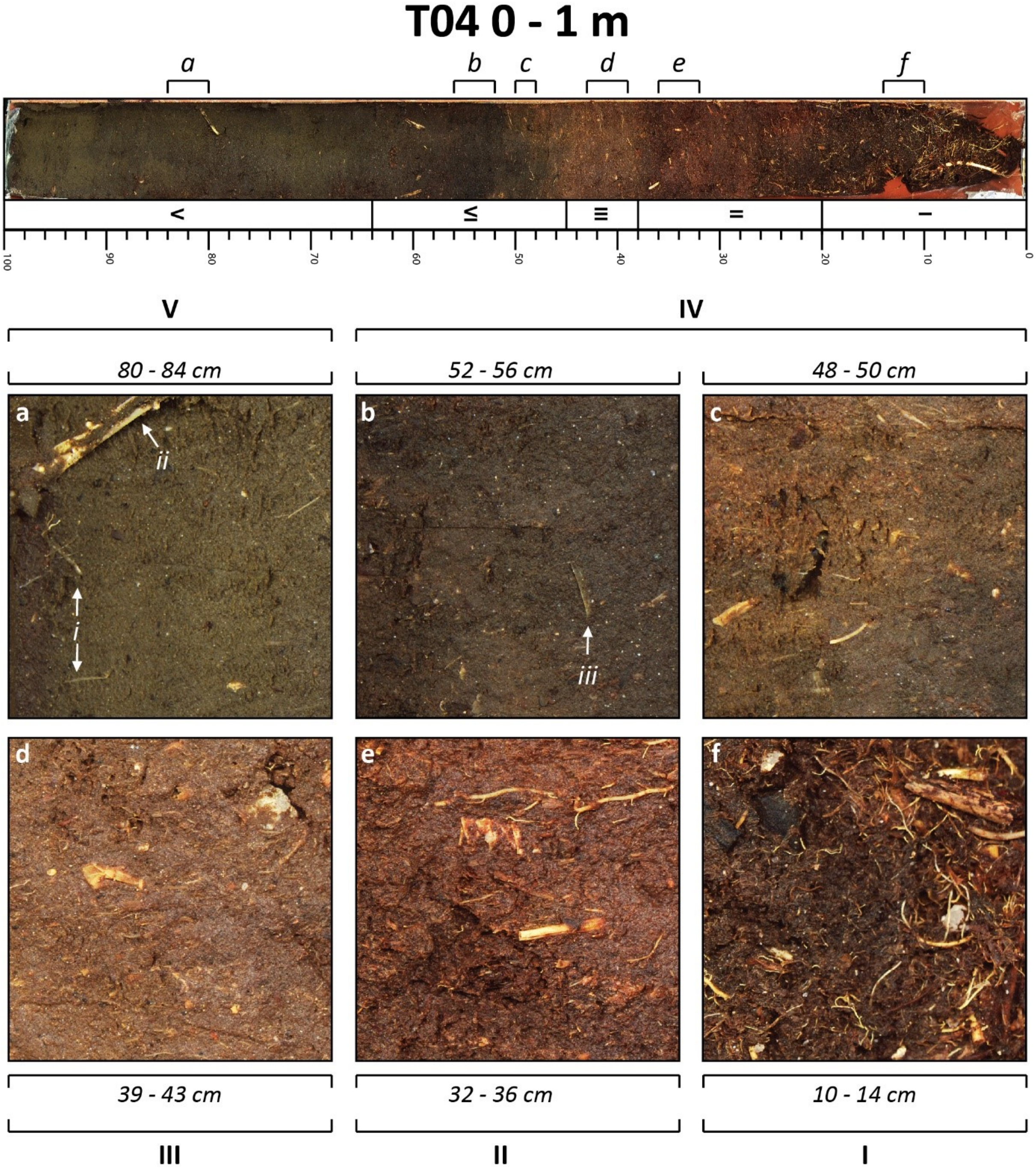

Figure 5.4 Close ups of sediments from core T04. The photos are brightened using adobe Photoshop to make features more visible. a) segment V, salt marsh environment: i) small preserved roots. ii) allochthonous reed detritus. b, c) segment IV, salt marsh environment: iii) small preserved roots. d) segment III: reedswamp environment. e) segment II, reedswamp environment. f) segment I, reedswamp environment.

In T04, Segment V (64 – 100 cm; >2110 years BP; fiure 5.4: a) is interpreted as originating from a vegetated salt marsh environment because the small preserved roots in the sediments (figure 5.4: i) and agglutinated foraminiferal species (see section

4.3.3), both suggest a formerly vegetated environment. Detritus from reeds in this segment (figure 5.4: ii) are likely allochthonous.

Segment IV (45 – 64 cm; >1350 to ca. 2110 years BP; figure 5.4: b, c) is also interpreted as originating from a vegetated salt marsh environment because of the visible roots (figure 5.3; b) and agglutinated foraminifera species (see section 4.3.3). The up-core darkening in colour (Figure 5.4; b compared to a) might reflect an increase in organic content, water content and/or might be related to redox conditions as suggested by the synchronous peaks of Fe and S between 41 and 47cm and 47 to 51 cm (Rothwell and Croudace, 2015; figure 4.4). The up-core increase of visible organic matter in segment IV as compared to that in segment V (figure 5.4: b compared to a) might reflect the degree of decomposition as a function of time. The colour change from a very dark greyish tangelo at 54 cm to a (brighter) dark tangelo between 51 and 45 (figure 5.4; c compared to b) cm is interpreted as bioturbation by the vegetation that grew at the sediment surface in segment III because the dark tangelo colour and fibrous appearance of the sediment is similar to segment III (figure 5.4; c compared to d). Considering the age of the sediments in segment V and IV (>2110 years BP and >1350 to ca. 2110 years BP, respectively; table 5.5), they were deposited in a period of established RSL fall (Romundset et al., 2015).

Segment III (38 – 45 cm; ca. 960 to ca. 1350 years BP; figure 5.4: d) is interpreted as originating from a different vegetational environment than segment IV and V. Compared to the below segments, the visible organic matter in segment III appears more abundant and fragments appear to be generally larger (figure 5.4; d compared to a, b, c). Additionally, the change to a moderate tangelo colour might reflect a change in vegetation (Deshpande et al., 2014). Due to the age of the sediments in segment III (ca. 960 to ca. 1350 years BP; shortly after the last geological evidence of falling RSL in the sea level curve from Romundset et al. (2015) it seems fair to assume that these were deposited in a period of falling RSL. As such, segment III is interpreted as reflecting a vertical transition upwards into the seaward reedswamp dominated by low growing reed species (see section 4.6), and thereby an up-core trend of falling RSL.

Segment II (20 – 38 cm; 135 to ca. 960; figure 5.4: e) is interpreted as originating from a different vegetational zone that segment III. The change in colour to a dark vermillion might reflect a change in vegetation, the sediment appears more fibrous, and the visible organic matter appears more abundant and fragments generally larger than is segment III (figure 5.4; e compared to d), suggesting a different depositional environment. These three differences between segment II and III might reflect different degrees of decomposition as a feature of time. However, because of the transition between segment III and II appears as relatively abrupt, segment II is interpreted as reflecting a transition into the reedswamp dominated by *P. australis*. As such, segment II suggests an up-core trend of falling RSL.

Segment I (20 – 0 cm; modern to 135 years BP; figure 5.4: f) includes the sediment surface in the present-day *P. australis* dominated reedswamp. Most of this segment was deposited during the past 92 years of measured RSL rise at the Tregde tide gauge (Romundset et al., 2015). Therefore, the increased density, coarser texture and browner colour (dark tangelo) of the sediments that differentiate segment I from segment II (figure 5.4: f compared to e) are assumed to reflect a change in the environment due to rising RSL (see section 5.2.4), and not a change in vegetational zone. As such, segment I indicates that RSL is now rising.

Table 5.5 Core segments in T04, vegetation zones, and RSL trend

T04	Depth in core (cm)	Age	Vegetation Zone	RSL Trend
I	0 – 20 cm	modern to 135 years BP	Reed Swamp supratidal	RSL rise
II	20 – 38 cm	135 to ca. 960	Reed swamp; supratidal	RSL fall
III	38 – 45 cm	ca. 960 to ca. 1350 years BP	Reed swamp supratidal	RSL fall
IV	45 – 64 cm	>1350 to ca. 2110 years BP	Salt marsh; Intertidal	RSL fall
V	64 – 100 cm	>2110 years BP	Salt marsh intertidal	-

In T04, segments V and IV reflect a period of known RSL fall, as they predate the isolation of two proximal (6 and 6.5km distant) basins described in Romundset et al. (2015), that were isolated from the sea between 1530-1370 years BP and 1720-1560 / 1810-1610 years BP, respectively (Romundset et al., 2015). Segments V, IV, III and II suggest a transition from the salt marsh vegetational platform to the *P. australis* dominated reedswamp environment, suggesting a gradual up-core fall in RSL between >2110 years BP and 134 years BP (approximate dates for 59 and 20 cm, respectively). Segment I is interpreted as originating from the same vegetation zone as segment II, but have been impacted by slowly rising RSL because the top 18 cm of segment I dates to a period of measured RSL rise, as recorded by the Tregde tide gauge (Romundset et al., 2015). Therefore, it seems reasonable to assume that segment I indicates a period of rising RSL for the past ca. 135 years (approximate date for 20cm).

5.4.3 Core T05

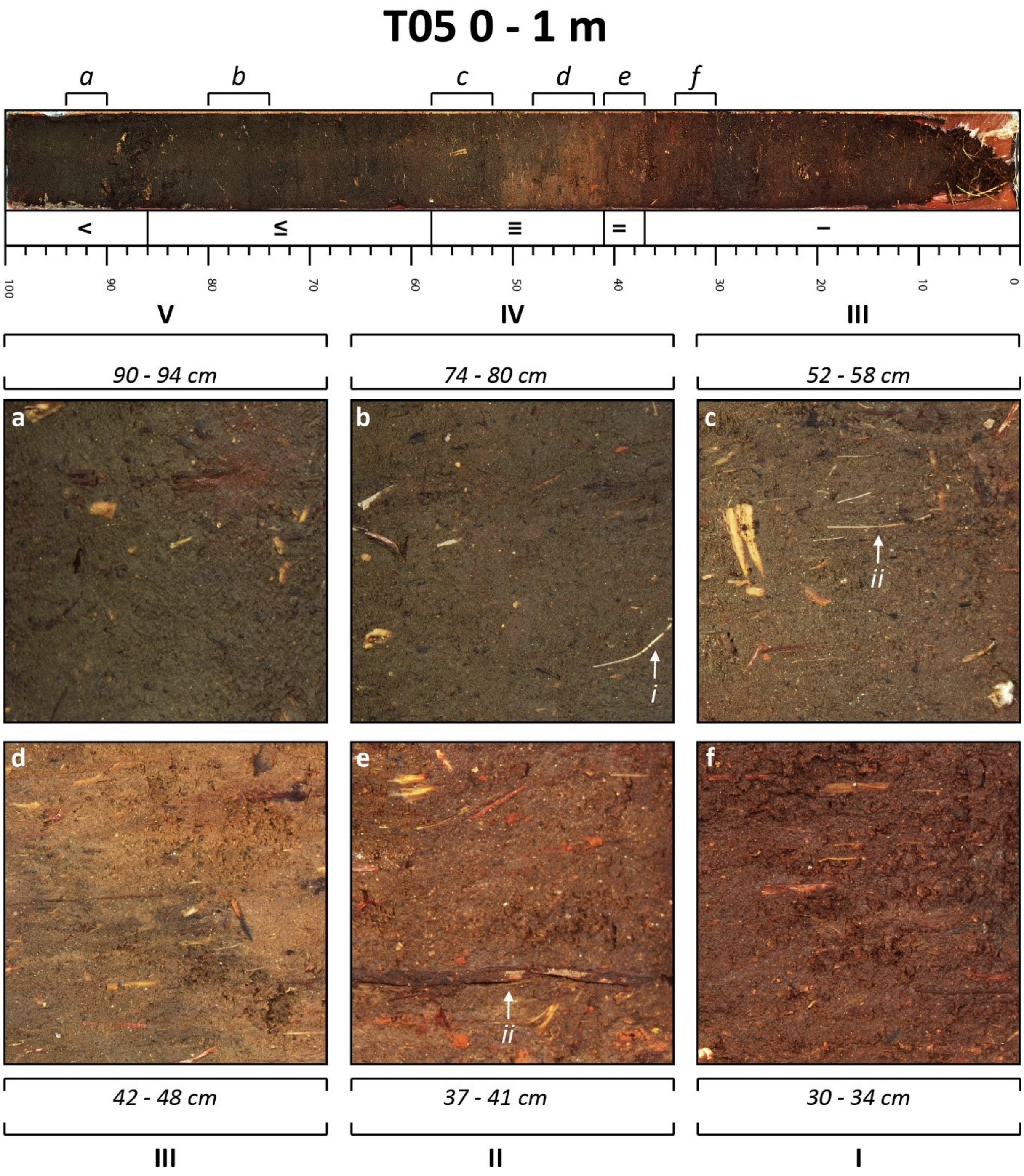

Figure 5.5 Close ups of sediments from core T05. The photos are brightened using adobe Photoshop to make features more visible. a) segment V, salt marsh environment. b) segment IV, salt marsh environment: i) small preserved root. c, d) segment III, salt marsh environment: ii) small preserved root. e) segment II, reedswamp environment: large preserved root. f) segment I, reedswamp environment.

In T05, Segment V (86 – 100 cm; dated to 4762 years BP at 95 cm: figure 5.5: a) is dated to 4762 years BP at 95 cm, a time when RSL was ~4m higher than at present (Romundset et al., 2015). A such, this segment should represent a marine environment, however, the agglutinated foraminifera found in this segment (see section 4.3.3) suggests an intertidal vegetated environment. This discrepancy is unexpected, and likely due to some unforeseen error. For instance, the radiocarbon date from this depth is from a piece of bark, which may be significantly older than the contemporaneous sediment at the time of deposition (e.g. driftwood). Moreover, tests from calcareous foraminifera may have dissolved in the low pH environment of marsh sediments (Concheyro et al., 2014), and some agglutinated foraminifera species can be found in near subtidal environments (Alve and Murray, 1999). The sediment includes many preserved organic fragments (figure 5.5: a), however, no roots are identifiable. This may be due to decomposition of roots over time.

Segment IV (58 – 86 cm; figure 5.5: b) is interpreted as originating from a vegetated salt marsh environment because small preserved roots are visible (figure 5.5; i). These are likely autochthons (Waller, 2015). As such, Segment IV indicates falling RSL.

Segment III (41 – 58 cm; figure 5.5: c, d) is also interpreted as originating from a vegetated salt marsh environment because of the visible roots (figure 5.5 ii). Compared to segment IV, the sediments in segment III are somewhat denser in the x-ray (figure 4.2) and brighter in colour (figure 5.5: c compared to b), suggesting a higher minerogenic fraction. The sediment between 41 and 50 cm is interpreted as having experienced bioturbated by the vegetation that grew at the sediment surface in segment II because the moderate tangelo colour and more fibrous appearance of the sediment is similar to segment II (figure 5.5; d compared to c).

Segment II (37 – 41 cm; figure 5.5: e) is interpreted as originating from a different vegetational environment than segment V, IV and III. Compared to the below segments, sediments in segment III appear more fibrous and visible roots are generally larger (figure 5.5: e compared to a, b, c). Additionally, the change to a dark tangelo colour might reflect a change in vegetation (Deshpande et al., 2014). Based on the observed vegetational zones in the marsh (see section 4.6), segment II is interpreted as reflecting a vertical transition upwards into the seaward reedswamp zone that is dominated by low-growing reed species, and therefore suggests an up-core trend of falling RSL.

Segment I (0 – 37 cm; figure 5.5: f) includes the sediment surface at the upland edge of the *P. australis* dominated reedswamp, and the sediments of this segment are interpreted as originating from that environment. The change in colour to a dark vermillion (figure 5.5: f compared to e) is assumed to reflect a transition from the seaward reedswamp, dominated by low growing species, to the reedswamp dominated by *P. australis,* as well as the rhizomes, appearing as white ovals in the x-ray (figure 4.2), which is a common feature of sediments from *P. australis* dominated environments

(Vis et al., 2015). The transition from segment II to I, up core, suggests a trend of falling RSL at this time.

Table 5.6 Core segments in T05, vegetation zones, and RSL trend

T05	Depth in core (cm)	Age	Vegetation Zone	RSL Trend
I	0 – 37 cm		Reed Swamp landward	RSL fall
II	37 – 41 cm		Reed swamp; seaward	RSL fall
III	41 – 58 cm		Salt marsh; High tidal flats	RSL fall
IV	58 – 86 cm		Salt marsh	RSL fall
V	86 – 100 cm	4762 BP	Salt marsh	-

In T05, segment V is dated to 4762 years BP at 95 cm depth. Above this, all segments in T05 show a transition from a salt marsh environment to the upper boundary of the *P. australis* reedswamp, which correlates to a gradual fall in RSL since ca. 4760 years BP. The measured RSL rise of the past 92 years as recorded by the tide gauge in Tregde (Romundset et al., 2015) is not reflected in the data presented in this thesis for core T05.

5.5 Multi-proxy Evidence for the Beginning RSL Rise at Tranevåg

Based on our interpretation of changing vegetation zones in sediment cores T01 and T04 (figures 5.3, 5.4; tables 5.4, 5.5) it appears that vegetation at Tranevåg responded to a switch from falling to rising RSL ca. 87 years BP at the seaward edge of the marsh (core T01) and ca. 135 years BP in the middle of the reedswamp (core T04). Such a time lag in vegetation response to low rates of RSL rise between the more seaward and inland parts of the marsh is unsurprising given their difference in elevation (T01 at 12 cm asl vs. T04 at 31.5 cm asl vs. T05 at 52 cm asl).

Increasing rates of salt marsh accretion are another common response of salt marsh systems to rising RSL (Kirwan and Megonigal, 2013; Crosby et al., 2016; Müller-Navarra 2019). In core T01, marsh accretion rates increased from ca. 0.89 mm/yr to 1.21 mm/yr, approximately 160 years BP according to our age model (38 cm down core; fig. 5,1, table 5.1), and continued to accelerate up core (table 5.1), up to 3.08 mm/yr. At the same time in T04 (ca. 160 years BP), accretion rates jumped from 0.19 mm/yr to 1.21 mm/yr (23 cm core depth; Fig. 5.1, Table 5.2).

Accelerating rates of salt marsh accretion in T01 and T04 around 160 years ago are coincident with sharply increasing Ti and decreasing U trends observed in the XRF data (figures 5.6, 5.7). The statistically significant anticorrelation between U and Ti (table 4.5, 4.6) in both T01 and T04 suggests that there is an inverse relationship between the influx of terrigenous material and U sorption capacity in Tranevåg sediments. Increasing Ti and decreasing U may therefore indicate that the more rapid rates of saltmarsh accretion in T01 and T04 correlate to a higher fraction of inorganic (minerogenic) sediment input, resulting in a relative lowering of U sorption capacity.

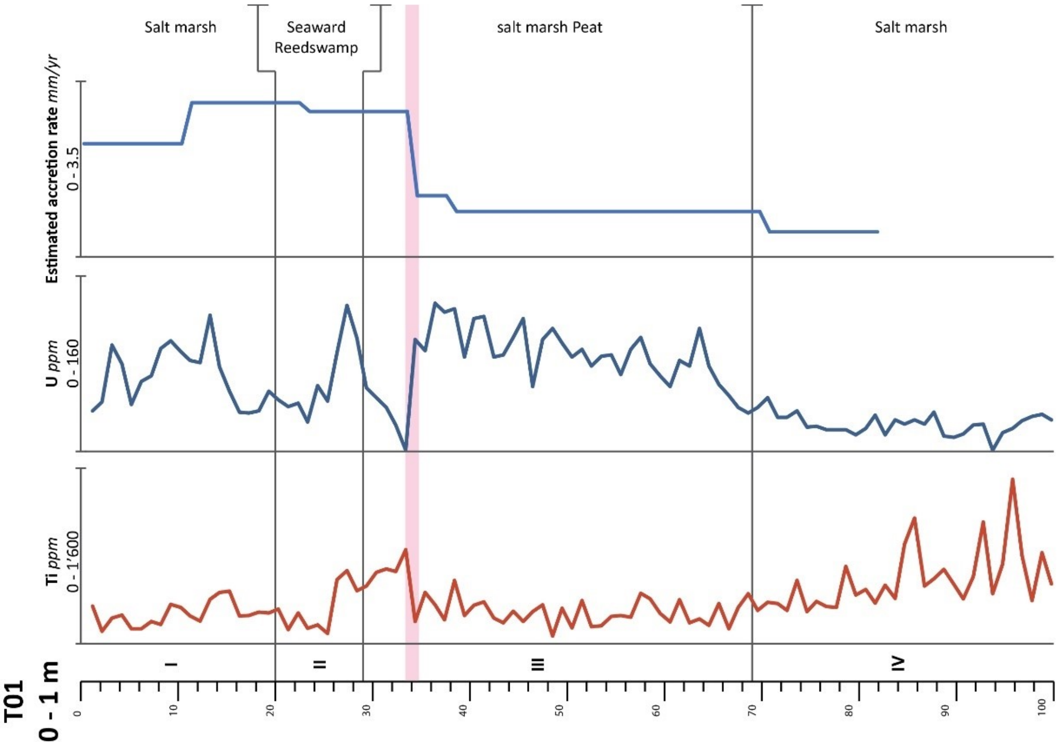

Figure 5.6 Core T01, U, Ti, and accretion rate data. Uranium shows an overall, up-core increasing trend from the base of the core (100 cm), upwards to 34 cm, at which point it falls sharply to 0 ppm. At the same time (ca. 126 years BP), both Ti concentrations and accretion rates increase rapidly (highlighted by pink line). Above 34 cm, U fluctuates between higher and lower values all the way to the core top (i.e. to present day), with a peak of 133 ppm at 28 cm core depth.

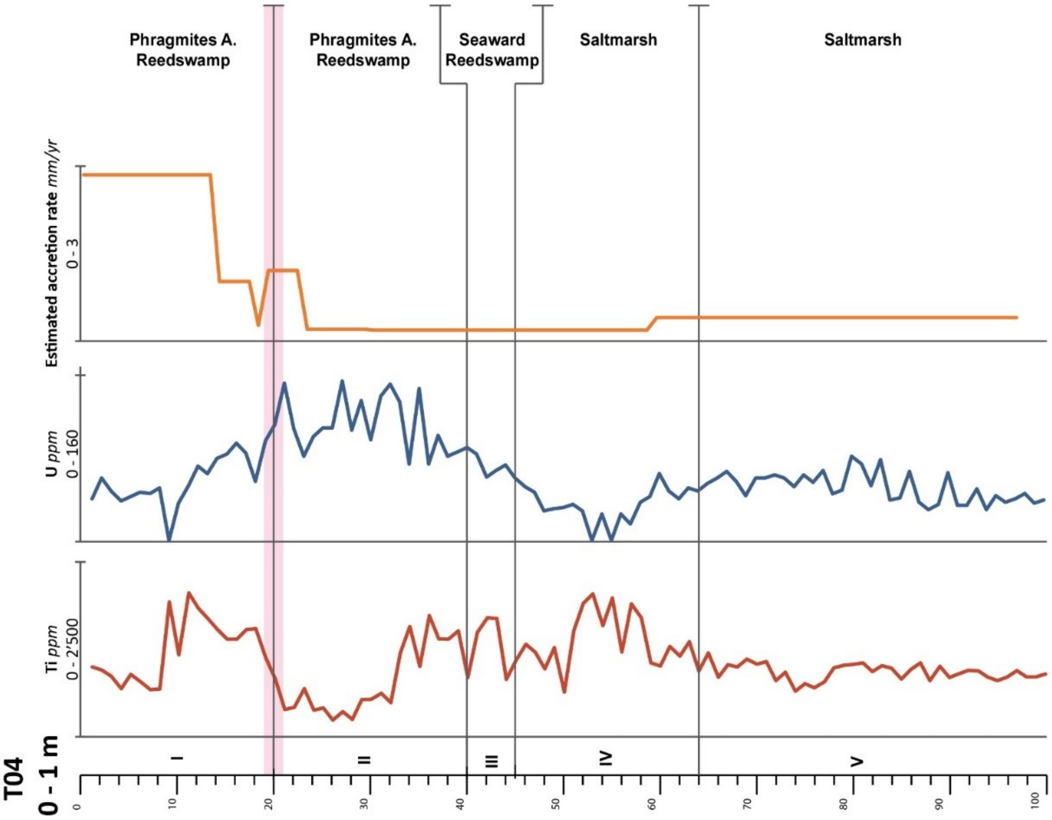

Figure 5.7 Core T04, U, Ti, and accretion rate data. Uranium concentrations in T04 begin to increase at ca. 55 cm, culminating at 140 ppm at 34 cm core depth, remaining high with peaks ranging from 140 to 150 ppm up wards to 21 cm, which coincides with the phragmites peat vegetation zone (segment II). Peak U concentrations are coincident with a major decrease in Ti concentrations at ca. 32 cm. At 21 cm core depth, U decreases and Ti increases, as marsh accretion rates increase (highlighted by pink line).

If the response of Tranevåg saltmarsh to the onset of rising RSL sometime prior to 1927 AD (92 years BP; i.e. the year of tide gauge installation) was to keep pace by increasing rates of accretion, then the accretion rates calculated using Pb measurements suggest this began around 160 years BP (1858 AD). Which is generally compatible with the increased Ti and decreased U in the sediments during the same interval, and with the vegetation zone data (figures 5.3, 5.4, table 5.4, 5.5). Assuming that the sharp decreases in U and sharp increases in Ti in T01 (34 cm) and T04 (21cm), reflect the onset of increasing accretion rates, this date is adjusted to 126 years BP in T01 (1877AD) and 142 years BP in T04 (1893 AD), averaged to 1885 AD.

One factor worth considering that may have impacted marsh accretion rates is related to historical land use change in form of harvesting of the reedswamp. Changes in hinterland land use are known to affect minerogenic sedimentation (e.g. McGregor et al., 2009). At Tranevåg, the harvesting of vegetation could reduce its sediment trapping potential and enhance surface wash erosion in the upper areas and deposition in the lower areas. Nevertheless, there are no clear indications that RSL was rising prior to 160 years BP. Therefore, if the increases in accretion rate do reflect land use change rather than RSL increase, they serve as a maximum age of the current transgression. Following, the age range where the beginning of the current transgression occurred is narrowed to 42 years, between 1885 AD to the beginning of measurements at the Tregde tide gauge in 1927 AD.

Chapter 6 Conclusions and Recommendations

By the end of the 21st century, the highest projected rates of RSL rise, following RCP 8.5, might approach or exceed ~10mm/yr for most of the Norwegian coast due to melting of the ice sheets (Richter et al., 2012; Simpson et al., 2015). Detailed knowledge of future sea-level rise in Norway, including how it will vary across space and time, and how it will manifest itself at the coast, is crucial for land-use planning, coastal management, and informing the general public (Simpson et al., 2015).

In Norway, long-term trends in RSL are mainly a function of GIA and changes in GMSL. Most of Norway still experiences rates of vertical uplift due to GIA that match or exceed rates of GMSL rise. However, in coastal areas that experienced less ice loading during the late Weichselian and Younger Dryas, rates of GMSL are higher than rates of GIA causing these coastal sites to experience RSL rise (Simpson et al., 2015; Fjeldskaar & Amantov, 2018).

The geological evidence of Holocene RSL change in the southernmost region of Norway demonstrate a trend of falling RSL for the past ~7000 years (Romundset et al., 2015). However, the instrumental record from the tide gauge at Tregde show an accelerating trend of RSL rise for this region since installation in 1927 AD, amounting to an average rate of 0.4 mm/a between 1927 and 2010, and 1.4 mm/a between 1980 and 2010. This recent record of RSL rise is not reflected in the established sea level curves for the area (e.g. Romundset et al., 2015). The ~1400 year gap between the youngest established geological evidence of falling RSL and the measured RSL rise at Tregde defines the uncertainty this thesis seeks to address.

The sedimentary record of the Tranevåg saltmarsh extends back to the Younger dryas, reflecting inundation during the Tapes transgression approximately 9,500 years BP, followed by a trend of falling RSL until recent times. Foraminiferal data presented in this thesis from the upper 2 m of the sedimentary record demonstrate that RSL was still falling 519 ±22 cal. years BP, but does not reflect the recent period of RSL rise.

Increased accretion rates, caused by increasing minerogenic sediment input, is a common response of salt marsh systems to rising RSL (Kirwan and Megonigal, 2013; Crosby et al., 2016; Müller-Navarra 2019). In our cores, statistically significant anticorrelation between U and Ti suggest that there is an inverse relationship between the influx of minerogenic material and the U sorption capacity of the sediment (Rothwell and Croudace, 2015; Brown et al., 2000; Ahmad, 2015). This correlates well with increasing accretion rates calculated using radiocarbon dates and variations in atmospheric Pb concentrations as chronomarkers (Rizzo et al., 2009), and is compatible with vegetation zone data (Waller, 2015). Based on increasing minerogenic sediment influx and decreasing U sorption capacity of the sediments, as indicated by Ti and U consentrations in our cores, we conclude that RSL in Tranevåg transitioned from falling/standstill to rising approximately 134 years ago in 1885 AD.

Our foraminiferal counts show that the Tranevåg marsh can be used for foraminifera based sea level research in line with the principles outlined by Edward and wright (2015). There are significant changes in the foraminiferal assemblages over time in the sedimentary record, here attributed to falling RSL since the Tapes transgression. Consequently, a correlation between vertical zonation of species and RSL is evident. Provided a good modern analog of foraminiferal vertical distribution patterns and reliable identification of organic linings, the number of foraminifera and long undisturbed sedimentary, makes the Tranevåg marsh promising in terms of foraminifera based RSL reconstruction and, considering the rarity of long saltmarsh records in southern Norway, this salt marsh might be the best option. Nevertheless, anthropogenic influence might have disturbed the uppermost assemblages in the sedimentary record. Therefore, it may be beneficial to extract a modern analogue of present-day vertical zonation of foraminifera from an undisturbed proximal marsh, if possible.

Our pre-screening shows several depths where layers of cryptotephra may be present in the upper meter of the sedimentary record, which appear to be compatible with the record of islandic eruptions. The next step is to confirm that the peaks in the elemental abundances and magnetic susceptibility do indeed reflect the presence of cryptotephra layers, by separating glass shards from the surrounding matrix. Geochemical analysis of the glass shards and comparison to the geochemical profiles of the volcanic eruptions, to be used as chronomarkers (Kylander et al., 2012), appears promising and would improve the core chronology and consequently the accuracy of the calculated accretion rates used here to determine the onset of the current trend of rising RSL.

7. References

Ahmad, M. (2015). Immobilization of uranium as a function of peat content (Master's thesis, Norwegian University of Life Sciences, Ås).

Alve, E., & Murray, J. W. (1999). Marginal marine environments of the Skagerrak and Kattegat: a baseline study of living (stained) benthic foraminiferal ecology. Palaeogeography, Palaeoclimatology, Palaeoecology, 146(1-4), 171-193.

Alve, E., & Murray, J. W. (2001). Temporal variability in vertical distributions of live (stained) intertidal foraminifera, southern England. The Journal of Foraminiferal Research, 31(1), 12 24.

Andersen, B. G. (1960). Sørlandet i sen-og postglacial tid. Aschehoug [in Komm.].

Artsdatabanken (2019) Artskart. Retrieved from: https://artskart.artsdatabanken.no Last accessed at: 23.09.2019

Banks, D., Reimann, C., & Skarphagen, H. (1998). The comparative hydrochemistry of two granitic island aquifers: the Isles of Scilly, UK and the Hvaler Islands, Norway. Science of the total environment, 209(2-3), 169-183.

Barnett, R. L., Newton, T. L., Charman, D. J., & Gehrels, W. R. (2017). Salt-marsh testate amoebae as precise and widespread indicators of sea-level change. Earth-science reviews, 164, 193-207.

Benn, D., & Evans, D. J. (2010). Glaciers and glaciation, Second edition. Routledge.

Berthelsen, B. O., Steinnes, E., Solberg, W., & Jingsen, L. (1995). Heavy metal concentrations in plants in relation to atmospheric heavy metal deposition. Journal of Environmental Quality, 24(5), 1018-1026.

Bouma, A. H. (1964). Notes on X-ray interpretation of marine sediments. Marine geology, 2(4), 278 309.

Brown, P. A., Gill, S. A., & Allen, S. J. (2000). Metal removal from wastewater using peat. Water research, 34(16), 3907-3916.

Camacho, S. G., de Jesus Moura, D. M., Connor, S., Scott, D. B., & Boski, T. (2015). Taxonomy, ecology and biogeographical trends of dominant benthic foraminifera species from an Atlantic Mediterranean estuary (the Guadiana, southeast Portugal). Palaeontologia Electronica, 18(1), 1-27.

Chagué-Goff, C., Andrew, A., Szczuciński, W., Goff, J., & Nishimura, Y. (2012). Geochemical signatures up to the maximum inundation of the 2011 Tohoku-oki tsunami—implications for the 869 AD Jogan and other palaeotsunamis. Sedimentary Geology, 282, 65-77.

Charman, D. J. (2015). Testate amoebae In I. shennan, A. J. Long, B. P. Horton(Ed.), Handbook of Sea Leven Research (pp. 3 - 25). John Wiley & Sons.

Charrieau, L. M., Bryngemark, L., Hansson, I., & Filipsson, H. L. (2018). Improved wet splitter for micropalaeontological analysis, and assessment of uncertainty using data from splitters. Journal of Micropalaeontology, 37(1), 191-194.

Church, J. A., Clark, P. U., Cazenave, A., Gregory, J. M., Jevrejeva, S., Levermann, A., ... & Payne, A. J. (2013). Sea level change. PM Cambridge University Press.

Concheyro, A., Caramés, A., Amenábar, C. R., & Lescano, M. (2014). Nannofossils, foraminifera and microforaminiferal linings in the Cenozoic diamictites of Cape Lamb, Vega Island, Antarctica. Polish Polar Research, 35(1), 1-26.

Crosby, S. C., Sax, D. F., Palmer, M. E., Booth, H. S., Deegan, L. A., Bertness, M. D., & Leslie, H. M. (2016). Salt marsh persistence is threatened by predicted sea-level rise. Estuarine, Coastal and Shelf Science, 181, 93-99.

Croudace, I. W., Romano, E., Ausili, A., Bergamin, L., & Rothwell, R. G. (2015). X-ray core scanners as an environmental forensics tool: a case study of polluted harbour sediment (Augusta Bay, Sicily). In Micro-XRF studies of sediment cores (pp. 393-421). Springer, Dordrecht.

Cushman, J. A., & Brönnimann, P. (1948). Some new genera and species of foraminifera from brackish water of Trinidad. Contributions from the Cushman Laboratory for Foraminiferal Research, 24(1), 37-42.

Denecke, M. A., Janssens, K., Proost, K., Rothe, J., & Noseck, U. (2005). Confocal micrometer-scale X ray fluorescence and X-ray absorption fine structure studies of uranium speciation in a tertiary sediment from a waste disposal natural analogue site. Environmental science & technology, 39(7), 2049-2058.

Deshpande, B. N., Tremblay, R., Pienitz, R., & Vincent, W. F. (2014). Sedimentary pigments as indicators of cyanobacterial dynamics in a hypereutrophic lake. Journal of paleolimnology, 52(3), 171-184.

Edwards, R and Wright, A. (2015). Foraminifera In I. shennan, A. J. Long, B. P. Horton(Ed.), Handbook of Sea-Leven Research (pp. 3 - 25). John Wiley & Sons.

Fjeldskaar, W., & Amantov, A. (2018). Younger Dryas transgression in western Norway: a modelling approach. Norwegian Journal of Geology, 98(1), 127-139.

Fjeldskaar, W., Lindholm, C., Dehls, J. F., & Fjeldskaar, I. (2000). Postglacial uplift, neotectonics and seismicity in Fennoscandia. Quaternary Science Reviews, 19(14-15), 1413-1422.

Forbes, D. L. (2011). State of the Arctic coast 2010: scientific review and outlook. Land Ocean Interactions in the Coastal Zone, Institute of Coastal Research.

Fægri, K. (1940). Quartärgeologische Untersuchungen im westlichen Norwegen. II. Zur spätquartären Geschichte Järens. Bergens Mus. Årb. 1939–40. Nat.-vit. rekke, 7, 202.

Fægri, K. (1944). Studies on the Pleistocene of Western Norway. III Bømlo.–Bergen Museum Årbok 1943. Bergen: Naturvitenskapelig rekkes, 100.

Gehrels, W. R. (1994). Determining relative sea-level change from salt-marsh foraminifera and plant zones on the coast of Maine, USA. Journal of Coastal Research, 990-1009.

Glooschenko, W. A., & Capobianco, J. A. (1982). Trace element content of northern Ontario peat. Environmental Science & Technology, 16(3), 187-188.

Haflidason, H., Eiriksson, J., & Kreveld, S. V. (2000). The tephrochronology of Iceland and the North Atlantic region during the Middle and Late Quaternary: a review. Journal of Quaternary Science: Published for the Quaternary Research Association, 15(1), 3-22.

Hamblin, W. K. (1962). X-ray radiography in the study of structures in homogeneous sediments. Journal of Sedimentary Research, 32(2), 201-210.

Hanebuth, T. J., & Lantzsch, H. (2008). A Late Quaternary sedimentary shelf system under hyperarid conditions: unravelling climatic, oceanographic and sea-level controls (Golfe d'Arguin, Mauritania, NW Africa). Marine Geology, 256(1-4), 77-89.

Haug, G. H., Hughen, K. A., Sigman, D. M., Peterson, L. C., & Röhl, U. (2001). Southward migration of the intertropical convergence zone through the Holocene. Science, 293(5533), 1304-1308.

Hayward, B. W., & Brook, F. J. (1994). Foraminiferal paleoecology and initial subsidence of the early Miocene Waitemata Basin, Waiheke Island, Auckland. New Zealand Journal of Geology and Geophysics, 37(1), 11-24.

Holm-Nilsen, S., Wergeland, P. (2018, September 22). «Knud» slo ut nødnettet: – Det er en skandale. Norsk Rikskringkastning (NRK), Retrieved 18.082019 from: https://www.nrk.no/norge/_knud_-slo-ut-nodnettet_-_-det-er-en-skandale-1.14219126.
Holmboe, J. 1909: En undersjøisk torvmyr ved Nordhassel paa Lister. Naturen 33, 235–243.

Holden, J. (Ed.). (2012). An introduction to physical geography and the environment, Third edition. Pearson Education.

Holmboe, J. (1909). En undersjoisk torvmyr ved Nordhassel paa Lister. éditeur non identifié.

Høeg, H. I. 1995: Pollenanalyse – Lista. In Ballin, T. B. & Lass Jensen, O. (eds.): Report. Farsundprosjektet – Steinalderbopladser på Lista (in Norwegian), 268–323. Universitetets Oldsaksamling, Varia 29.

Kartverket (Se havnivå) (2018, September 22). Se Havnivå: Østre Tranevåg (Vest-Agder). Retrieved from: https://www.kartverket.no/en/sehavniva Last accessed 12.08.2019

Kartverket (InnlandsGIS) (2019a). Skyggerelieff 25cm NHM. Retrieved from: https://geocortex3.innlandsgis.no Last accessed: 19.08.2019

Kartverket (2019b). Liknes-Farsund-Lyngdal 1966. Retrieved from: https://www.norgeibilder.no Last accessed: 19.08.2019

Kartverket (2019c). Farsund 2009. Retrieved from: https://www.norgeibilder.no Last accessed: 19.08.2019

Kartverket (InnlandsGIS) (2019d). Bakgrunnskart; farger. Retrieved from: https://geocortex3.innlandsgis.no Last accessed: 30.08.2019

Kemp, A. C., Horton, B. P., Culver, S. J., Corbett, D. R., van de Plassche, O., Gehrels, W. R., ... & Parnell, A. C. (2009). Timing and magnitude of recent accelerated sea-level rise (North Carolina, United States). Geology, 37(11), 1035-1038.

Kierulf, H. P., Ouassou, M., Simpson, M. J. R., & Vestøl, O. (2013). A continuous velocity field for Norway. Journal of Geodesy, 87(4), 337-349.

Kirwan, M. L., Guntenspergen, G. R., d'Alpaos, A., Morris, J. T., Mudd, S. M., & Temmerman, S. (2010). Limits on the adaptability of coastal marshes to rising sea level. Geophysical research letters, 37(23).

Kirwan, M. L., & Megonigal, J. P. (2013). Tidal wetland stability in the face of human impacts and sea level rise. Nature, 504(7478), 53.

Kylander, M. E., Lind, E. M., Wastegård, S., & Löwemark, L. (2012). Recommendations for using XRF core scanning as a tool in tephrochronology. The Holocene, 22(3), 371-375.

Marshall, W. (2015). Chronohorizons: Indirect and unique event dating methods for sea-level reconstructions In I. shennan, A. J. Long, B. P. Horton(Ed.), Handbook of Sea-Leven Research (pp. 3 - 25). John Wiley & Sons.

Mayhew, S. (2015) Oxford Dictionary of Geography, fifth edition. Oxford; Oxford University Press.

McConnell, J. R., & Edwards, R. (2008). Coal burning leaves toxic heavy metal legacy in the Arctic. Proceedings of the National Academy of Sciences, 105(34), 12140-12144.

McGregor, H. V., Dupont, L., Stuut, J. B. W., & Kuhlmann, H. (2009). Vegetation change, goats, and religion: a 2000-year history of land use in southern Morocco. Quaternary Science Reviews, 28(15-16), 1434-1448.

Müller-Navarra, K., Milker, Y., Bunzel, D., Lindhorst, S., Friedrich, J., Arz, H., & Schmiedl, G. (2019). Evolution of a salt marsh in the southeastern North Sea region–Anthropogenic and natural forcing. Estuarine, Coastal and Shelf Science, 218, 268-277.

Nixon, F. C., Reinhardt, E. G., & Rothaus, R. (2009). Foraminifera and tidal notches: dating neotectonic events at Korphos, Greece. Marine Geology, 257(1-4), 41-53.

Okuno, J. I., Nakada, M., Ishii, M., & Miura, H. (2014). Vertical tectonic crustal movements along the Japanese coastlines inferred from late Quaternary and recent relative sea-level changes. Quaternary Science Reviews, 91, 42-61.

Overpeck, J. T., Otto-Bliesner, B. L., Miller, G. H., Muhs, D. R., Alley, R. B., & Kiehl, J. T. (2006). Paleoclimatic evidence for future ice-sheet instability and rapid sea-level rise. Science, 311(5768), 1747-1750.

Pakarinen, P., Tolonen, K., & Soveri, J. (1980, August). Distribution of trace metals and sulfur in the surface peat of Finnish raised bogs. In Proceedings of the 6th International Peat Congress (pp. 645-648).

Prøsch-Danielsen, L. (1997). New light on the Holocene shore displacement curve on Lista, the southernmost part of Norway.

Prøsch-Danielsen, L. (2006). Sea level studies along the coast of of southwestern Norway. With emphasise on three short-lived Holocene marine events. Arkeologisk museum i Stavanger.

Richter, K., Nilsen, J. E., & Drange, H. (2012). Contributions to sea level variability along the Norwegian coast for 1960–2010. Journal of Geophysical Research: Oceans, 117(C5).

Riveiros, N. V., & Patterson, R. T. (2007a). An illustrated guide to fjord foraminifera from the Seymour-Belize Inlet Complex, northern British Columbia, Canada. Palaeontol Electronica, 11(1), 1-45.

Riveiros, N. V., Babalola, A. O., Boudreau, R. E., Patterson, R. T., Roe, H. M., & Doherty, C. (2007b). Modern distribution of salt marsh foraminifera and thecamoebians in the Seymour–Belize Inlet Complex, British Columbia, Canada. Marine Geology, 242(1-3), 39-63.

Rizzo, S., Basile, S., Caruso, A., Cosentino, C., Tranchina, L., & Brai, M. (2009). Dating of a sediment core by 210 Pb ex method and Pb pollution chronology in the Palermo Gulf (Italy). Water, air, and soil pollution, 202(1-4), 109-120.

Romundset, A., Fredin, O., & Høgaas, F. (2015). AH olocene sea-level curve and revised isobase map based on isolation basins from near the southern tip of N orway. Boreas, 44(2), 383-400.

Rothwell, R. G. and Croudace, I. W. (2015). Twenty years of XRF core scanning marine sediments: what do geochemical proxies tell us?. In Micro-XRF Studies of Sediment Cores (pp. 25-102). Springer, Dordrecht.

Ryen, H. T., Landvik, J. Y. & Jakobsen, L. V. 2009: Multiple Holocene transgressions at Lista, Southern Norway, reconstructed from ground penetrating radar and stratigraphic studies. Norwegian Geological Winter Meeting 2009, Abstracts and Proceedings, 87–88, Geological Society of Norway, Oslo.

Schuerch, M., Vafeidis, A., Slawig, T., & Temmerman, S. (2013). Modeling the influence of changing storm patterns on the ability of a salt marsh to keep pace with sea level rise. Journal of Geophysical Research: Earth Surface, 118(1), 84-96.

Schwartz, M. L.(editor), Kelletat, D., & Scheffers, A. (2005). Europe, coastal geomorphology. In Encyclopedia of Coastal Science (pp. 452-462). Springer Netherlands.

Scott, D. S., & Medioli, F. S. (1978). Vertical zonations of marsh foraminifera as accurate indicators of former sea-levels. Nature, 272(5653), 528.

Selbekk, R. S., & Trønnes, R. G. (2007). The 1362 AD Öræfajökull eruption, Iceland: Petrology and geochemistry of large-volume homogeneous rhyolite. Journal of Volcanology and Geothermal Research, 160(1-2), 42-58.

shennan, I. (2015). Handbook of sea-level research: framing research questions In I. shennan, A. J. Long, B. P. Horton(Ed.), Handbook of Sea-Leven Research (pp. 3 - 25). John Wiley & Sons.

Shvartsev, S. L. (2008). Geochemistry of fresh groundwater in the main landscape zones of the Earth. Geochemistry International, 46(13), 1285.

Simpson, M., Breili, K., Kierulf, H. P., Lysaker, D., Ouassou, M., & Haug, E. (2012). Estimates of future sea-level changes for Norway. In Technical Report of the Norwegian Mapping Authority.

Simpson, M. J., Nilsen, J. E. Ø., Ravndal, O. R., Breili, K., Sande, H., Kierulf, H. P., ... & Vestøl, O. (2015). Sea Level Change for Norway: Past and Present Observations and Projections to 2100. Norwegian Centre for Climate Services report, 1, 2015.

Sluijs, A., Röhl, U., Schouten, S., Brumsack, H. J., Sangiorgi, F., Damsté, J. S. S., & Brinkhuis, H. (2008). Arctic late Paleocene–early Eocene paleoenvironments with special emphasis on the Paleocene-Eocene thermal maximum (Lomonosov Ridge, Integrated Ocean Drilling Program Expedition 302). Paleoceanography, 23(1).

Sollesnes, A. F., & Fægri, K. (1951). Pollenanalytisk undersøkelse av to avleiringer fra Norges sydvestlige kyst. Blyttia, 9(2), 41-58.

Steinnes, E., Allen, R. O., Petersen, H. M., Rambæk, J. P., & Varskog, P. (1997). Evidence of large scale heavy-metal contamination of natural surface soils in Norway from long-range atmospheric transport. Science of the Total Environment, 205(2-3), 255-266.

Steinnes, E., Solberg, W., Petersen, H. M., & Wren, C. D. (1989). Heavy metal pollution by long range atmospheric transport in natural soils of Southern Norway. Water, Air, and Soil Pollution, 45(3-4), 207-218.

Stuiver, M., Reimer, P.J., and Reimer, R.W., 2019, CALIB 7.1 [WWW program] at http://calib.org, accessed 2019-7-15

Svendsen, J. I., & Mangerud, J. (1987). Late Weichselian and Holocene sea-level history for a cross section of western Norway. Journal of Quaternary Science, 2(2), 113-132.

Sørensen, R., Bakkelid, S., & Torp, B. (1987). Land Uplift Nasjonalatlas for Norge. Statens kartverk.

Vis, G. J., Cohen, K. M., Westerhoff, W. E., Ten Veen, J. H., Hijma, M. P., Van, A. J. F. & Vos, P. C (2015). Paleogeography In I. shennan, A. J. Long, B. P. Horton(Ed.), Handbook of Sea-Leven Research (pp. 3 - 25). John Wiley & Sons.

VORREN, T. O., VORREN, K. D., ALM, T., GULLIKSEN, S., & LØVLIE, R. (1988). The last deglaciation (20,000 to 11,000 BP) on Andoya, Northern Norway. Boreas, 17(1), 41-77.

Wahl, T., Haigh, I. D., Woodworth, P. L., Albrecht, F., Dillingh, D., Jensen, J., ... & Wöppelmann, G. (2013). Observed mean sea level changes around the North Sea coastline from 1800 to present. Earth-Science Reviews, 124, 51-67

Waller, M. (2015). Techniques and applications of plant macrofossil analysis in sea-level studies In I. shennan, A. J. Long, B. P. Horton(Ed.), Handbook of Sea-Leven Research (pp. 3 - 25). John Wiley & Sons.

8. Appendices

Appendix 1 Notes on Uranium Supply to The Tranevåg Marsh

Appendix 2 X-ray fluorescence measurements for T01 and T04

Appendix 3 High-Resolution RGP Photographs and Magnetic susceptibility measurements of T01 5-7m

Appendix 1

Notes on Uranium Supply to The Tranevåg Marsh

The assumption that U is supplied continuously the the studied marsh of this thesis is based on published papers by Shavartsev (2008) and Banks et al. (1988), as outlined here.

Shvartsev (2008) compiled a global dataset to compare groundwater chemistry from different climatic regions. Average geochemistry in groundwater samples from wetlands, mixed forests and southern taigas in temperate humid climates all showed the presence of uranium with concentrations of 0.1 µg/l, 0.57 µg/l and 0.31 µg/l, respectively. Although specific sites were not mentioned, concentrations of uranium were present in data from temperate humid locations in Sweden (0.12 µg/l) and Finland (0.46 µg/l). Samples from the Norwegian mountains had very high concentrations (2.5 µg/l) (Shavartsev, 2008).

Shavatsev (2008) also compares the geochemistry different types of groundwater to rivers and seawater. In his data, seawater had an average uranium concentration of 3.3 µg/l, 2.52 orders of magnitude higher than the average groundwater concentrations. Concentrations of uranium in rivers (presented as two categories by Shavatsev, 2008) were very low (avg. 0.004 µg/l), not present or below the detection limit of the measurement instruments used (Shavartsev, 2008).

Earlier, in 1988, Banks et al. compared the geochemistry of groundwater derived from boreholes in seemingly similar granitic islands of Hvaler and the Scilly islands. Based on their results, they argue that the differences in the groundwaters geochemistry isn’t merely determined by the lithology, but also a range of other factors such as the hydrodynamic, geographical, biological and anthropogenic, and that these factors create a complex interplay (Banks et al., 1988).

They also argue that weathering histories have a considerable effect on the groundwater geochemistry. Among others, a longer weathering history might cause a depletion of uranium in the unsaturated zone and zone of active groundwater flow. The younger age of the bedrock surface at Hvaler, that was scoured by glacier ice as recently as the younger dryas, gives a shorter weathering history compared to the similar location on The Scilly islands and is used as a possible explanation for the higher concentrations of uranium in the local groundwater. These concentrations were at least one order of magnitude higher in Hvaler than in The Scilly islands (Banks et al., 1988).

Based on the observations of Shvartsev (2008) and Banks et al. (1988) it seems reasonable to assume that bot sea and groundwater have relatively high consentrations of solved U, resulting in a continuous supply of U to the studied saltmarsh.

Appendix 2

X-ray fluorescence measurements T01

Table A2.1 X-ray fluorescence measurements in T01 0 – 1 m section.

Depth	Si	SiO2	P	P2O5	S	S	Cl	K	K2O	Ca	CaO	Ti	TiO2	Mn	MnO
cm	Ppm	Wt%	Ppm	Wt%	Ppm	Wt%	Ppm	Ppm	Wt%	Ppm	Wt%	Ppm	Wt%	Ppm	Wt%
1	92787.5	19.9	300	0.07	17065	1.7	16258	4362	0.53	6842	0.96	342	0.06	72	0.01
2	32761.1	7.0	300	0.07	16963	1.7	101821	3247	0.39	6087	0.85	113	0.02	27	0.003
3	83275.6	17.8	300	0.07	15038	1.5	20082	3109	0.37	7529	1.05	235	0.04	36	0.005
4	104673.3	22.4	300	0.07	16329	1.6	26704	4010	0.48	7034	0.98	259	0.04	46	0.006
5	89527.1	19.2	300	0.07	18695	1.9	88535	3028	0.36	6620	0.93	137	0.02	22	0.003
6	65910.2	14.1	300	0.07	19359	1.9	97785	2659	0.32	6354	0.89	137	0.02	19	0.002
7	122910.6	26.3	300	0.07	21374	2.1	56607	2870	0.35	7519	1.05	202	0.03	32	0.004
8	70882.2	15.2	300	0.07	22570	2.3	79366	2728	0.33	7195	1.01	174	0.03	24	0.003
9	103891.4	22.2	300	0.07	19167	1.9	18338	3332	0.40	6640	0.93	359	0.06	36	0.005
10	96975.85	20.7	300	0.07	26991	2.7	55702	3640	0.44	7557	1.06	331	0.06	36	0.005
11	89301.4	19.1	300	0.07	33790	3.4	101427	3126	0.38	7925	1.11	254	0.04	28	0.004
12	73409.3	15.7	300	0.07	43558	4.4	149482	3491	0.42	8528	1.19	206	0.03	24	0.003
13	141367.6	30.2	300	0.07	23212	2.3	49403	4594	0.55	5720	0.80	404	0.07	42	0.005
14	172362.8	36.9	300	0.07	17858	1.8	36256	3831	0.46	5174	0.72	468	0.08	45	0.006
15	173172.8	37.0	300	0.07	22114	2.2	50985	4167	0.50	6006	0.84	478	0.08	44	0.006
16	99139.6	21.2	300	0.07	39180	3.9	86808	2939	0.35	9549	1.34	254	0.04	38	0.005
17	94790.6	20.3	300	0.07	39245	3.9	104468	3154	0.38	8717	1.22	258	0.04	21	0.003
18	112720.1	24.1	300	0.07	35364	3.5	79322	3258	0.39	7807	1.09	287	0.05	34	0.004
19	79574.3	17.0	300	0.07	30863	3.1	73069	3042	0.37	6701	0.94	282	0.05	39	0.005
20	87484.7	18.7	300	0.07	32238	3.2	110084	3849	0.46	6875	0.96	314	0.05	28	0.004
21	58917.8	12.6	300	0.07	34366	3.4	103980	2222	0.27	5809	0.81	128	0.02	20	0.003
22	79644.7	17.0	300	0.07	39015	3.9	108259	3274	0.39	8579	1.20	279	0.05	34	0.004
23	60609.8	13.0	300	0.07	43720	4.4	124000	2611	0.31	8272	1.16	139	0.02	14	0.002
24	84484.3	18.1	300	0.07	35350	3.5	127297	2827	0.34	7118	1.00	170	0.03	30	0.004
25	44587.7	9.5	300	0.07	34924	3.5	125993	1829	0.22	6368	0.89	93	0.02	13	0.002
26	75681.3	16.2	300	0.07	32249	3.2	37663	3955	0.48	6654	0.93	583	0.10	56	0.007
27	85771.5	18.3	300	0.07	32388	3.2	26667	4371	0.53	6764	0.95	666	0.11	67	0.009
28	78811.8	16.9	300	0.07	30141	3.0	30981	3340	0.40	5473	0.77	484	0.08	46	0.006
29	121151.7	25.9	300	0.07	24940	2.5	33081	3725	0.45	4875	0.68	525	0.09	45	0.006
30	115526.7	24.7	300	0.07	31698	3.2	86508	3642	0.44	6844	0.96	652	0.11	42	0.005
31	78996.3	16.9	300	0.07	40075	4.0	95507	3832	0.46	8321	1.16	682	0.11	59	0.008
32	126290	27.0	300	0.07	39602	4.0	64536	5541	0.67	9688	1.36	658	0.11	37	0.005
33	71541.15	15.3	300	0.07	31541	3.2	64031	5006	0.60	7716	1.08	856	0.14	64	0.008
34	38025.85	8.1	300	0.07	48466	4.8	88378	2435	0.29	9324	1.30	203	0.03	18	0.002
35	65912.55	14.1	300	0.07	40114	4.0	57708	3297	0.40	6830	0.96	469	0.08	56	0.007
36	55170	11.8	300	0.07	46327	4.6	50965	3075	0.37	7548	1.06	353	0.06	39	0.005
37	23787.8	5.1	300	0.07	59191	5.9	91202	2659	0.32	9957	1.39	217	0.04	30	0.004

38	67016.6	14.3	300	0.07	42561	4.3	33150	4018	0.48	5508	0.77	578	0.10	58	0.007

Table A2.1 Continued

Depth	Si	SiO2	P	P2O5	S	S	Cl	K	K2O	Ca	CaO	Ti	TiO2	Mn	MnO
cm	Ppm	Wt%	Ppm	Wt%	Ppm	Wt%	Ppm	Ppm	Wt%	Ppm	Wt%	Ppm	Wt%	Ppm	Wt%
39	31243.2	6.7	300	0.07	49467	4.9	107733	2278	0.27	8983	1.26	258	0.04	28	0.004
40	47842.1	10.2	300	0.07	40673	4.1	56501	2839	0.34	6195	0.87	350	0.06	41	0.005
41	52297.55	11.2	300	0.07	46796	4.7	48300	3214	0.39	7491	1.05	381	0.06	51	0.007
42	37057.8	7.9	300	0.07	57375	5.7	93784	2936	0.35	9992	1.40	234	0.04	25	0.003
43	44473.77	9.5	300	0.07	61450	6.1	88865	2360	0.28	8151	1.14	192	0.03	35	0.005
44	47262.9	10.1	300	0.07	46659	4.7	44439	2590	0.31	5536	0.77	296	0.05	38	0.005
45	35125.4	7.5	300	0.07	54872	5.5	61181	2280	0.27	7695	1.08	204	0.03	35	0.005
46	44787.2	9.6	300	0.07	55481	5.5	89326	2905	0.35	7978	1.12	291	0.05	37	0.005
47	52786	11.3	300	0.07	55039	5.5	55128	3117	0.38	7137	1.00	353	0.06	51	0.007
48	13258.4	2.8	300	0.07	57305	5.7	67427	2010	0.24	7464	1.04	72	0.01	15	0.002
49	55183.83	11.8	300	0.07	50970	5.1	50366	2871	0.35	6253	0.87	322	0.05	45	0.006
50	40460	8.7	300	0.07	56242	5.6	89660	2431	0.29	6777	0.95	145	0.02	28	0.004
51	59635.7	12.8	300	0.07	55455	5.5	52417	3341	0.40	8136	1.14	395	0.07	54	0.007
52	41038.7	8.8	300	0.07	57874	5.8	78563	2237	0.27	9248	1.29	154	0.03	24	0.003
53	44007.2	9.4	300	0.07	57933	5.8	72014	2083	0.25	9128	1.28	165	0.03	30	0.004
54	74656.6	16.0	300	0.07	60806	6.1	70095	2820	0.34	7726	1.08	250	0.04	31	0.004
55	64030.4	13.7	300	0.07	58751	5.9	99604	2851	0.34	8704	1.22	255	0.04	34	0.004
56	62356.3	13.3	300	0.07	65711	6.6	89820	2897	0.35	8079	1.13	241	0.04	32	0.004
57	88968.4	19.0	300	0.07	46635	4.7	28417	3395	0.41	5543	0.78	461	0.08	61	0.008
58	92745.6	19.8	300	0.07	44149	4.4	30127	3531	0.43	5560	0.78	408	0.07	54	0.007
59	70815.25	15.1	300	0.07	53561	5.4	58633	2776	0.33	8105	1.13	275	0.05	55	0.007
60	48799.3	10.4	300	0.07	60699	6.1	65166	2194	0.26	9073	1.27	199	0.03	28	0.004
61	68893.4	14.7	300	0.07	51029	5.1	60907	2907	0.35	10225	1.43	401	0.07	39	0.005
62	62174.2	13.3	300	0.07	54491	5.4	82994	2538	0.31	8667	1.21	192	0.03	29	0.004
63	41713.1	8.9	300	0.07	43380	4.3	23510	2238	0.27	6209	0.87	224	0.04	42	0.005
64	30760	6.6	300	0.07	67752	6.8	80218	2711	0.33	11702	1.64	168	0.03	22	0.003
65	78385.2	16.8	300	0.07	48670	4.9	36371	2872	0.35	6866	0.96	366	0.06	51	0.007
66	35729.1	7.6	300	0.07	69558	7.0	74691	2375	0.29	10729	1.50	137	0.02	28	0.004
67	71496.2	15.3	300	0.07	62387	6.2	93411	2809	0.34	13094	1.83	332	0.06	59	0.008
68	99978.1	21.4	300	0.07	52061	5.2	73159	3514	0.42	10606	1.48	457	0.08	63	0.008
69	80523.1	17.2	300	0.07	51586	5.2	117392	3027	0.36	9232	1.29	302	0.05	65	0.008
70	67574.7	14.5	300	0.07	43060	4.3	62459	3349	0.40	8125	1.14	378	0.06	74	0.010
71	106683.2	22.8	300	0.07	48165	4.8	99389	3678	0.44	7290	1.02	364	0.06	67	0.009
72	77175.2	16.5	300	0.07	58975	5.9	85866	3413	0.41	10210	1.43	302	0.05	65	0.008
73	143288.1	30.7	300	0.07	37528	3.8	26630	4949	0.60	6504	0.91	576	0.10	100	0.013
74	80687	17.3	300	0.07	53118	5.3	90980	3516	0.42	10179	1.42	293	0.05	56	0.007
75	97811.4	20.9	300	0.07	52898	5.3	108961	3879	0.47	9655	1.35	385	0.06	76	0.010
76	90775.6	19.4	300	0.07	52679	5.3	127222	4069	0.49	8538	1.19	339	0.06	66	0.009
77	93874.1	20.1	300	0.07	45691	4.6	119108	3401	0.41	8005	1.12	331	0.06	62	0.008
78	110548.9	23.6	300	0.07	44690	4.5	81619	5366	0.65	7631	1.07	706	0.12	97	0.012
79	99503.2	21.3	300	0.07	54814	5.5	83953	3691	0.44	10200	1.43	443	0.07	68	0.009
80	102444.9	21.9	300	0.07	53562	5.4	108658	4380	0.53	9643	1.35	494	0.08	66	0.009

81	95163.9	20.4	300	0.07	54086	5.4	113953	3905	0.47	10054	1.41	369	0.06	72	0.009

Table A2.1 Continued

Depth	Si	SiO2	P	P2O5	S	S	Cl	K	K2O	Ca	CaO	Ti	TiO2	Mn	MnO
cm	Ppm	Wt%	Ppm	Wt%	Ppm	Wt%	Ppm	Ppm	Wt%	Ppm	Wt%	Ppm	Wt%	Ppm	Wt%
82	108084.5	23.1	300	0.07	58732	5.9	101471	5096	0.61	12829	1.80	535	0.09	77	0.010
83	97560.1	20.9	300	0.07	51548	5.2	119005	4008	0.48	8567	1.20	412	0.07	78	0.010
84	162715.3	34.8	300	0.07	36344	3.6	34130	6412	0.77	5487	0.77	909	0.15	122	0.016
85	167878	35.9	300	0.07	35847	3.6	27398	7738	0.93	5736	0.80	1145	0.19	159	0.021
86	107275.4	22.9	300	0.07	51746	5.2	98122	4809	0.58	8541	1.20	526	0.09	78	0.010
87	109859.6	23.5	300	0.07	59584	6.0	121945	5018	0.60	10209	1.43	593	0.10	94	0.012
88	139518.7	29.8	300	0.07	52967	5.3	83161	5260	0.63	11281	1.58	679	0.11	96	0.012
89	91414.3	19.6	300	0.07	62072	6.2	127525	4359	0.53	13235	1.85	541	0.09	92	0.012
90	87086.1	18.6	300	0.07	62160	6.2	117956	4185	0.50	10564	1.48	410	0.07	87	0.011
91	107247.4	22.9	300	0.07	62150	6.2	100466	5077	0.61	12019	1.68	610	0.10	91	0.012
92	154176.9	33.0	300	0.07	38502	3.9	39350	7044	0.85	5876	0.82	1110	0.19	140	0.018
93	79060.8	16.9	300	0.07	63295	6.3	150277	4071	0.49	12182	1.70	454	0.08	94	0.012
94	100207.3	21.4	300	0.07	64187	6.4	119507	5140	0.62	9901	1.39	728	0.12	102	0.013
95	164346.8	35.2	300	0.07	38282	3.8	35189	7880	0.95	5674	0.79	1498	0.25	151	0.019
96	136283.9	29.2	300	0.07	61662	6.2	92950	5902	0.71	10588	1.48	803	0.13	117	0.015
97	114769.5	24.6	300	0.07	54935	5.5	120992	4416	0.53	9613	1.35	393	0.07	87	0.011
98	173465.9	37.1	300	0.07	35272	3.5	46037	6388	0.77	5694	0.80	831	0.14	119	0.015
99	147210.2	31.5	300	0.07	49321	4.9	80438	4558	0.55	8475	1.19	544	0.09	93	0.012

Table A2.1 X-ray fluorescence measurements in T01 0 – 1 m section.

Depth	Fe	Fe2O3T	Cr	Cr2O3	Ag	As	Ba	Bi	Cd	Ce	Co	Cu	Hg	La	Mo
cm	Ppm	Wt%	Ppm	Wt%	Ppm	Ppm	Ppm	Ppm	Ppm	Ppm	Ppm	Ppm	Ppm	Ppm	Ppm
1	15935	2.28	25	0.004	1	44	77	5	1	25	25	29	1	25	21
2	10507	1.50	3	0.000	1	30	97	5	1	25	25	35	1	25	25
3	9599	1.37	21	0.003	1	31	111	5	1	25	25	42	1	25	13
4	7134	1.02	21	0.003	1	38	125	5	1	25	25	33	1	96	18
5	3353	0.48	13	0.002	1	30	25	5	1	25	25	39	1	25	22
6	2621	0.37	13	0.002	1	34	99	5	1	25	25	42	1	25	32
7	8709	1.25	21	0.003	1	43	100	5	1	25	25	36	1	25	32
8	4406	0.63	17	0.002	1	41	90	5	1	25	25	41	1	25	35
9	5382	0.77	28	0.004	1	49	113	5	1	25	25	43	1	25	37
10	5507	0.79	28	0.004	1	40	92	5	1	25	25	44	1	25	33
11	5443	0.78	20	0.003	1	45	78	5	1	25	25	47	9	25	40
12	9989	1.43	15	0.002	1	70	70	5	1	25	25	40	1	25	43
13	7214	1.03	31	0.005	1	56	103	5	1	25	25	32	12	25	19
14	6775	0.97	34	0.005	1	54	96	5	1	25	25	33	1	25	24
15	6320	0.90	35	0.005	1	46	81	5	1	25	25	29	1	25	21
16	4943	0.71	18	0.003	1	42	150	5	1	25	25	20	6	25	22
17	5962	0.85	15	0.002	1	58	116	5	1	25	25	17	1	25	23
18	4490	0.64	17	0.002	1	27	95	5	1	25	25	20	1	25	27
19	9481	1.36	17	0.002	1	55	73	5	1	25	25	20	1	25	18
20	8719	1.25	18	0.003	1	54	90	5	1	25	25	20	1	25	15
21	5238	0.75	8	0.001	1	18	87	5	1	73	25	3	1	25	27
24	4047	0.58	14	0.002	1	28	79	5	1	25	25	3	1	66	22
25	2199	0.31	10	0.001	1	17	77	5	1	25	25	3	1	25	26
26	6678	0.95	61	0.009	1	35	92	5	1	123	25	22	1	25	33
27	5600	0.80	56	0.008	1	35	60	5	1	106	25	21	1	25	37
28	3561	0.51	47	0.007	1	35	75	5	1	134	25	24	1	25	43
29	4371	0.62	32	0.005	1	33	78	5	1	25	25	26	1	25	45
30	4865	0.70	18	0.003	1	32	108	5	1	25	25	23	1	25	39
31	4759	0.68	17	0.002	1	19	134	5	1	25	25	23	1	25	43
32	4529	0.65	18	0.003	1	43	243	5	1	98	25	15	1	25	44
33	5109	0.73	24	0.003	1	33	279	5	1	25	25	29	1	25	47
34	2597	0.37	13	0.002	1	32	76	5	1	25	25	21	1	25	94
35	5468	0.78	34	0.005	1	18	69	5	1	25	25	23	1	25	70
36	6647	0.95	36	0.005	1	27	64	5	1	62	25	27	1	49	100
37	18286	2.61	21	0.003	1	36	75	5	1	90	25	24	1	25	152
38	38678	5.53	51	0.007	1	44	25	5	1	124	25	31	1	25	147
39	16168	2.31	20	0.003	1	23	74	5	1	111	179	14	1	25	121
40	3538	0.51	34	0.005	1	17	50	5	1	110	25	20	1	25	93
41	21557	3.08	42	0.006	1	32	65	5	1	25	131	27	1	25	99
42	4081	0.58	20	0.003	1	18	79	5	1	25	120	20	1	69	105
43	13172	1.88	18	0.003	1	38	50	5	1	92	132	20	1	25	230
44	21113	3.02	35	0.005	1	21	64	5	1	60	25	17	1	25	112
45	7153	1.02	25	0.004	1	18	54	5	1	176	25	23	1	25	139

Table A2.1 Continued

Depth	Fe	Fe2O3T	Cr	Cr2O3	Ag	As	Ba	Bi	Cd	Ce	Co	Cu	Hg	La	Mo
cm	Ppm	Wt%	Ppm	Wt%	Ppm	Ppm	Ppm	Ppm	Ppm	Ppm	Ppm	Ppm	Ppm	Ppm	Ppm
46	7962	1.14	24	0.004	1	16	64	5	1	116	25	17	1	25	117
47	13712	1.96	32	0.005	1	22	60	5	1	25	25	26	1	25	133
48	3005	0.43	19	0.003	1	19	25	5	1	102	85	3	1	25	71
49	9721	1.39	36	0.005	1	21	71	5	1	79	25	19	1	25	109
50	8546	1.22	20	0.003	1	19	76	5	1	132	25	3	1	76	134
51	10876	1.55	37	0.005	1	16	61	5	1	107	25	17	1	46	105
52	5775	0.83	19	0.003	1	14	48	5	1	115	25	3	1	61	105
53	7110	1.02	19	0.003	1	13	25	5	1	25	25	15	1	67	94
54	12505	1.79	26	0.004	1	14	63	5	1	132	25	16	1	25	69
55	8945	1.28	26	0.004	1	11	60	5	1	86	25	3	1	25	73
56	14549	2.08	23	0.003	1	16	66	5	1	25	25	3	1	100	73
57	15284	2.19	53	0.008	1	24	66	5	1	96	25	17	1	25	91
58	12551	1.79	42	0.006	1	16	76	5	1	135	25	14	1	25	84
59	11490	1.64	28	0.004	1	13	56	5	1	82	25	8	1	47	83
60	7180	1.03	19	0.003	1	8	25	5	1	25	25	3	1	25	99
61	4255	0.61	22	0.003	1	12	55	5	1	119	25	3	1	25	47
62	6058	0.87	18	0.003	1	10	46	5	1	25	25	17	1	25	72
63	5738	0.82	35	0.005	1	15	25	5	1	91	25	3	1	25	71
64	4959	0.71	11	0.002	1	12	25	5	1	25	25	3	1	25	72
65	11168	1.60	29	0.004	1	17	68	5	1	57	25	14	1	55	60
66	6599	0.94	11	0.002	1	13	50	5	1	25	25	25	1	76	60
67	6455	0.92	19	0.003	1	1	107	5	1	110	25	13	1	25	61
68	5091	0.73	27	0.004	1	1	107	5	1	126	25	12	1	25	52
69	8221	1.18	31	0.005	1	10	73	5	1	166	25	24	1	70	142
70	10244	1.46	37	0.005	1	12	63	5	1	137	25	18	1	50	175
71	11155	1.59	32	0.005	1	9	91	5	1	165	25	20	1	86	171
72	8016	1.15	28	0.004	1	7	102	5	1	120	25	3	1	70	141
73	13205	1.89	60	0.009	1	13	102	5	1	128	25	27	1	71	133
74	5883	0.84	26	0.004	1	1	71	5	1	147	25	18	1	78	99
75	8888	1.27	27	0.004	1	8	102	5	1	130	25	17	1	82	102
76	7581	1.08	20	0.003	1	7	92	5	1	136	25	13	1	79	86
77	7789	1.11	29	0.004	1	1	119	27	1	172	83	18	1	79	90
78	12890	1.84	41	0.006	8	8	121	5	1	159	25	24	1	48	75
79	8529	1.22	24	0.004	1	7	92	28	1	109	97	3	1	70	85
80	9253	1.32	31	0.005	1	1	100	5	1	154	25	11	1	77	65
81	7588	1.08	29	0.004	1	7	130	5	1	188	25	13	1	73	85
82	10884	1.56	39	0.006	19	11	140	5	1	164	25	25	1	25	95
83	10484	1.50	31	0.005	1	10	113	5	1	164	25	20	1	74	104
84	19306	2.76	65	0.010	1	15	117	5	1	180	25	33	1	25	87
85	19765	2.83	76	0.011	1	10	145	5	1	151	25	37	1	100	84
86	10477	1.50	34	0.005	1	8	141	5	1	130	25	18	1	86	83
87	12073	1.73	38	0.006	1	11	147	5	1	200	25	23	1	63	87
88	11802	1.69	44	0.006	1	8	141	13	1	158	48	24	1	79	69

Table A2.1 Continued

Depth	Fe	Fe2O3T	Cr	Cr2O3	Ag	As	Ba	Bi	Cd	Ce	Co	Cu	Hg	La	Mo
cm	Ppm	Wt%	Ppm	Wt%	Ppm	Ppm	Ppm	Ppm	Ppm	Ppm	Ppm	Ppm	Ppm	Ppm	Ppm
89	10618	1.52	29	0.004	1	7	173	5	1	180	25	24	1	59	77
90	10508	1.50	27	0.004	13	9	163	5	1	146	120	22	1	86	65
91	12089	1.73	38	0.006	1	12	155	5	1	113	25	25	1	77	75
92	19027	2.72	67	0.010	1	12	173	5	1	100	25	32	1	72	77
93	9099	1.30	22	0.003	1	9	166	5	8	197	94	12	1	95	62
94	11242	1.61	32	0.005	13	8	134	5	1	118	25	26	1	97	64
95	21923	3.13	70	0.010	1	16	168	5	1	192	25	36	1	25	80
96	16916	2.42	49	0.007	15	19	188	5	1	146	25	27	1	68	90
97	9423	1.35	31	0.005	1	10	157	5	1	176	25	25	1	96	111
98	15383	2.20	51	0.007	1	16	136	5	1	168	25	36	1	72	114
99	11343	1.62	34	0.005	1	13	108	5	1	108	60	34	1	25	120

Table A2.3 X-ray fluorescence measurements in T01 0 – 1 m section.

Depth	Nb	Nd	Ni	Pb	Rb	Sb	Sn	Sr	Th	U	V	W	Y	Zn	Zr
Cm	Ppm	Ppm	Ppm	Ppm	Ppm	Ppm	Ppm	Ppm	Ppm	Ppm	Ppm	Ppm	Ppm	Ppm	ppm
1	18	2	24	27	301	46	1	310	1	37	30.7	2	2	94	13
2	14	2	2	17	298	41	1	286	1	45	12.2	2	2	71	1
3	18	2	19	30	350	27	1	318	1	97	27.6	2	2	85	8
4	19	2	17	35	367	26	1	313	1	80	29.0	2	2	58	9
5	16	2	2	38	330	44	1	304	1	43	18.7	2	2	43	8
6	16	2	23	47	361	42	1	335	1	64	17.8	2	2	39	1
7	18	2	12	57	382	41	1	341	1	69	26.2	2	2	40	5
8	17	2	29	59	386	43	1	347	1	94	21.3	2	2	38	6
9	14	2	37	97	333	37	1	305	1	101	34.7	2	2	56	9
10	17	2	39	112	353	44	1	344	1	91	30.3	2	2	69	21
11	14	2	29	126	318	41	13	311	1	83	26.2	2	2	56	21
12	17	2	36	107	338	62	1	334	1	81	27.9	2	2	60	23
13	21	2	48	88	352	44	1	303	1	124	34.1	2	2	52	28
14	17	2	40	101	342	37	14	295	1	77	35.0	2	2	43	38
15	17	2	42	91	274	45	1	305	1	55	31.4	2	2	47	63
16	17	2	20	75	320	33	1	307	1	36	19.5	2	2	37	26
17	22	2	21	105	338	32	1	317	1	35	21.3	2	2	41	31
18	20	2	2	75	326	33	1	305	1	37	23.0	2	2	22	40
19	14	2	29	104	309	29	1	318	1	55	22.9	2	2	38	38
20	17	2	36	94	304	49	1	322	1	47	26.9	2	2	20	40
21	15	2	12	59	289	30	1	282	1	41	9.5	2	2	23	31
22	20	2	26	79	309	28	1	322	1	44	17.1	2	2	35	34
23	15	2	2	52	257	19	1	282	1	27	9.5	2	2	21	29
24	13	2	18	68	255	27	1	310	1	60	14.4	2	2	23	33
25	12	2	2	57	231	16	1	278	1	46	8.3	2	11	14	40
26	11	2	27	87	215	1	1	340	16	90	49.3	2	115	38	64
27	10	2	48	101	189	18	1	377	1	133	55.7	2	149	46	68
28	12	2	23	79	191	15	1	319	1	103	38.6	2	90	36	59
29	12	2	30	77	200	37	1	264	1	58	38.6	2	36	46	57
30	20	2	18	83	174	28	1	309	1	49	18.9	2	36	33	172
31	19	2	2	148	157	18	1	324	21	40	24.8	2	57	32	270
32	14	2	2	161	120	22	18	381	1	24	28.6	2	46	20	271
33	15	2	2	160	105	21	1	382	8	1	40.7	2	64	40	229
34	9	2	2	165	141	19	1	332	1	102	18.3	2	49	28	74
35	6	2	14	69	145	24	1	280	1	92	34.9	2	79	42	65
36	4	2	24	132	140	12	1	307	1	135	34.7	2	104	45	70
37	7	2	2	31	129	20	1	307	1	127	30.5	2	101	30	71
38	1	2	35	40	145	36	1	316	1	130	66.0	2	123	57	104
39	9	2	2	1	122	17	1	279	1	86	18.3	2	85	24	59
40	4	2	19	7	136	19	1	280	16	121	30.7	2	110	40	93
41	3	2	14	1	130	15	1	277	1	123	39.4	2	96	44	65
42	9	2	20	1	134	17	1	315	26	86	25.8	2	111	37	62
43	6	2	45	20	117	20	1	228	1	88	22.5	2	86	42	38

Table A2.3 continued

Depth Cm	Nb Ppm	Nd Ppm	Ni Ppm	Pb Ppm	Rb Ppm	Sb Ppm	Sn Ppm	Sr Ppm	Th Ppm	U Ppm	V Ppm	W Ppm	Y Ppm	Zn Ppm	Zr ppm
44	4	2	34	1	126	12	1	236	1	104	34.4	2	111	54	63
45	1	2	21	9	129	1	1	260	13	121	29.1	2	100	41	85
46	10	2	29	9	129	22	1	245	1	59	25.1	2	97	62	58
47	1	2	31	10	139	23	1	262	1	102	33.8	2	124	56	47
48	5	2	19	1	123	17	1	272	1	112	19.5	2	60	100	7
49	4	2	28	10	137	13	1	272	5	99	31.9	2	103	92	67
50	5	2	21	10	125	1	1	257	17	86	18.1	2	84	69	58
51	7	2	25	9	119	9	1	255	7	93	31.7	2	101	92	61
52	9	2	2	8	118	1	1	231	15	78	14.5	2	74	51	41
53	5	2	13	11	118	14	1	258	1	87	18.5	2	81	122	37
54	6	2	2	14	117	14	1	237	1	88	22.5	2	98	39	75
55	7	2	19	14	111	13	1	238	1	70	22.5	2	95	67	55
56	7	2	22	14	133	18	1	263	1	93	22.9	2	88	43	75
57	6	2	31	15	125	1	1	287	1	104	44.0	2	113	118	44
58	6	2	28	11	116	18	1	256	18	80	42.2	2	109	105	82
59	8	2	14	15	118	7	1	251	5	69	29.6	2	93	38	50
60	7	2	14	14	118	15	1	275	14	59	20.2	2	82	47	41
61	11	2	18	1	176	23	1	337	1	83	21.2	2	49	57	48
62	8	2	18	14	152	1	1	312	1	78	18.5	2	49	38	77
63	5	2	18	13	142	14	1	291	1	112	39.8	2	79	76	48
64	9	2	2	1	164	1	1	305	15	78	16.8	2	25	42	30
65	10	2	18	9	165	23	1	260	7	61	34.2	2	38	49	48
66	10	2	2	10	149	1	1	279	1	51	15.5	2	27	47	76
67	10	2	2	19	125	18	1	274	15	40	25.4	2	72	45	84
68	11	2	15	23	129	1	1	272	22	35	25.0	2	79	48	76
69	9	2	16	20	114	18	1	265	16	40	29.1	2	101	65	63
70	8	2	19	29	116	13	1	248	13	49	41.6	2	106	104	53
71	9	2	26	24	121	22	1	269	27	31	29.9	2	112	94	59
72	7	2	19	17	106	13	1	251	17	31	27.0	2	96	50	67
73	10	2	24	18	117	16	1	253	17	37	57.0	2	109	126	62
74	7	2	2	16	109	1	1	237	22	22	22.2	2	80	42	51
75	8	2	18	15	107	1	1	251	20	23	29.9	2	93	103	78
76	11	2	16	10	105	17	1	230	21	20	26.1	2	93	42	75
77	10	2	17	16	100	14	1	239	11	20	25.0	2	90	87	111
78	10	2	9	18	108	9	1	228	16	20	36.0	2	92	83	89
79	10	2	17	13	98	1	1	238	19	15	29.7	2	88	81	68
80	11	2	2	12	99	16	1	232	20	21	28.1	2	88	39	77
81	10	2	27	18	107	12	1	247	19	33	28.3	2	87	88	74
82	13	2	15	16	114	19	1	280	18	15	34.0	2	101	58	77
83	10	2	25	16	109	14	1	291	13	29	28.8	2	98	137	118
84	13	2	25	18	113	1	1	218	22	25	66.0	2	104	83	146
85	12	2	30	17	106	1	1	214	21	29	75.0	2	111	114	140
86	11	2	21	15	103	1	1	228	17	25	34.0	2	93	72	121

Table A2.3 Continued

Depth	Nb	Nd	Ni	Pb	Rb	Sb	Sn	Sr	Th	U	V	W	Y	Zn	Zr
Cm	Ppm	Ppm	Ppm	Ppm	Ppm	Ppm	Ppm	Ppm	Ppm	Ppm	Ppm	Ppm	Ppm	Ppm	ppm
87	9	2	25	18	110	1	1	287	20	36	37.0	2	100	107	122
88	11	2	24	15	100	5	1	221	19	14	37.7	2	82	86	124
89	12	2	15	16	98	1	1	235	19	13	27.0	2	75	67	129
90	14	2	16	15	108	13	1	278	24	16	29.7	2	90	80	134
91	15	2	20	15	112	18	1	271	15	24	34.0	2	96	73	191
92	14	2	33	13	106	1	1	199	17	25	60.0	2	94	96	147
93	14	2	22	16	103	12	1	261	19	1	23.0	2	75	96	126
94	13	2	20	20	109	1	1	263	21	17	30.0	2	89	86	180
95	15	2	28	15	123	16	1	239	26	21	73.0	2	99	81	207
96	17	2	22	14	133	15	1	334	18	28	53.0	2	94	97	172
97	14	2	33	1	129	18	1	275	16	32	32.3	2	67	115	110
98	11	2	44	1	138	25	1	231	20	34	59.0	2	63	107	74
99	12	2	35	1	131	6	1	291	19	29	37.1	2	65	93	73

X-ray fluorescence measurements of T04

Table A2.4 X-ray fluorescence measurements in T04 0 – 1 m section.

Depth	Si	SiO2	P	P2O5	S	S	Cl	K	K2O	Ca	CaO	Ti	TiO2	Mn	MnO
Cm	Ppm	Wt%	Ppm	Wt%	Ppm	Wt%	Ppm	Ppm	Wt%	Ppm	Wt%	Ppm	Wt%	Ppm	Wt%
1	84464.8	18.1	300	0.07	9845	0.98	3767	3433	0.41	7029	0.98	996	0.166	415	0.054
2	69070.9	14.8	300	0.07	11112	1.11	4548	2989	0.36	6739	0.94	952	0.159	212	0.027
3	78388.6	16.8	300	0.07	14254	1.43	6689	3406	0.41	10243	1.43	865	0.144	173	0.022
4	85191.9	18.2	300	0.07	13133	1.31	14558	4613	0.56	7000	0.98	687	0.115	151	0.019
5	95743.7	20.5	300	0.07	15993	1.60	14117	4425	0.53	8254	1.15	892	0.149	150	0.019
6	61488	13.2	300	0.07	12397	1.24	13466	4710	0.57	7768	1.09	789	0.132	190	0.025
7	59467	12.7	300	0.07	14243	1.42	14514	6955	0.84	8939	1.25	670	0.112	156	0.020
8	48788	10.4	300	0.07	11470	1.15	14359	3344	0.40	6059	0.85	679	0.113	123	0.016
9	95359.2	20.4	300	0.07	12768	1.28	10944	5182	0.62	6623	0.93	1928	0.322	121	0.016
10	86966.2	18.6	300	0.07	12533	1.25	14085	3765	0.45	6178	0.86	1172	0.195	99	0.013
11	108790.8	23.3	300	0.07	12349	1.23	9827	5495	0.66	7067	0.99	2054	0.343	126	0.016
12	112051.2	24.0	300	0.07	11275	1.13	9324	5050	0.61	6105	0.85	1837	0.306	113	0.015
13	92117.1	19.7	300	0.07	10444	1.04	3780	4100	0.49	5282	0.74	1692	0.282	95	0.012
14	98016.6	21.0	300	0.07	9962	1.00	2782	3544	0.43	8227	1.15	1533	0.256	112	0.014
15	83796.1	17.9	300	0.07	11148	1.11	7649	3881	0.47	5844	0.82	1392	0.232	100	0.013
16	97657.9	20.9	300	0.07	8966	0.90	2385	4277	0.52	4397	0.62	1394	0.233	97	0.013
17	108188.2	23.1	300	0.07	10042	1.00	1981	4479	0.54	4908	0.69	1530	0.255	105	0.014
18	103531.8	22.1	300	0.07	11550	1.16	2337	4829	0.58	6281	0.88	1544	0.258	120	0.015
19	86424	18.5	300	0.07	11743	1.17	2212	3041	0.37	4395	0.61	1128	0.188	93	0.012
20	86263.9	18.5	300	0.07	15741	1.57	6134	3228	0.39	4692	0.66	825	0.138	74	0.010
21	41775.8	8.9	300	0.07	16968.5	1.70	4684.5	772.5	0.09	5287	0.74	387.5	0.065	50.6	0.007
22	42135.2	9.0	300	0.07	21238	2.12	7636	1230	0.15	4756	0.67	417	0.070	33.5	0.004
23	57636.5	12.3	300	0.07	21506	2.15	6782	2313	0.28	5272	0.74	685	0.114	49.1	0.006
24	38901.1	8.3	300	0.07	24613	2.46	6144	1160	0.14	5350	0.75	378	0.063	26.5	0.003
25	34909.4	7.5	300	0.07	24440	2.44	5827	1160	0.14	4683	0.66	409	0.068	35.1	0.005
26	16523	3.5	300	0.07	27854	2.79	5397	671	0.08	5008	0.70	237	0.040	28.9	0.004
27	30215	6.5	300	0.07	27108.5	2.71	6080.5	1090.5	0.13	5488	0.77	354	0.059	46.45	0.006
28	15088.7	3.2	300	0.07	34627	3.46	5643	652	0.08	6085	0.85	246	0.041	38	0.005
29	36487.1	7.8	300	0.07	29273	2.93	7043	1444	0.17	6493	0.91	529	0.088	59	0.008
30	41737.2	8.9	300	0.07	24177	2.42	7833	1745	0.21	6168	0.86	533	0.089	128	0.017
31	48931.4	10.5	300	0.07	25238	2.52	1738	2094	0.25	5477	0.77	618	0.103	89	0.011
32	37356.1	8.0	300	0.07	32581	3.26	5727	1868	0.23	6169	0.86	487	0.081	54.2	0.007
33	91367.4	19.5	300	0.07	27410	2.74	2343	4470	0.54	6164	0.86	1198	0.200	117	0.015
34	109547	23.4	300	0.07	42670	4.27	6737	5898	0.71	8989	1.26	1576	0.263	153	0.020
35	76652.5	16.4	300	0.07	33887	3.39	1685	3047	0.37	6401	0.90	1004	0.167	99	0.013
36	131466.9	28.1	300	0.07	36133	3.61	6387	6121	0.74	8331	1.17	1729	0.288	156	0.020
37	133572.5	28.6	300	0.07	37215	3.72	5554	5550	0.67	8266	1.16	1398	0.233	144	0.019
38	136490.6	29.2	300	0.07	45481	4.55	5370	5872	0.71	10224	1.43	1394	0.233	147	0.019
39	134766	28.8	300	0.07	42693	4.27	4862	5961	0.72	9048	1.27	1512	0.252	154	0.020

40	106418	22.8	300	0.07	50256	5.03	5476	3298	0.40	10644	1.49	845	0.141	86	0.011

Table A2.4 Continued

Depth	Si	SiO2	P	P2O5	S	S	Cl	K	K2O	Ca	CaO	Ti	TiO2	Mn	MnO
Cm	Ppm	Wt%	Ppm	Wt%	Ppm	Wt%	Ppm	Ppm	Wt%	Ppm	Wt%	Ppm	Wt%	Ppm	Wt%
41	131595.1	28.2	300	0.07	36407	3.64	3765	5157	0.62	7349	1.03	1489	0.248	139	0.018
42	123200.4	26.4	300	0.07	76623	7.66	3764	5961	0.72	4031	0.56	1701	0.284	197	0.025
43	122869	26.3	300	0.07	61212	6.12	3282	6520	0.79	4583	0.64	1693	0.282	190	0.025
44	105867.2	22.6	300	0.07	97231	9.72	5479	2973	0.36	9637	1.35	820	0.137	131	0.017
45	93631.6	20.0	300	0.07	71518	7.15	5440	4258	0.51	13536	1.89	1088	0.181	133	0.017
46	108982	23.3	300	0.07	78569	7.86	6127	4566	0.55	13802	1.93	1321	0.220	171	0.022
47	137873	29.5	300	0.07	54020	5.40	5152	5325	0.64	11887	1.66	1208	0.201	163	0.021
48	82436.5	17.6	300	0.07	177251	17.73	6122	3221	0.39	11925	1.67	968	0.161	171	0.022
49	95498.1	20.4	300	0.07	113636	11.36	4626	4756	0.57	14840	2.08	1271	0.212	225	0.029
50	78710	16.8	300	0.07	82325	8.23	3967	2816	0.34	15566	2.18	637	0.106	154	0.020
51	156271	33.4	300	0.07	49482	4.95	1591	6740	0.81	6047	0.85	1517	0.253	223	0.029
52	153155.8	32.8	300	0.07	46733	4.67	2570	7688	0.93	8004	1.12	1908	0.318	232	0.030
53	131582.4	28.1	300	0.07	64417	6.44	3345	8529	1.03	15208	2.13	2041	0.340	275	0.036
54	116461.7	24.9	300	0.07	71087	7.11	4149	6340	0.76	15005	2.10	1589	0.265	228	0.029
55	146587.4	31.4	300	0.07	71596	7.16	3895	6143	0.74	17573	2.46	1986	0.331	277	0.036
56	137235.8	29.4	300	0.07	84412	8.44	4912	7062	0.85	20337	2.85	1210	0.202	245	0.032
57	154152.3	33.0	300	0.07	42500	4.25	2634	6575	0.79	6863	0.96	1900	0.317	184	0.024
58	158817.1	34.0	300	0.07	32867	3.29	2631	6651	0.80	6156	0.86	1702	0.284	195	0.025
59	158960.4	34.0	300	0.07	31970	3.20	3123	4639	0.56	5657	0.79	1054	0.176	135	0.017
60	156155.9	33.4	300	0.07	39249	3.92	3459	4176	0.50	7267	1.02	1010	0.168	125	0.016
61	169729.9	36.3	300	0.07	35081	3.51	3205	5614	0.68	7463	1.04	1291	0.215	167	0.022
62	124336.6	26.6	300	0.07	67301	6.73	6808	4838	0.58	16285	2.28	1151	0.192	163	0.021
63	149940.8	32.1	300	0.07	33246	3.32	3892	5490	0.66	7210	1.01	1357	0.226	158	0.020
64	121008.5	25.9	300	0.07	64887	6.49	5970	4161	0.50	16893	2.36	939	0.157	146	0.019
65	142597.6	30.5	300	0.07	32130	3.21	3715	4634	0.56	7911	1.11	1196	0.199	181	0.023
66	149320.5	31.9	300	0.07	50216	5.02	6319	3838	0.46	12631	1.77	852	0.142	118	0.015
67	173951.2	37.2	300	0.07	29696	2.97	3578	4866	0.59	8048	1.13	1027	0.171	138	0.018
68	158936.1	34.0	300	0.07	56753	5.68	7199	4860	0.59	14848	2.08	995	0.166	146	0.019
69	167162.1	35.8	300	0.07	36870	3.69	4480	7778	0.94	7522	1.05	1110	0.185	135	0.017
70	171191.2	36.6	300	0.07	32483	3.25	3668	5174	0.62	7846	1.10	1037	0.173	122	0.016
71	193228.7	41.3	300	0.07	33902	3.39	3713	5364	0.65	8406	1.18	1071	0.179	127	0.016
72	171512.9	36.7	300	0.07	36826	3.68	6867	3916	0.47	9683	1.35	801	0.134	95	0.012
73	187030.9	40.0	300	0.07	27018	2.70	2897	4738	0.57	7608	1.06	922	0.154	109	0.014
74	205666.1	44.0	300	0.07	21687	2.17	2085	3808	0.46	6323	0.88	650	0.108	86	0.011
75	211312.9	45.2	300	0.07	25513	2.55	3203	4311	0.52	7013	0.98	758	0.126	89	0.011
76	167780.6	35.9	300	0.07	40287	4.03	10813	4018	0.48	10480	1.47	699	0.117	83	0.011
77	172122.4	36.8	300	0.07	37722	3.77	9645	4887	0.59	10277	1.44	783	0.131	101	0.013
78	198827.2	42.5	300	0.07	27848.5	2.78	3446	5282	0.64	8143.5	1.14	983	0.164	107.5	0.014
79	203239.8	43.5	300	0.07	28852	2.89	3903	5722	0.69	8848	1.24	1021	0.170	123	0.016
80	191254.8	40.9	300	0.07	30087	3.01	3741	5369	0.65	10344	1.45	1034	0.172	124	0.016
81	189639.5	40.6	300	0.07	27464	2.75	4279	5416	0.65	9470	1.33	1054	0.176	114	0.015
82	173937.3	37.2	300	0.07	35358	3.54	9390	5024	0.61	11356	1.59	931	0.155	100	0.013

83	195090.7	41.7	300	0.07	26248	2.62	3718	5633	0.68	11100	1.55	1013	0.169	117	0.015

Table A2.4 Continued

Depth	Si	SiO2	P	P2O5	S	S	Cl	K	K2O	Ca	CaO	Ti	TiO2	Mn	MnO
Cm	Ppm	Wt%	Ppm	Wt%	Ppm	Wt%	Ppm	Ppm	Wt%	Ppm	Wt%	Ppm	Wt%	Ppm	Wt%
84	190759.1	40.8	300	0.07	25052	2.51	4114	5352	0.64	8548	1.20	978	0.163	107	0.014
85	165644	35.4	300	0.07	31812	3.18	10115	4530	0.55	10046	1.41	824	0.137	98	0.013
86	191280.8	40.9	300	0.07	26245	2.62	5417	5216	0.63	9535	1.33	963	0.161	110	0.014
87	194475.7	41.6	300	0.07	28515	2.85	4279	5549	0.67	9328	1.31	1056	0.176	119	0.015
88	168879.8	36.1	300	0.07	35623	3.56	10264	4608	0.56	11118	1.56	800	0.133	99	0.013
89	205902.2	44.0	300	0.07	27245	2.72	5805	5582	0.67	9871	1.38	1004	0.167	112	0.014
90	167720.5	35.9	300	0.07	41323	4.13	12526	4774	0.58	12361	1.73	844	0.141	113	0.015
91	169323	36.2	300	0.07	42789	4.28	12452	4854	0.58	11876	1.66	899	0.150	115	0.015
92	189192.1	40.5	300	0.07	26666	2.67	4285	4979	0.60	8540	1.19	948	0.158	111	0.014
93	196977	42.1	300	0.07	26802	2.68	5526	5205	0.63	9768	1.37	941	0.157	113	0.015
94	200320.4	42.9	300	0.07	28180	2.82	4580	4720	0.57	8013	1.12	850	0.142	101	0.013
95	170761.1	36.5	300	0.07	35350	3.54	10578	4275	0.51	10551	1.48	800	0.133	91	0.012
96	189647.5	40.6	300	0.07	25464	2.55	5579	4612	0.56	8324	1.16	849	0.142	117	0.015
97	193802.2	41.5	300	0.07	25971	2.60	5541	4852	0.58	8317	1.16	944	0.157	104	0.013
98	199296.9	42.6	300	0.07	27421	2.74	5530	4667	0.56	8683	1.21	855	0.143	95	0.012
99	207967.5	44.5	300	0.07	25909	2.59	4381	4884	0.59	7772	1.09	856	0.143	92	0.012
100	216113.9	46.2	300	0.07	25433	2.54	4472	5098	0.61	8328	1.17	894	0.149	98	0.013

Table A2.5 X-ray fluorescence measurements in T04 0 – 1 m section.

Depth	Fe	Fe2O3T	Cr	Cr2O3	Ag	As	Ba	Bi	Cd	Ce	Co	Cu	Hg	La	Mo
Cm	Ppm	Wt%	Ppm	Wt%	Ppm	Ppm	Ppm	Ppm	Ppm	Ppm	Ppm	Ppm	Ppm	Ppm	ppm
1	21395	3.06	53	0.008	1	54	86	5	1	149	25	46	1	25	29
2	18550	2.65	45	0.007	1	53	74	5	1	25	25	50	1	25	17
3	21445	3.07	52	0.008	1	65	25	5	1	25	25	58	15	25	12
4	15464	2.21	33	0.005	1	42	142	5	1	25	25	44	1	25	15
5	15017	2.15	41	0.006	1	53	25	5	1	25	25	62	1	25	14
6	17476	2.50	40	0.006	1	45	120	5	1	25	25	32	1	25	16
7	20960	3.00	41	0.006	1	44	80	5	1	25	25	58	1	25	16
8	11877	1.70	31	0.005	1	40	141	5	1	25	25	46	1	25	21
9	4996	0.71	36	0.005	1	31	332	5	1	115	25	19	1	25	24
10	7541	1.08	38	0.006	1	48	196	5	1	120	25	38	1	25	30
11	6367	0.91	51	0.007	1	51	325	5	1	25	25	36	1	71	29
12	5404	0.77	53	0.008	1	44	206	5	1	148	25	27	1	89	23
13	6255	0.89	65	0.010	1	69	264	5	1	140	25	40	1	25	27
14	5595	0.80	124	0.018	1	85	156	5	1	155	25	33	1	25	25
15	5760	0.82	78	0.011	1	56	140	5	1	181	25	22	1	150	16
16	5908	0.84	65	0.010	1	40	147	5	1	125	25	29	1	92	21
17	7348	1.05	68	0.010	1	35	193	5	1	121	25	21	10	25	19
18	5957	0.85	89	0.013	1	32	346	5	1	118	25	16	1	71	20
19	7097	1.01	67	0.010	1	45	143	5	1	195	25	60	1	126	50
20	5027	0.72	62	0.009	1	42	130	5	1	119	25	42	1	84	37
21	2372	0.34	82	0.012	1	34	25	5	1	202	25	34.5	1	98	38
22	2133	0.30	47.8	0.007	1	18	25	5	1	185	25	25	1	74	40
23	3463	0.50	40	0.006	1	22	121	5	1	90	25	26	1	79	38
24	1953	0.28	39	0.006	1	27	25	5	1	25	25	12	1	81	59
25	2271	0.32	40.3	0.006	1	21	43	5	1	126	25	3	1	25	47
26	1747	0.25	34.9	0.005	1	33	25	5	1	103	25	3	1	25	75
27	2897	0.41	54	0.008	1	23	25	5	1	142.5	25	28	1	102	37
28	2378	0.34	50	0.007	1	35	25	5	1	25	25	14	1	25	96
29	5031	0.72	71	0.010	1	22	25	5	1	196	25	32	1	89	38
30	5335	0.76	43	0.006	1	26	25	5	1	116	25	22	1	25	42
31	5070	0.72	83	0.012	1	25	90	5	1	161	25	30	1	87	45
32	2278	0.33	70	0.010	1	15.8	54	5	1	153	25	18	1	86	46
33	6201	0.89	93	0.014	1	28	135	5	1	218	25	59	1	111	98
34	8113	1.16	105	0.015	1	14	249	5	1	296	25	70	1	116	123
35	4696	0.67	118	0.017	1	28	156	5	1	217	25	53	1	98	95
36	8422	1.20	95	0.014	1	18	237	5	1	230	25	62	1	127	118
37	8348	1.19	92	0.013	1	21	208	5	1	255	25	36	1	111	104
38	8018	1.15	91	0.013	1	16	193	5	1	220	25	69	1	81	145
39	9220	1.32	97	0.014	1	28	243	5	27	255	25	72	1	109	149
40	5705	0.82	79	0.012	15	27	202	5	1	178	25	78	1	128	193
41	7964	1.14	122	0.018	1	28	201	5	1	225	25	65	1	114	146
42	59641	8.53	130	0.019	1	110	187	5	48	244	25	51	1	88	277
43	42324	6.05	111	0.016	1	60	211	5	23	208	25	54	1	92	212

Table A2.5 Continued

Depth	Fe	Fe2O3T	Cr	Cr2O3	Ag	As	Ba	Bi	Cd	Ce	Co	Cu	Hg	La	Mo
Cm	Ppm	Wt%	Ppm	Wt%	Ppm	Ppm	Ppm	Ppm	Ppm	Ppm	Ppm	Ppm	Ppm	Ppm	ppm
44	43477	6.22	99	0.014	1	54	168	5	11	230	25	56	1	130	210
45	17021	2.43	70	0.010	1	27	198	5	17	220	25	30	1	115	108
46	21489	3.07	105	0.015	1	28	195	5	1	201	25	22	1	114	64
47	12418	1.78	102	0.015	1	28	344	5	9	197	25	39	1	130	75
48	96142	13.75	117	0.017	21	29	232	5	1	209	25	30	1	25	122
49	43023	6.15	100	0.015	21	18	281	5	1	283	25	19	1	153	96
50	22364	3.20	84	0.012	1	16	119	5	1	264	25	32	1	95	97
51	29215	4.18	117	0.017	1	14	222	5	1	259	25	44	1	116	86
52	26337	3.77	117	0.017	1	14	243	5	1	289	25	40	1	116	91
53	28656	4.10	98	0.014	1	18	353	5	1	218	25	39	1	82	81
54	24931	3.56	93	0.014	1	22	326	5	1	248	25	35	1	115	86
55	20537	2.94	101	0.015	1	12.1	346	5	1	261	25	40	1	140	78
56	23460	3.35	97	0.014	1	14	331	5	1	253	25	33	1	123	68
57	29084	4.16	109	0.016	1	18	337	5	1	186	25	39	1	25	79
58	20865	2.98	107	0.016	1	17	242	5	1	181	25	44	1	85	108
59	16699	2.39	93	0.014	1	15.7	212	5	1	177	25	43	1	95	132
60	16127	2.31	79	0.012	1	22	151	5	9	166	25	52	1	99	121
61	16624	2.38	84	0.012	1	12.6	220	5	1	187	25	39	1	76	96
62	15858	2.27	70	0.010	1	15.2	380	5	7	198	25	43	1	116	98
63	20366	2.91	88	0.013	1	17	276	5	1	186	25	43	1	104	103
64	15306	2.19	66	0.010	1	15.7	188	5	8	149	25	50	1	69	123
65	23524	3.36	83	0.012	1	23	181	5	1	132	25	50	1	90	124
66	12991	1.86	58	0.008	1	14.9	147	5	1	126	25	44	1	25	125
67	15472	2.21	67	0.010	1	16.2	198	5	1	212	25	46	1	79	112
68	13150	1.88	56	0.008	1	9.7	254	5	1	180	25	51	1	76	111
69	16266	2.33	65	0.010	1	19	171	5	1	174	25	36	1	86	128
70	12824	1.83	70	0.010	1	10.4	158	5	1	149	25	47	1	59	101
71	15883	2.27	72	0.011	1	16	146	5	1	153	25	63	1	76	121
72	12179	1.74	56	0.008	1	14.1	190	5	1	120	25	49	1	76	104
73	12287	1.76	69	0.010	1	10.3	127	5	1	106	25	44	1	25	106
74	10198	1.46	56	0.008	1	14.9	118	5	1	104	25	39	1	25	103
75	11696	1.67	57	0.008	1	15.8	139	5	1	111	25	46	1	65	132
76	11614	1.66	53	0.008	1	13.7	117	5	1	126	25	49	1	25	132
77	11667	1.67	49	0.007	1	13.7	147	5	1	128	25	43	1	77	106
78	13575	1.94	61	0.009	1	15.1	151	5	1	97	25	50	1	55.5	108
79	13608	1.95	60	0.009	1	15	174	5	1	119	25	50	1	85	103
80	13371	1.91	73	0.011	1	14.3	149	5	1	113	25	67	1	25	120
81	14056	2.01	59	0.009	1	15.1	124	5	1	148	25	62	1	25	99
82	11476	1.64	52	0.008	1	12.3	130	5	1	99	25	57	1	25	91
83	12961	1.85	73	0.011	1	12.2	175	5	1	99	25	54	1	94	85
84	12050	1.72	53	0.008	1	14.7	145	5	1	105	25	48	1	94	89
85	11489	1.64	46	0.007	1	12.1	159	5	1	121	25	41	1	25	83
86	12731	1.82	58	0.008	1	10.4	164	5	1	105	25	47	1	75	85

Table A2.5 Continued

Depth	Fe	Fe2O3T	Cr	Cr2O3	Ag	As	Ba	Bi	Cd	Ce	Co	Cu	Hg	La	Mo
Cm	Ppm	Wt%	Ppm	Wt%	Ppm	Ppm	Ppm	Ppm	Ppm	Ppm	Ppm	Ppm	Ppm	Ppm	ppm
87	13857	1.98	63	0.009	1	13.2	152	5	1	89	25	54	1	25	90
88	11347	1.62	49	0.007	1	11.8	141	5	1	134	25	53	1	25	86
89	15415	2.20	64	0.009	1	15	144	5	1	109	25	71	1	25	91
90	11762	1.68	50	0.007	1	17.5	120	5	1	114	25	47	1	25	84
91	11967	1.71	49	0.007	1	16.8	137	5	1	159	25	49	1	25	80
92	11103	1.59	61	0.009	1	11.6	101	5	1	25	25	39	1	73	81
93	12851	1.84	66	0.010	1	12.8	145	5	1	114	25	54	1	62	83
94	11573	1.65	48	0.007	1	11.6	145	5	1	25	25	53	1	25	89
95	10249	1.47	60	0.009	1	13.3	116	5	1	126	25	34	1	25	98
96	11021	1.58	52	0.008	1	9.9	120	5	1	25	25	42	1	25	98
97	11790	1.69	63	0.009	14	18.5	126	5	1	92	25	50	1	25	99
98	11594	1.66	55	0.008	1	12.5	107	5	1	122	25	56	1	68	94
99	11544	1.65	51	0.007	1	13.7	122	5	1	117	25	47	1	61	84
100	11719	1.68	50	0.007	1	13.3	120	5	1	25	25	55	1	25	84

Table A2.6 X-ray fluorescence measurements in T04 0 – 1 m section.

Depth	Nb	Nd	Ni	Pb	Rb	Sb	Se	Sn	Sr	Th	U	V	W	Y	Zn	Zr
Cm	Ppm	Ppm	Ppm	Ppm	Ppm	Ppm	Ppm	Ppm	Ppm	Ppm	Ppm	Ppm	Ppm	Ppm	Ppm	ppm
1	15.4	2	19	179	165	33	9.6	1	272	1	39	48	2	50	188	67
2	12	2	29	174	169	44	6.9	1	274	1	58	44	2	35	192	110
3	8	2	27	150	177	94	9.5	32	310	1	46	50	2	22	232	143
4	14.8	2	2	145	183	33	8.6	1	272	1	37	33.6	2	19	160	69
5	14	2	27	152	186	44	9	1	268	1	41	37	2	2	167	114
6	11.3	2	19	155	169	46	8.6	1	284	1	45	37	2	19	172	86
7	11	2	20	149	162	72	9.2	1	271	1	44	36	2	19	210	44
8	16.5	2	17	194	170	28	9.9	1	296	1	49	26.6	2	32	141	204
9	26.4	2	2	306	154	26	3.6	17	308	1	1	54	2	61	78	369
10	27.9	2	2	347	160	25	7.9	1	298	25	35	47.3	2	75	87	274
11	29	2	2	416	190	20	6.4	1	414	20	51	68	2	87	99	299
12	26	2	2	392	191	25	9.1	1	348	17	69	67	2	104	76	335
13	24.9	2	21	444	222	19	14.1	1	356	17	62	66	2	95	81	360
14	19.4	2	25	528	245	28	13.4	1	395	1	76	120	2	127	84	310
15	16.9	2	13	448	196	24	10.9	1	327	18	80	72	2	172	72	387
16	18.9	2	20	336	270	19	15	1	278	19	90	65	2	74	66	279
17	25	2	13	235	246	19	14	1	321	33	81	75	2	78	59	415
18	21.7	2	14	241	228	15	11.3	1	360	18	55	97	2	85	42	367
19	16.4	2	12	352	202	15	13.5	1	278	16	92	64.5	2	121	45	171
20	10	2	23	319	212	33	14.3	1	279	1	107	60.4	2	113	38	76
21	1	2	30	153.5	178.5	21.5	14.55	1	276	1	145	72.05	2	185	25.5	21.7
22	8.4	2	19	90	213	15	15.7	1	276	1	103	41.5	2	117	27	79
23	14.3	2	21	92	182	15	11.1	1	279	18	78	50.8	2	90	34	177
24	8.7	2	23	37	218	1	12.7	1	285	1	96	48.2	2	61	23	36.3
25	7.7	2	13	48	197	19	14.7	1	284	1	104	46.3	2	103	22	62.5
26	1	2	2	41	115	21	8.8	1	280	1	104	45.2	2	102	19	19.9
27	1	2	32	51.5	140	20	12.7	15	297	1	147	55.15	2	151	32	83
28	1	2	38	29	112	20	7.6	1	315	1	102	73.6	2	135	33	13
29	1	2	34	58	152	27	10	1	305	1	129	66.7	2	190	34	116
30	6.2	2	18	93	138	24	9.8	1	298	1	93	46.2	2	133	54	80
31	1	2	30	66	141	1	9.5	1	331	1	133	82.4	2	189	27	169
32	1	2	29	14	126	16	9.7	1	342	14	144	63.3	2	224	25	65.6
33	11.3	2	40	39	133	18	13	1	336	17	128	96	2	226	52	175
34	22.1	2	29	25	144	13	11.4	1	362	38	71	103	2	251	49	353
35	9.2	2	30	29	134	17	12.9	1	356	20	140	125	2	253	43	133
36	17	2	35	22	139	1	12	1	330	31	71	83	2	211	52	315
37	17	2	36	22	139	13	10.7	1	326	32	97	84	2	230	56	374
38	17.1	2	26	13	126	1	13.2	1	309	25	78	82	2	216	49	379
39	21	2	36	20	131	28	11.8	1	376	24	82	99	2	251	63	395
40	16	2	41	19	173	19	18.2	1	326	21	86	71.5	2	183	92	238
41	22	2	42	23	122	23	14.2	1	339	36	80	111	2	241	75	315
42	16.1	2	200	11	115	21	13.5	1	188	16	59	146	2	212	455	214
43	16.5	2	68	29	127	1	11.5	1	214	1	65	111	2	165	142	336

Table A2.6 Continued

Depth	Nb	Nd	Ni	Pb	Rb	Sb	Se	Sn	Sr	Th	U	V	W	Y	Zn	Zr
Cm	Ppm	Ppm	Ppm	Ppm	Ppm	Ppm	Ppm	Ppm	Ppm	Ppm	Ppm	Ppm	Ppm	Ppm	Ppm	ppm
44	8.5	2	113	16	133	21	14.3	1	213	17	70	89	2	204	294	192
45	13.4	2	52	15	112	17	7.7	1	254	19	58	69	2	169	159	251
46	10.8	2	61	12	110	17	6.3	1	301	19	50	96	2	216	207	463
47	18.7	2	60	22	119	15	6.6	1	350	29	45	88	2	220	177	317
48	11.9	2	73	1	76	17	8.9	1	207	15	28	106	2	163	158	227
49	17.2	2	40	1	108	18	5.2	1	299	20	30	104	2	170	134	265
50	11.7	2	32	1	103	17	6.7	1	287	15	31	72	2	176	145	128
51	12.6	2	31	9	114	18	4.9	1	298	18	34	109	2	220	124	271
52	17.1	2	43	10	119	15	5.2	1	316	25	28	111	2	225	138	400
53	24.8	2	30	8	121	1	5.3	1	403	23	1	97	2	195	125	363
54	15.4	2	36	1	100	1	6.4	1	411	22	25	97	2	187	135	398
55	16.2	2	36	8	101	1	5.7	1	348	26	1	105	2	207	160	326
56	17.6	2	34	8	107	14	6.3	1	353	31	25	95	2	192	203	394
57	18.1	2	25	8	103	24	9.5	1	284	20	16	109	2	153	104	368
58	19.6	2	45	12	126	16	9	1	280	22	36	99	2	172	89	237
59	12.8	2	42	12	124	1	8.4	1	255	24	41	86	2	163	92	197
60	14.5	2	43	10	108	19	11.5	1	333	22	62	87	2	137	169	201
61	14.4	2	52	7	108	1	10.2	1	276	21	46	84	2	125	151	271
62	21.8	2	43	10	123	20	10.3	1	374	18	39	70	2	130	115	352
63	15.6	2	44	16	128	16	8.9	1	320	26	49	79	2	143	82	357
64	19.1	2	58	1	117	1	14.8	1	323	22	46	64	2	107	184	194
65	15.6	2	35	8	121	1	11.1	1	324	21	53	87	2	133	101	224
66	15.6	2	56	1	121	14	11	1	310	18	58	58	2	108	101	160
67	15.1	2	55	1	120	12	11.8	1	308	26	64	74	2	108	123	161
68	15.5	2	45	1	113	21	10.9	1	348	23	55	66	2	117	123	258
69	19.3	2	49	1	128	1	12.9	1	336	32	42	76	2	109	102	211
70	13.4	2	53	1	111	1	10.8	1	291	22	58	61	2	92	122	119
71	14.6	2	59	1	129	16	13.4	1	361	22	58	69	2	99	136	139
72	13.2	2	46	1	126	19	12.4	1	350	16	61	52	2	91	98	166
73	12.6	2	56	1	110	1	10	1	320	20	58	61	2	96	106	134
74	10.3	2	52	1	105	26	11.6	1	328	21	50	45	2	83	99	127
75	7.5	2	54	1	120	17	11.8	1	347	17	61	52	2	74	98	99
76	12.3	2	61	1	127	13	13	1	368	15	54	51	2	80	108	111
77	10.2	2	49	1	115	1	10.3	1	372	26	65	50	2	83	108	116
78	12.65	2	60	1	120.5	8	11.4	1	374.5	24	43.5	64	2	99	111	137.5
79	15.7	2	48	1	123	14	11.7	1	376	20	47	60	2	102	120	136
80	12	2	53	1	116	16	11.8	1	431	20	78	69	2	111	112	159
81	12.6	2	62	1	117	1	11.9	1	417	20	71	58	2	106	139	134
82	14.5	2	50	1	108	15	9.2	1	399	27	51	48	2	106	107	117
83	10.5	2	51	1	112	18	12.8	1	417	30	75	59	2	106	110	127
84	12.3	2	51	1	109	13	9.5	1	331	26	38	50	2	72	108	109
85	13.1	2	51	1	112	15	9.8	1	385	21	40	40	2	84	106	137
86	8.9	2	44	1	112	14	9.2	1	426	24	64	55	2	119	114	135

Table A2.6 Continued

Depth	Nb	Nd	Ni	Pb	Rb	Sb	Se	Sn	Sr	Th	U	V	W	Y	Zn	Zr
Cm	Ppm	Ppm	Ppm	Ppm	Ppm	Ppm	Ppm	Ppm	Ppm	Ppm	Ppm	Ppm	Ppm	Ppm	Ppm	ppm
87	13.1	2	49	1	107	14	12	1	385	22	36	57	2	81	116	151
88	12.5	2	44	1	103	15	8.8	1	396	23	29	45	2	85	109	127
89	15.6	2	57	1	122	25	13.9	1	437	17	34	48	2	86	128	121
90	11.8	2	48	1	110	15	11.8	1	446	14	63	44	2	121	112	131
91	12.4	2	37	1	105	1	11.1	1	404	21	33	49	2	84	107	130
92	11.9	2	51	1	96	17	10.2	1	352	22	33	47	2	78	101	112
93	11.9	2	51	1	104	14	11	1	400	23	48	49	2	107	112	142
94	10	2	52	1	110	17	10.2	1	364	12	29	51	2	83	118	119
95	11.1	2	45	1	106	13	12.5	1	350	18	42	44	2	83	91	120
96	13.3	2	49	1	106	16	10.9	1	321	20	36	51	2	73	94	110
97	13.7	2	62	1	111	1	12.5	1	354	17	39	59	2	76	110	137
98	11.7	2	46	1	102	1	8.9	1	364	23	44	46	2	71	101	114
99	11.8	2	52	1	102	12	11.1	1	336	18	35	49	2	69	93	111
100	12.3	2	60	1	104	24	7.3	1	359	20	38	49	2	89	100	140

Appendix 3

High-Resolution RGP Photographs of T01

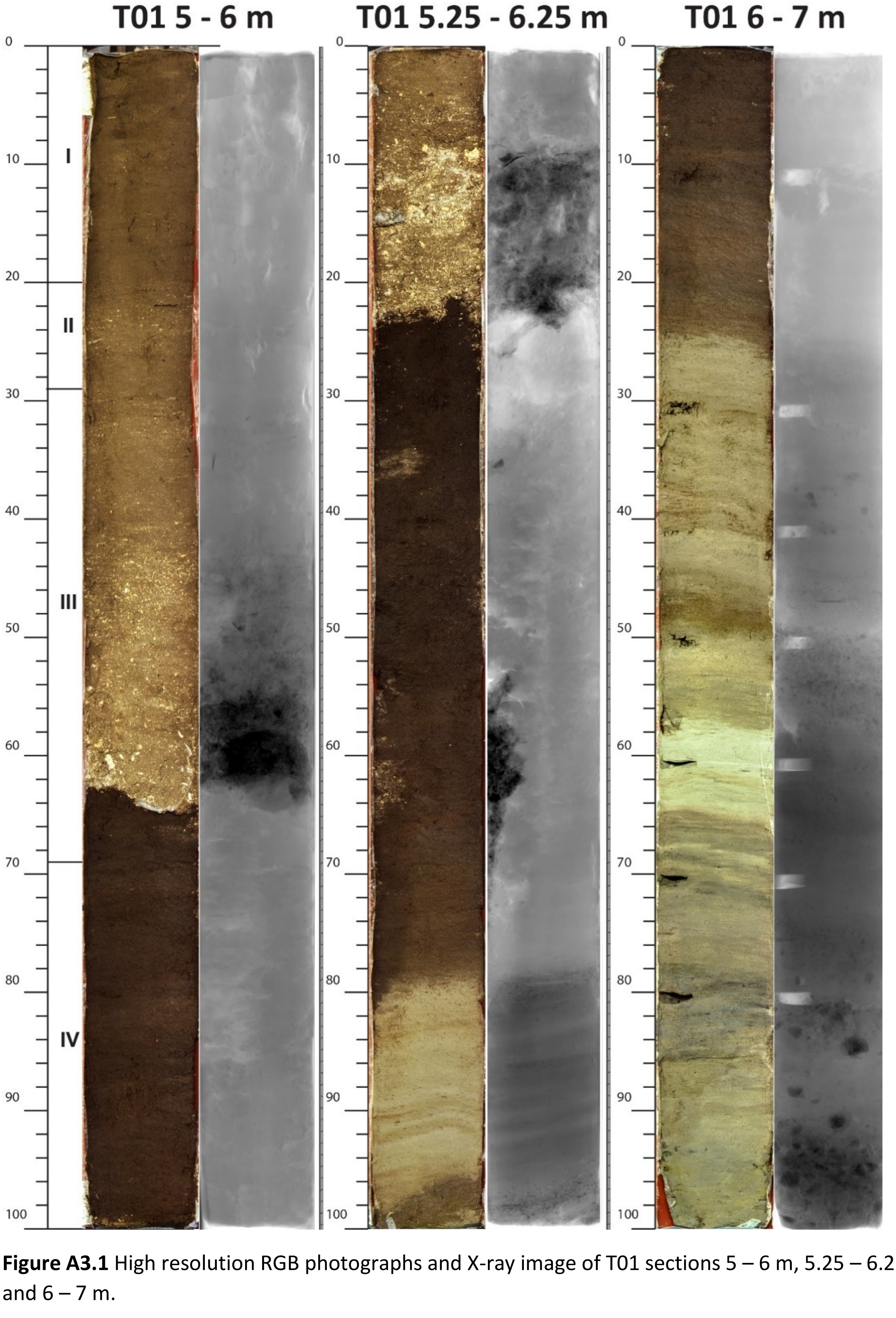

Figure A3.1 High resolution RGB photographs and X-ray image of T01 sections 5 – 6 m, 5.25 – 6.25 m and 6 – 7 m.

Magnetic susceptibility Measurements for T01

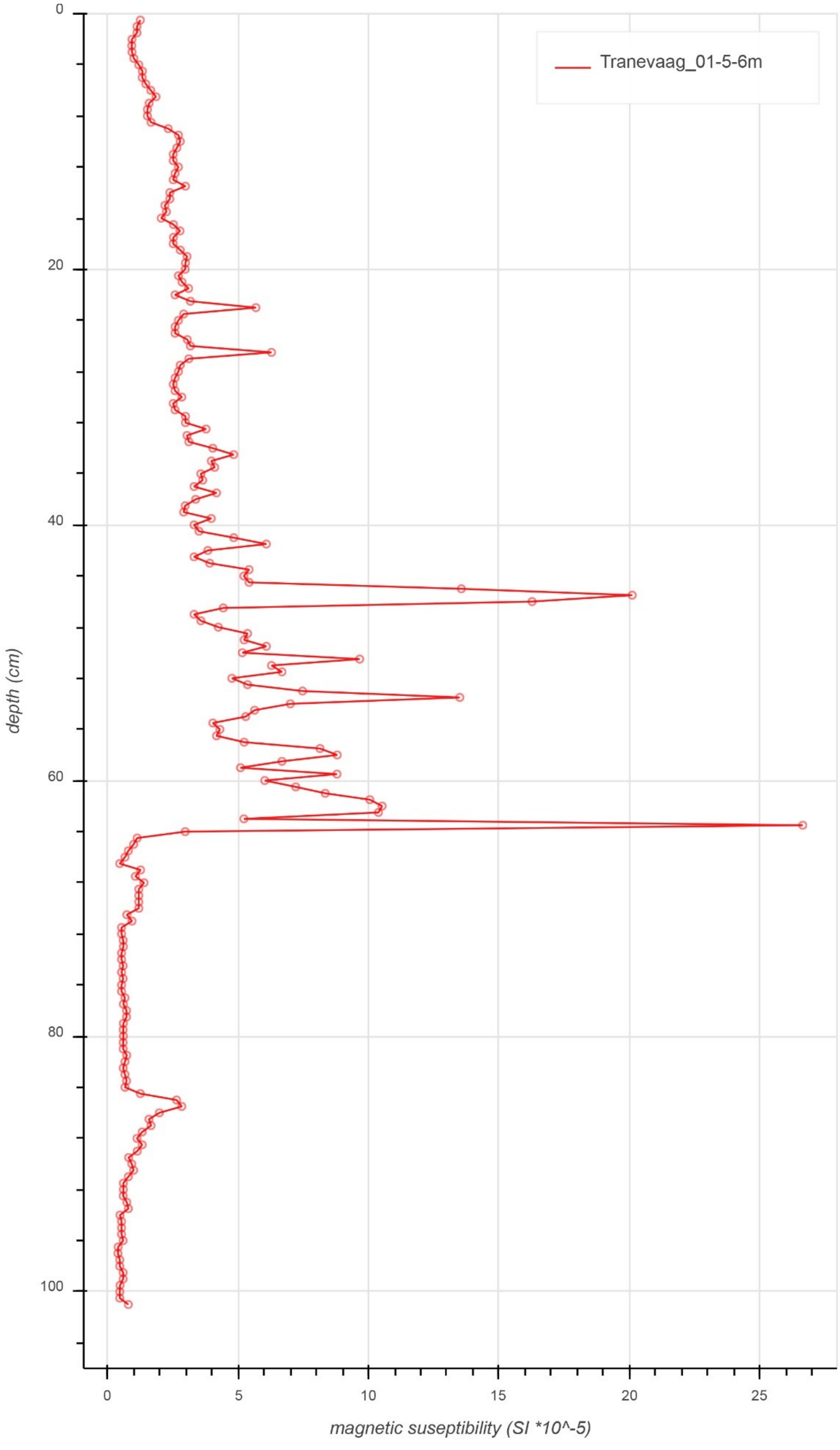

Figure A3.2 Magnetic susceptibility measurements for T01 5 – 6 m section

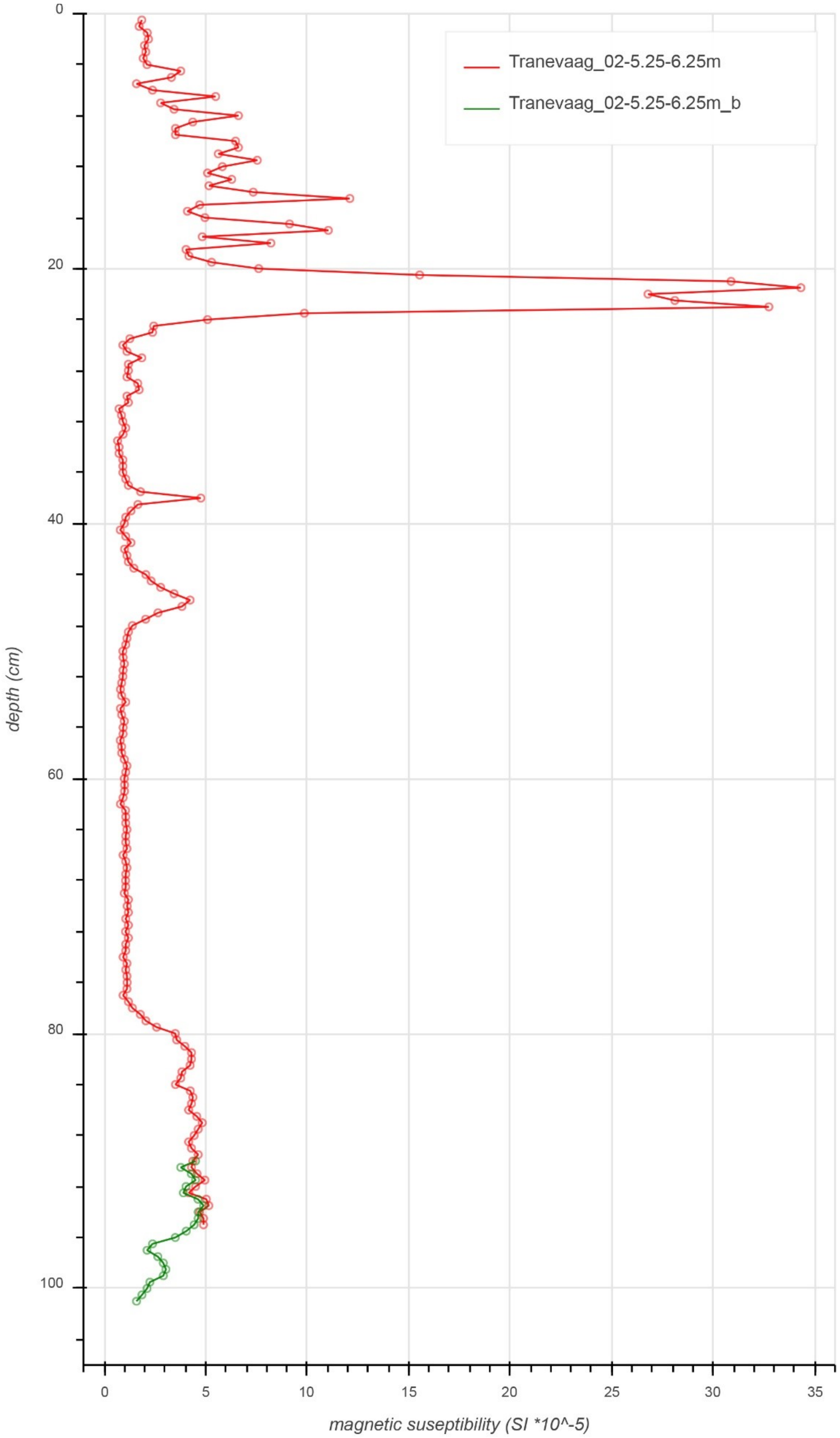

Figure A3.3 Magnetic susceptibility measurements of T01 5.25 – 6.25 m section

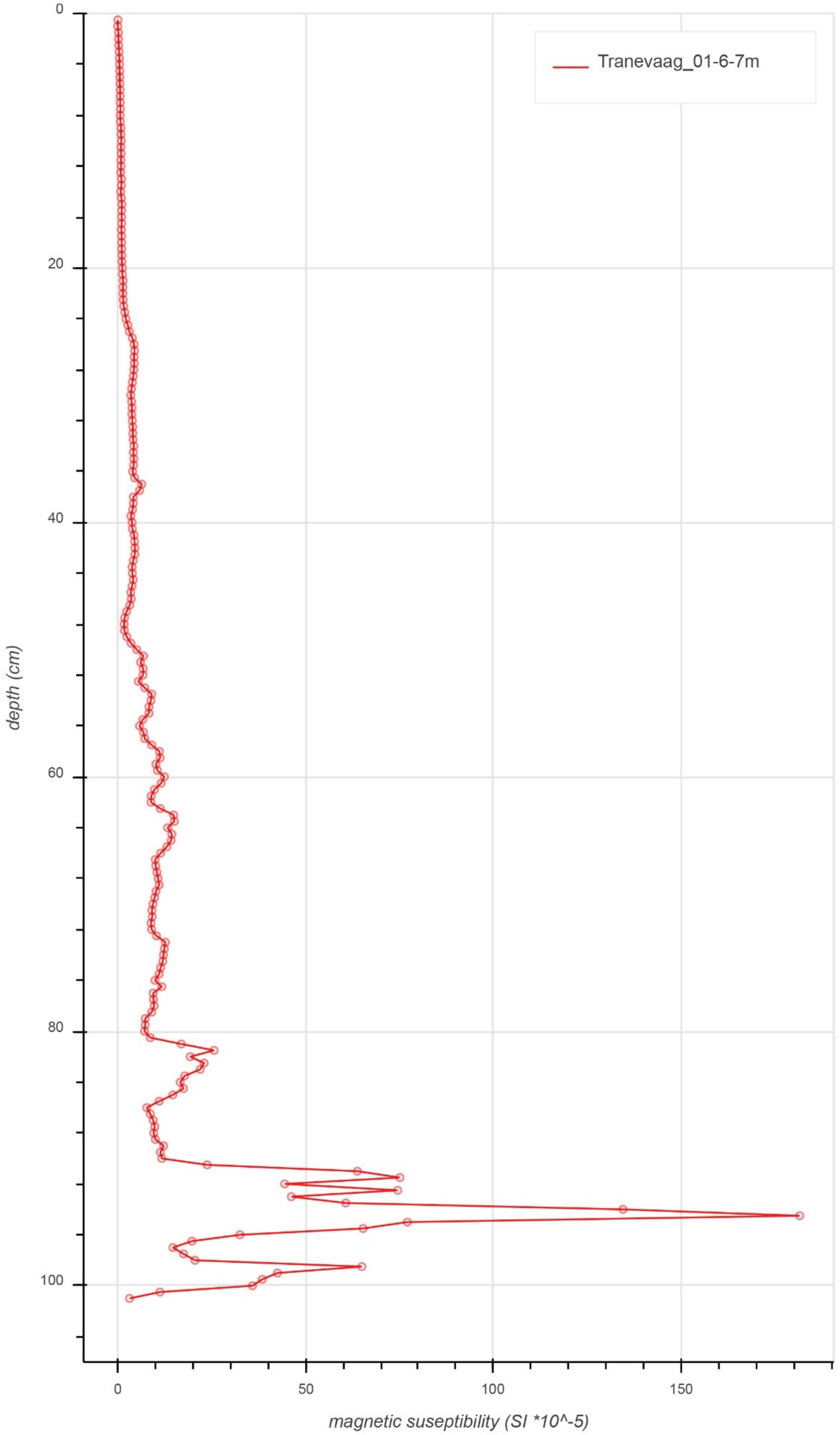

Figure A3.4 Magnetic susceptibility measurements of T01 6 – 7 m section

Oskar E. Lilienthal

The onset of relative sea-level rise in the late 19th century at Tranevåg salt marsh, southern Norway.

NTNU
Norwegian University of
Science and Technology